



**Experimental and numerical study of an easily
replaceable dissipative system for concrete-steel
composite structures when subjected to seismic
actions - DRBrC**

Nuno Manuel Marques Rosas

Thesis to obtain the Master of Science Degree in

Civil Engineering

Supervisors:

Prof. Dr. Luís Manuel Calado de Oliveira Martins

Prof. Dr. Jorge Miguel Silveira Filipe Mascarenhas Proença

Examination Committee

Chairperson: Prof. Dr. Orlando José Barreiros D'Almeida Pereira

Supervisor: Prof. Dr. Luís Manuel Calado de Oliveira Martins

Member of the Committee: Prof. Dr. Alper Kanyilmaz

November 2021

Statement

I state that the present document is an original work of my own authorship and that it fulfills all the requirements of the Code of Conduct and Good Practices of the University of Lisbon.

Declaração

Declaro que o presente documento é um trabalho original da minha autoria e que cumpre todos os requisitos do Código de Conduta e Boas Práticas da Universidade de Lisboa.

Agradecimentos

Primeiro de tudo quero dar um grande obrigado a três pessoas importantes na realização desta tese, são elas o Diogo Cabrita no qual sempre me apoiou e deu-me dicas até quando começou a trabalhar, o Professor Luís Calado pela sua disponibilidade e conselhos para realização da tal e por fim ao técnico Fernando Alves que com o seu bom humor tornou os ensaios de laboratório mais engraçados.

Também queria agradecer à minha família, especialmente aos meus pais pela oportunidade que me deram de estudar no IST, aos meus avós e tias por me acolherem tão bem nestes seis anos de curso.

Por fim um obrigado aos meus amigos tanto os de faculdade, sem eles estes últimos seis anos não seriam a mesma coisa, e aos meus velhos amigos da minha cidade natal, Aveiro, que também estiveram sempre ao dispor.

Acknowledgments

First, I want to give a big thank you to three important people in the realization of this thesis, they are Diogo Cabrita in which always supported me and gave me tips even when he started working, Professor Luís Calado for his availability and advice for the realization of this thesis and finally the technician Fernando Alves who with his good humour made the laboratory tests more fun.

I would also like to thank my family, especially my parents for the opportunity they gave me to study at IST, my grandparents and aunts for welcoming me so well during these six years of my course.

Finally, a thank you to my friends from college, without them these last six years wouldn't be the same, and to my old friends from my hometown, Aveiro, who were always there for me.

Abstract

Notwithstanding the design of more conventional structures, in accordance with EC8, devices capable of dissipating energy from earthquakes have also been developed and studied. Conventional energy dissipation systems rely on the inelastic deformation of major structural elements. This leads to a long interruption of the building's functionality, assuming that repair work is feasible and not too expensive. The DISSIPABLE project is currently developing an innovative, low-cost, easily replaceable dissipative device to absorb seismic energy while leaving the main structure intact. These devices are installed in braced steel frames.

This MSc Dissertation, developed within the framework of the DISSIPABLE research project, presents several results of force and cumulative dissipated energy, through cyclic testing, of several possible application configurations such as different types of steel in both the boxes (S355 and HSS) and pins (S235 and StS) and internal plate distances of the boxes (70mm and 90mm). A parametric analysis is performed trying to reach an optimal configuration. An analysis of the type of breakage of the pins was also performed, finding that some broke by bending and others by cutting which is a less desirable situation due to the greater difficulty in removing the pin.

A brief numerical analysis is also performed by modeling the devices and applying a "ductile damage" damage criterion, using the ABAQUS software.

Finally, and as mentioned before, being an easy device to replace (pin), 4 boxes were reused to study the behaviour in a second use and the results were different due to the ovalizations suffered in the 1st test.

Keywords: repairable dissipative devices; cyclic testing; hysteretic behaviour; ductile damage; braced frames; boxes reuse.

Resumo

Não obstante ao EC8, foram também desenvolvidos e estudados aparelhos capazes de dissipar energia proveniente dos terremotos. Os sistemas convencionais de dissipação de energia dependem da deformação inelástica dos principais elementos estruturais. Isto leva a uma longa interrupção da funcionalidade do edifício, assumindo que o trabalho de reparação é viável e não muito caro. O projecto DISSIPABLE está actualmente a desenvolver um dispositivo dissipativo inovador, de baixo custo e facilmente substituível, para absorver a energia sísmica, deixando a estrutura principal intacta. Estes aparelhos são instalados em pórticos contraventados.

Esta Dissertação de Mestrado é continuação do trabalho DISSIPABLE 2019. Apresenta vários resultados de força e energia acumulada dissipada, através de ensaios cíclicos, de várias configurações possíveis de aplicação como diferentes tipos de aço tanto nas caixas (S355 e HSS) como nos pinos (S235 e StS) e distanciamento de placas internas das caixas (70mm e 90mm). É realizada uma análise paramétrica tentando chegar a uma configuração ótima. Acrescenta-se também a análise do tipo de rotura dos pinos sendo que uns romperam por flexão e outros por corte que é uma situação menos desejada devido à dificuldade maior na remoção do pino.

Também é realizada uma breve análise numérica modelando os aparelhos e aplicando um critério de dano, Rotura Dúctil, usando o ABAQUS.

Por fim e como referido anteriormente, sendo um dispositivo fácil de substituir (pino), reutilizaram-se 4 caixas para estudar o comportamento numa segunda utilização e os resultados foram diferentes devido às ovalizações sofridas no 1º ensaio.

Palavras-chave: Dispositivos dissipativos reparáveis; ensaios cíclicos; comportamento histórico; rotura dúctil; pórticos contraventados; reutilização de caixas.

Contents

Agradecimientos	iii
Acknowledgments	iii
Abstract	v
Resumo	vi
1. Introduction	1
1.1 DISSIPABLE-DRBrC	2
1.2 Personal Motivation	2
1.3 Organization of the dissertation	3
2. Literature Review	4
2.1 Seismic behaviour of bracing frames	5
2.1.1 MBF system	5
2.1.2 OBS system	5
2.2 Dissipative systems for bracing frames	6
2.2.1 EBF-Replaceable bolted link	6
2.2.2 SHD-Steel Hysteretic Devices	7
2.2.3 CBF-MB- Concentrically braced frame with modified braces	8
2.2.4 CBF-INERD project	9
2.3 DISSIPABLE project: DRBrC	11
2.3.1 Predesign	12
2.3.2 Experimental analysis	14
2.3.3 Numerical analysis	16
3. Experimental Studies	22
3.1 Introduction	22
3.2 Drawings	23
3.3 Load Histories	24
3.4 Experimental Setup	24
3.4.1 Procedures before the first test	31
3.4.2 Procedures before a test	31
3.4.3 Procedures during a test	32
3.4.4 Procedures after a test	32
3.5 Material Characterization (Steel's)	33
3.6 Results	37

3.6.1 Test 05: R_S235_HSS_D1_E	38
3.6.2 Test 13: R_StS_HSS_D1_C1	41
3.6.3 Test 19: R_S235_HSS_D2_E	43
3.6.4 Test 20: R_S235_HSS_D2_C1	46
4. Parametric Analysis	49
4.1 Pins: S235vsStS	49
4.1.1 HSS+D1	49
4.1.2 HSS+D2	51
4.2 Plates: S355vsHSS	53
4.2.1 StS+D1	53
4.2.2 StS+D2	55
4.3 D1vsD2	57
4.3.1 S235+HSS	57
4.3.2 StS+S355	60
4.3.3 StS+HSS	61
5. Numerical Analysis	64
5.1 Calibration of the materials	64
5.2 Damage criteria: Ductile damage	67
6. Reusable boxes	73
6.1 Test 19: R_S235_HSS_D2_E vs Test 20R: R_S235*_HSS_D2_E	74
6.2 D1vsD2 with reused boxes	77
6.3 S355vsHSS with reused boxes	77
7. Conclusions and future developments	79
7.1 Conclusions	79
7.2 Future developments	80
References:	81
Annexes	85

List of Figures

Fig. 1.1: Overall view of DRBrC installed in a frame (DISSIPABLE, 2018).	2
Fig. 2.1: Simple frame (dissipative zones in the beams and at the base of the columns) (EC8, 2004).	4
Fig. 2.2: Frames with diagonal bracing centred (a), V-centred (b) and eccentric (c) (Guedes, 2011).	4
Fig. 2.3: John Hancock Center, Chicago (Lynch, 2017) (a); Braced frame models of 30-story (b).	5
Fig. 2.4: Schematic Off-center bracing system.	6
Fig. 2.5: Replaceable link concept (Vayas, 2017).	7
Fig. 2.6: Main components of TRSH bracing system – side view (Vayas, 2017).	7
Fig. 2.7: Sketch of the behaviour of the structure (Vayas, 2017).	8
Fig. 2.8: CBF-MB system (Vayas et al., 2017).	9
Fig. 2.9: INERD U-Connections (Calado & Ferreira, 2004).	9
Fig. 2.10: INERD Pin-Connections (Calado & Ferreira, 2004).	10
Fig. 2.11: Stages of loading of pin connection (Vayas et al., 2017).	10
Fig. 2.12: INERD device, developed in 2004 (left) and the DISSIPABLE device, developed in 2019 (right) (Nascimento, 2020).	11
Fig. 2.13: Connection scheme: (a) top view and (b) side view. (DISSIPABLE, 2020b).	12
Fig 2.14: Moment diagram of the pin at the point of ultimate resistance.	13
Fig 2.15: DRBrC current configuration: (left) top view and (right) side view. Dimensions in mm (Cabrita, 2020).	14
Fig. 2.16: Full list of experimental test specimens (RFCS Project - Dissipable, 2017).	14
Fig. 2.17: Guiding plates	15
Fig. 2.18: Tested weld configurations (Cabrita, 2020).	15
Fig. 2.19: Intrinsic Dissipated Energy (Cabrita, 2020).	16
Fig. 2.20: Scheme of the general methodology used (Farinha, 2020).	16
Fig. 2.21: Mesh of a generic example that achieved accurate results.	17
Fig. 2.22 Node to surface contact specifications (DASSAULT, 2014).	19
Fig. 2.23: Force-displacement curves comparison for test 16 (Cabrita, 2020).	20
Fig. 2.24: Deformation of the pin in test 02: (a) experimental test, (b) numerical model (Cabrita, 2020).	21
Fig. 3.1: Initial full list of experimental test specimens.	22
Fig. 3.2: Dimensions (mm) of DRBrC with spacing D1 (=70mm): (a) Top view, (b) Lateral view (DISSIPABLE, 2021).	23
Fig. 3.3: Dimensions (mm) of DRBrC with spacing D2 (=90mm): (a) Top view, (b) Lateral view (DISSIPABLE, 2021).	24
Fig. 3.4: Overall view of LERM.	25
Fig. 3.5: General overview of experimental setup (DISSIPABLE, 2021).	26
Fig. 3.6: View from north of the experimental setup.	27
Fig. 3.7: View from south of the experimental setup.	28
Fig. 3.8: Position of the displacement transducers and direction criterion. View from above (Dimensions in mm) (DISSIPABLE, 2021).	29
Fig. 3.9: Location of the load cell. View from above (Dimensions in mm) (DISSIPABLE, 2021).	29
Fig. 3.10: Examples of instruments selected for tests: (a) Load cell, (b) lateral displacement transducer and (c) principal displacement transducer and wire transducer (DISSIPABLE, 2021).	30
Fig. 3.11: Examples of equipment used: (a) Computer setup, (b) software and (c) actuator manual control (DISSIPABLE, 2021).	30
Fig. 3.12: Video camera view (DISSIPABLE, 2021).	31
Fig. 3.13: Computer and Control Table control of parameters during a test.	32
Fig. 3.14: Instron test machine (DISSIPABLE, 2021).	33
Fig. 3.15: Test 06 DRBrC specimen material (DISSIPABLE, 2021).	34

Fig. 3.16: Tensile test specimens of S355, HSS, StS and S235 materials, respectively (DISSIPABLE, 2021).	34
Fig. 3.17: Tensile test specimen S235*(1) – (a) removed pin and (b) pin processing (DISSIPABLE, 2020).	34
Fig. 3.18: Dimensions of S235 material tensile test specimen (DISSIPABLE, 2021).	35
Fig. 3.19: Dimensions of StS material tensile test specimen (DISSIPABLE, 2021).	35
Fig. 3.20: Dimensions of S355 material tensile test specimen (DISSIPABLE, 2021).	35
Fig. 3.21: Dimensions of HSS material tensile test specimen (DISSIPABLE, 2021).	35
Fig. 3.22: Dimensions of S235*(1) material tensile test specimen (DISSIPABLE, 2021).	35
Fig. 3.23: Dimensions of S235*(2) material tensile test specimen (DISSIPABLE, 2021).	36
Fig. 3.24: Tested specimens of – (a) S355, HSS, StS and S235 materials, respectively and (b) S235*(1) and S235*(2) material (DISSIPABLE, 2021).	36
Fig. 3.25: Engineering and true stress-strain curves for all the materials.	37
Fig. 3.26: Codename for the experimental test configurations, which is Test 26.	38
Fig. 3.27: Specimen model of test number 5.	38
Fig. 3.28: Load history for test number 5.	39
Fig. 3.29: Force-Displacement curve of test number 5.	39
Fig. 3.30: Experimental test number 5: (a) and (b) pin failure.	40
Fig. 3.31: Accumulated Dissipated Energy curve of test number 5.	40
Fig. 3.32: Specimen model of test number 13.	41
Fig. 3.33: Load history for test number 13.	41
Fig. 3.34: Force-Displacement curve of test number 13.	42
Fig. 3.35: Experimental test number 13: (a) pin failure; (b) division of the pin.	42
Fig. 3.36: Accumulated Dissipated Energy curve of test number 13.	43
Fig. 3.37: Specimen model of test number 19.	44
Fig. 3.38: Load history for test number 19.	44
Fig. 3.39: Force-Displacement curve of test number 19.	45
Fig. 3.40: Experimental test number 19: (a) failure mode; (b) pin elongation.	45
Fig. 3.41: Accumulated Dissipated Energy curve of test number 19.	46
Fig. 3.42: Load history for test number 20.	47
Fig. 3.43: Force-Displacement curve of test number 20.	47
Fig. 3.44: Experimental test number 20: (a) failure mode; (b) pin failure.	48
Fig. 3.45: Accumulated Dissipated Energy curve of test number 20.	48
Fig. 4.1: Specimen S235_HSS_D1 (a) and StS_HSS_D1 (b).	49
Fig. 4.2: Comparisons between S235_HSS_D1 (red) with StS_HSS_D1 (green).	50
Fig. 4.3: Specimen S235_HSS_D2 (a) and StS_HSS_D2 (b).	51
Fig. 4.4: Comparisons between S235_HSS_D2 (red) with StS_HSS_D2 (green).	52
Fig. 4.5: Specimen StS_S355_D1 (a) and StS_HSS_D1 (b).	53
Fig. 4.6: Comparisons between StS_S355_D1 (red) with StS_HSS_D1 (yellow).	54
Fig. 4.7: Specimen StS_S355_D2 (a) and StS_HSS_D2 (b).	55
Fig. 4.8: Comparisons between StS_S355_D2 (red) with StS_HSS_D2 (yellow).	56
Fig. 4.9: Specimen S235_HSS_D1 (a) and S235_HSS_D2 (b).	57
Fig. 4.10: Comparisons between S235_HSS_D1 (red) with S235_HSS_D2 (blue).	59
Fig. 4.11: Specimen StS_S355_D1 (a) and StS_S355_D2 (b).	60
Fig. 4.12: Comparisons between StS_S355_D1 (red) with StS_S355_D2 (blue).	61
Fig. 4.13: Specimen StS_HSS_D1 (a) and StS_HSS_D2 (b).	61
Fig. 4.14: Comparisons between StS_S355_D1 (red) with StS_S355_D2 (blue).	62
Fig. 5.1: Evolution of isotropic and kinematic hardening for combined hardening model under uniaxial stress state (adapted from ABAQUS, 2012).	65
Fig. 5.2: Representation of the Bauschinger Effect (Stahleisen & Hoff, 1958).	65
Fig. 5.3: Plastic range calibration: (a) pin S235, (b) pin StS, (c) plate S355 and (d) plate HSS.	66
Fig. 5.4: Stress-strain curve with progressive damage degradation (Cabrita, 2020).	67
Fig. 5.5: Force-Displacement Curve of the simulation without damage criteria over the experimental one (Box 23: R_StS_S355_D2_E).	69
Fig. 5.6: Force-Displacement Curve of the simulation with damage criteria over the experimental one (Box 23: R_StS_S355_D2_E).	69

Fig. 5.7: Force-Displacement Curve of the simulation without damage criteria over the experimental one (Box 22: R_S235_HSS_D2_C3).	70
Fig. 5.8: Force-Displacement Curve of the simulation with damage criteria over the experimental one (Box 22: R_S235_HSS_D2_C3).	70
Fig. 5.9: StS pin failure: experimental (a) and numerical (b).	71
Fig. 5.10: Rupture trend of the StS pin numerically.	71
Fig. 5.11: Force-Displacement Curve of the simulation without damage criteria over the experimental.	72
Fig. 6.1: Failure mode of test number 19 (a) and numeration of the plates to evaluate de ovalization (b) & (c).	73
Fig. 6.2: (a) pin elongation (b) box ovalization.	73
Fig. 6.3: Load history for test number 19 and 20R.	74
Fig. 6.4: Force-Displacement curve of test number 19 and 20R.	75
Fig. 6.5: Experimental test number 20R: (a) failure mode; (b) pin failure.	75
Fig. 6.6: Accumulated Dissipated Energy curve of test number 19 and 20R.	76
Fig. 6.7: Force-Displacement curve of test number 19 (a) and 20R (b), with the progress of the force.	76
Fig. 6.9: Comparisons between S235*_S355 (red) with S235*_HSS (dark blue).	78
Fig 7.1: Devices with higher and lower values.	79

List of Tables

Tab. 2.1: Forces and deflections of pin connection (Plumier et al., 2004)	1313
Table 2.2: Geometric limitations for DRB systems (based on INERD devices) (Pluriel et al 2004 and Vayas et al 2017).	1313
Tab 2.3: Predesign of the pin-device (Cabrita, 2020).	1313
Tab. 3.1: Final list of tested configurations on the second phase.	2322
Tab. 3.2: ECCS load history (ECCS, 1986).	2423
Tab. 3.3: Principal quantities to be measured.	2827
Tab. 3.4: Measuring instruments configurations.	28
Tab. 3.5: Material main characteristics determined by SOFMAN.	32
Tab. 3.6: Dimensions of the tensile test specimens (dimension in mm).	3635
Tab. 3.7: Main engineering characteristics obtained from the tensile tests.	3736
Tab. 3.8: Results for experimental test 5.	4039
Tab. 3.9: Results for experimental test 13.	4342
Tab. 3.10: Results for experimental test 19.	4645
Tab. 3.11: Results for experimental test 20.	4847
Tab. 4.1: Variation percentage of Force and Energy.	5150
Tab. 4.2: Variation percentage of Force and Energy.	5352
Tab. 4.3: Variation percentage of Force and Energy.	5554
Tab. 4.4: Variation percentage of Force and Energy.	5756
Tab. 4.5: Variation percentage of Force and Energy.	5958
Tab. 4.6: Variation percentage of Force and Energy.	6160
Tab. 4.7: Variation percentage of Force and Energy.	6362
Tab 5.1: Combined hardening parameters	6665
Tab. 5.2: Damage parameters for the tensile tests.	6867
Tab. 6.1: Ovalization of the plates HSS and the pin S235 of the box 19.	7372

List of Symbols

Latin upper-case letters

C	Kinematic hardening parameter
C_1	Initial Hardening Parameter
D	Damage criteria
D1	Axial distance between the external eye-bar plates (70mm)
D2	Axial distance between the external eye-bar plates (90mm)
E	Modulus of elasticity
G_f	Fracture energy
I	Second moment of area of the pin cross section
L	Equivalent length
M_{pl}	Plastic resistance moment of the pin
P_{max}	Maximum design load of the connection
P_y	Design yield load of the connection
Q_∞	Isotropic hardening parameter
W_{pl}	Plastic section modulus

Latin lower-cases letters

a	Distance between the external the internal eye-bar plate
b	Pin width, Isotropic hardening parameter
b_{ext}	Width of the external eye-bar plates
b_{int}	Width of the internal eye-bar plates
d_{ext}	Axial distance between the external eye-bar plates
d_{int}	Axial distance between the internal eye-bar plates
f_s	Friction Shear Stress
f_u	Tensile strength of the material
f_y	Yield strength of the material
h	Pin height
h_{ext}	Height of the external eye-bar plates
h_{int}	Height of the internal eye-bar plates
l	Axial distance between medial axis of external eye-bar plate and the edge of the hole
q	Behaviour coefficient
s_{ext}	Distance from the free edge of the external eye-bar plate and the edge of the hole
s_{int}	Distance from the free edge of the internal eye-bar plate and the edge of the hole

t_{ext}	Thickness of the external eye-bar plates
t_{int}	Thickness of the internal eye-bar plates
\bar{u}^{pl}	Equivalent true plastic displacement
\bar{u}_f^{pl}	Equivalent true plastic displacement at failure

Greek upper-case letters

Φ	Pin diameter
--------	--------------

Greek lower-case letters

α	Imperfection factor
$\bar{\alpha}$	Equivalent back stress
γ	Kinematic hardening parameter
γ_1	Kinematic hardening parameter
δ_{II}	Ultimate displacement
δ_{lim}	Deformation capacity displacement
δ_y	Yield displacement
$\bar{\epsilon}^{\text{pl}}$	Equivalent plastic strain
$\bar{\epsilon}_0^{\text{pl}}$	Equivalent plastic strain at the onset of damage
ϵ_e	Engineering Strain
$\bar{\epsilon}_f^{\text{pl}}$	Equivalent Plastic Strain at Fracture
μ	Friction Coefficient
ρ	Normal Pressure
σ	(Damage) Stress tensor
$\bar{\sigma}$	Equivalent stress or Von Mises stress
σ^0	Yield stress at zero plastic strain
σ_u	Ultimate stress
σ_{y0}	Stress at the onset of damage

List of Acronyms

C	Constant imposed amplitudes
CBF	Concentrically Braced Frames
CBF-MB	Concentrically Braced Frame with Modified Braces
DISSIPABLE	Fully Dissipative and Easily Repairable Devices for Resilient Buildings with Composite Steel-Concrete Structure (project acronym)
DRBrC	Dissipative Replaceable Bracing Connection
EBF	Eccentrically Braced Frame
EC	European Community
ECCS	European Convention for Constructional Steelwork
EC8	Eurocode 8
GP	Guiding Plate
HSS	High Strength Steel
INERD	Two Innovations for Earthquake Resistant Design (project acronym)
IST	Instituto Superior Técnico
LERM	Laboratório de Estruturas e Resistência de Materiais
LVDT	Linear Variable Differential Transformer
MBF	Mega Braced Frames
MRF	Moment Resisting Frame
MSSH	Moon Shaped Steel Hysteretic
NEHRP	National Earthquake Hazards Reduction Program
NTUA	National Technical University Athens
OBS	Off-center Bracing System
RFCS	Research Fund for Coal and Steel
SHD	Steel Hysteretic Devices
StS	Special treatment Steel
TRSH	Triangular Steel Hysteretic
UL	Universidade de Lisboa
USA	United States of America

1. Introduction

Many years have passed but it cannot be forgotten: the 1755 earthquake that shook Lisbon, the rest of the south side and the Algarve coast was one of the largest and powerful earthquakes in early modern Europe. It is estimated to have reached a magnitude of 8 to 9 on the Richter scale, just like Tōhoku earthquake, Japan March 11, 2011. Humanity must have the wisdom to realize that in fact there is life under our "feet" (Ferreira, 2021), especially civil engineers when designing and dimensioning structures, where they must be concerned with preventing the collapse of the structure, prolonging service life and, most importantly, protecting/keeping human life safe (NEHRP, 1997).

An earthquake is a natural phenomenon resulting from a violent rupture inside the earth's crust, corresponding to the sudden and unexpected release of a large amount of energy, causing vibrations that propagate in all directions to a vast surrounding area. In most cases earthquakes are due to movements along geological faults that exist at the contact between the different tectonic plates that make up the Earth's surface, which move against each other (ProCiv, 2017). They are measured using two scales, the Modified Mercalli Scale (I to XII) characterized by the observation of the damage produced, and the Richter Scale (1 to 9 but can be unlimited)-this measures the magnitude of the earthquake (energy released).

In Portugal, successive generations of earthquake-resistant design codes entered into force, namely in 1958, 1983 and, more recently, the Eurocode 8 in 2019 (published as a Portuguese standard in 2010).

The concern of seismic events should not be exclusive to new structures, but also in rehabilitation. It is known that today there are already many buildings where the construction incorporates materials more suitable and with greater resistance to the effects of an earthquake. What about rehabilitation? At a time when the rehabilitation of buildings is increasing it would be indispensable that the same improvement works could also serve to create more structural safety in buildings. According to Carlos Mineiro Aires, in Portugal 60% of the existing buildings were built more than 30 years ago, and 14% will need a medium to very large structural repair. Besides this, in terms of legislation "Portugal is quite demanding at this level and was also a pioneer in the legal requirements for the calculation of structures against seismic actions", considers this responsible (Construir, 2018).

The Dissipative Replaceable Bracing Connection (DRBrC) device is applied to braced frames, and these can be used for rehabilitation or retrofit (Papavasileiou et al., 2020).

1.1 DISSIPABLE-DRBrC

DISSIPABLE is an acronym of two words: DISSIPATIVE plus reparABLE, a “Research Fund for Coal and Steel” program organized by the European Community (EC) that is developing anti-seismic devices that dissipate much of the energy from an earthquake and are easily repairable. Many of these devices are described in the ECCS Innovative Anti-seismic Devices and Systems document developed by Vayas, 2017, in which some are explicit in this dissertation in chapter 2.

However, this dissertation will put much more emphasis on the DRBrC device. This hysteretic device was elaborated intended for steel constructions and mixed steel-concrete structures, installed in bracketed frames (fig. 1.1).

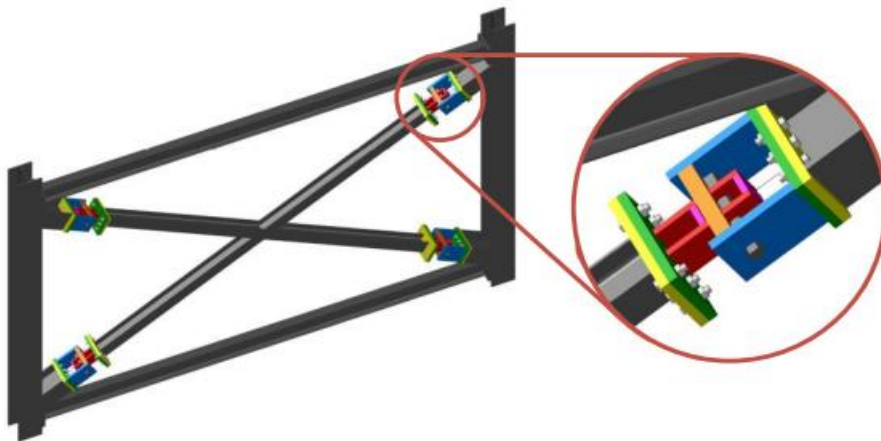


Fig. 1.1: Overall view of DRBrC installed in a frame (DISSIPABLE, 2018).

This is a hysteretic device consisting of a steel pin fuse.

To study this device there were several hypotheses of steel conjugations, both in the cases and in the pins, and distancing between internal plates, which are presented in figure 3.1. The analysis variables are the maximum force it can reach, the maximum number of cycles and the capacity to accumulate dissipated energy.

1.2 Personal Motivation

The biggest motivation for this final dissertation is to have a better knowledge in Earthquake Engineering area, not to know in detail what an earthquake is, this being a topic under discussion in Geophysics, but to develop and study solutions capable of reducing collateral damage mainly in structures. Perhaps improving the quality of human life and extending the life span of structures.

It is also a great privilege to work on a European project in cooperation with Italian, Greek and German colleagues.

1.3 Organization of the dissertation

The next chapter discusses some studies conducted in recent years and with special emphasis on the essays prepared by previous colleagues, DISSIPABLE 2019.

Chapter 3 presents the experimental tests carried out at the laboratory, namely in terms of the test setup, instrumentation and loading protocols, as well as the material tests (tensile tests carried out to characterize the different materials used).

In chapter 4 all tests are compared in a parametric analysis with emphasis on forces, number of cycles and accumulated dissipated energies.

A numerical analysis was also performed resorting to the ABAQUS software to compare experimental tests with numerical simulations (chapter 5).

Chapter 6 presents the experimental results of the devices under study, when repaired and reused after a first strong motion earthquake.

Finally, some conclusions and future development ideas are presented in the last chapter.

2. Literature Review

Frames are the trademark of steel structures. In short, a simple frame consists of two columns supporting a beam at their top (2D). It is also very common to have frames in steel-concrete composite structures, but in this case the slab is usually heavy due to the characteristics of the concrete.

With the evolution of construction and the design of structures, bracing were developed, which is the introduction of one or more metal bars, typically two, which serve to support lateral forces (earthquake and wind) and distribute vertical forces (gravity and overloads) by the lower columns. As mentioned above, its main role offers more rigidity to the structure itself, that is, one bar works in compression and the other in tension. They may designate braced frames.

The major differences between simple and braced frames are found in the support conditions and in connections. While simple frames (MRF's) are embedded in the base and have rigid connections, braced frames (CBF's) are articulated both in the base and in the beam-column connections (Guedes, 2011).

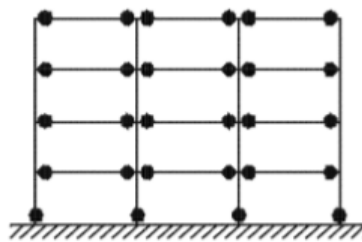


Fig. 2.1: Simple frame (dissipative zones in the beams and at the base of the columns) (EC8, 2004).

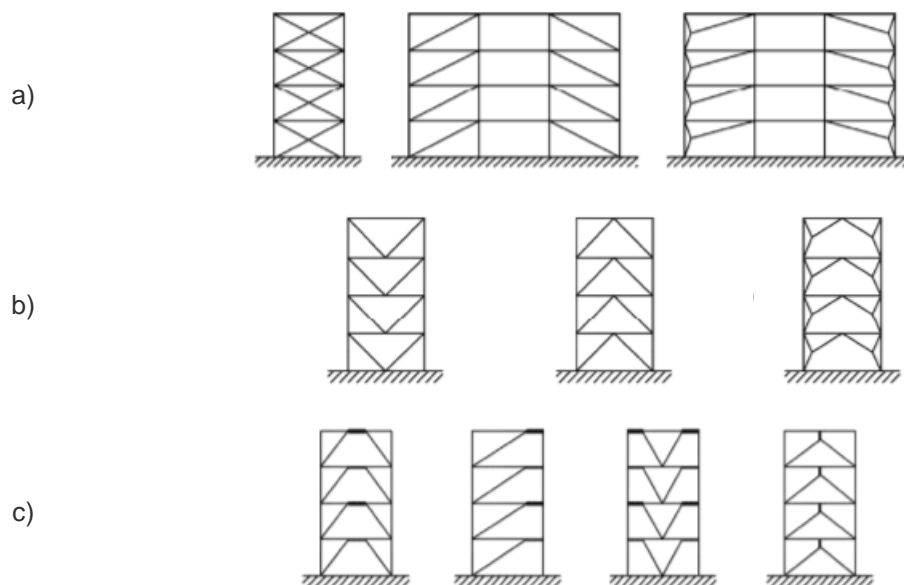


Fig. 2.2: Frames with diagonal bracing centred (a), V-centred (b) and eccentric (c) (Guedes, 2011).

2.1 Seismic behaviour of bracing frames

Currently, the trend to use tall steel structures has increased the need to find more efficient and economical lateral load resisting systems.

2.1.1 MBF system

An American study (H. Sheikh and A. Massumi, 2014) investigated the structural performance of shoring configurations under earth movements in PERFORM-3D software. Four models were used: concentric bracing (CBF) and 3 different types of mega bracing (MBF), present in figure 2.3. This technique is widely used in the USA as in the famous Empire State Building and the John Hancock Center (Taranath BS, 1988 and Stafford Smith B, 1991).

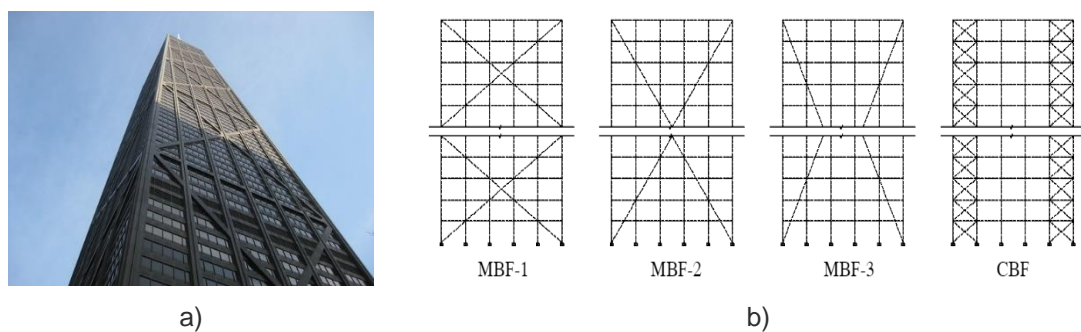


Fig. 2.3: John Hancock Center, Chicago (Lynch, 2017) (a); Braced frame models of 30-story (b).

The purpose of this report was to study the seismic behaviour of mega-braced structures, by studying the comparative analyses of roof drift, inter-story drift and energy absorption. The result of this study showed that the roof drifts in MBF are 12%-70% for 18-story frames and 10%-55% for 30-story frames lower than CBF. The reduction in inter-story drifts for 18- and 30-story frames is on average equal to 35% and 25%, respectively. Thus, if the goal of adding structural bracing is to reduce lateral displacement, the use of MBF-1 and MBF-2 has the greatest effect on this parameter, especially at the upper floors. Dynamic analyses indicate that MBFs reduce the compressive axial force of column bases and base shear compared to CBF. The reduction in compressive axial force of column bases compared to CBF is on average equal to 32% and 18% for 18 floors and 30 floors, respectively. In the cases studied, MBF-2 has the highest impact on the reduction of the base shear coefficient. The comparative analyses performed confirm that MBF-1 is the most cost-effective.

2.1.2 OBS system

Another type of braced gantry crane developed in Canada is called the OBS, Off-center Bracing System (Estekanchi, Soltani & Vafai, 2004). The midpoint of the diagonal member is connected to the corner joint using a brace member with a relatively low stiffness, thus forming a three-brace member system.

The main disadvantage of CBF's, when considering earthquake resistance, is their relatively high stiffness to strength ratio and low deformation capacity (Newmark & Resenblueth, 1971 and Chopra, 2001). OBF's systems can be considered as an improvement over CBF's, providing higher deformation capacity, lower stiffness, and higher energy dissipation through improved hysteresis loop characteristics. The basic idea behind the eccentric bracing system is to provide a bending yielding mechanism that allows for greater deformation and energy dissipation in the nonlinear range (Naeim, 2002). The idea behind this bracing system is to utilize the nonlinearity introduced by the geometric configuration of the bracing system to produce a certain amount of seismic isolation. The degree of nonlinearity depends on the eccentricity of the tension diagonal and relative stiffness of bracing frames. The general configuration of the system is represented in figure 2.4.

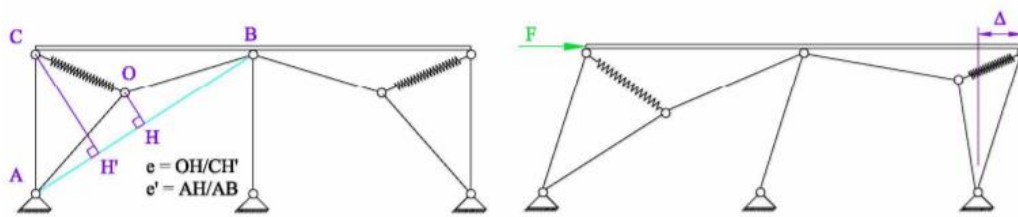


Fig. 2.4: Schematic Off-center bracing system.

It was concluded from the study that the general characteristics of Off-center clamps are like a base insulation system acting on a whole story level system at the lowest level of buildings. As the diagonal that dissipative the earthquake energy has a low stiffness, it ends up being fragile to large displacements (higher floors). In buildings equipped with off-center braces, the floor deflections at the lowest level are considerably higher than their braced gantry counterparts, and the effective damping of off-center braids is typically about half that of their counterparts with CBFs, where their effective free vibration period is about twice as high (Estekanchi et al., 2004).

2.2 Dissipative systems for bracing frames

However, research for the development and improvement of braced frames has progressed to the ideology of placing dissipative systems of seismic actions. In the report of Innovative anti-seismic devices and systems edited by Ioannis Vayas, 2017, several interesting ways to dissipate energy coming from earthquakes are present.

2.2.1 EBF-Replaceable bolted link

Interesting fuse system investigated is the replaceable bolted link (Taucer et al., 2014), a dual structure system, obtained by combining steel eccentrically braced frames (EBFs) equipped with removable bolted links (Figure 2.5), and moment resisting frames (MRFs). The bolted links are intended to provide the energy dissipation capacity and to be easily replaceable. The flexible

MRFs provide the necessary re-centering capability to the structure, defined as the capacity of minimizing the residual displacement at the end of the seismic action.

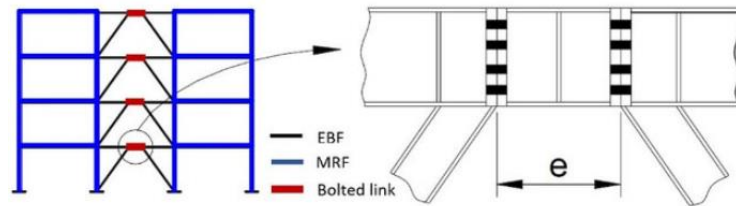


Fig. 2.5: Replaceable link concept (Vayas, 2017).

2.2.2 SHD-Steel Hysteretic Devices

Steel Hysteretic Devices (SHD) represent an effective solution to increase the capability of structures to dissipate seismic energy. Yield may be obtained through uniaxial tension (or compression), shear, torsion and bending (LESSLOSS, 2007 and Medeot, 2004).

Among SHD devices, the Triangular Steel Hysteretic (TRSH) device is an effective element for the implementation into a structural bracing system, e.g.:

- The bending curvature produced by a transverse force applied at the end of the triangular plates is uniform over the full height of the plate.
- It can undergo large inelastic deformations without curvature concentrations.

The operational principle of a bracing system implementing TRSH devices and its qualitative kinematics. A possible layout of the connection of braces with a beam by means of a TRSH is shown in figure 2.6.

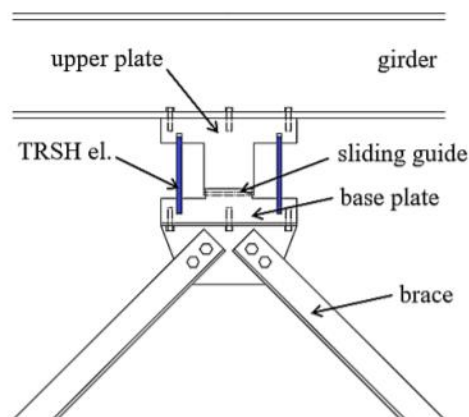


Fig. 2.6: Main components of TRSH bracing system – side view (Vayas, 2017).

Among SHD the Moon Shaped Steel Hysteretic (MSSH) device, shown, was developed as damper for base isolated structures. The isolator consists of a flat surface slider resp. elastomeric bearing and MSSH devices.

To reach a high strain for the MSSH device without material failure, the utilized steel must possess the characteristics of very distinctive flow behaviour. The innovative seismic resistant system with MSSH devices consists of the introduction of these devices at every building storey: considering a concentric bracing system, the devices are introduced at the end of every brace element (figure 2.7). Under strong seismic motion inelastic deformations are restricted to the MSSH devices, which dissipate a large amount of input energy, leaving the rest of the structure elastic and undamaged.

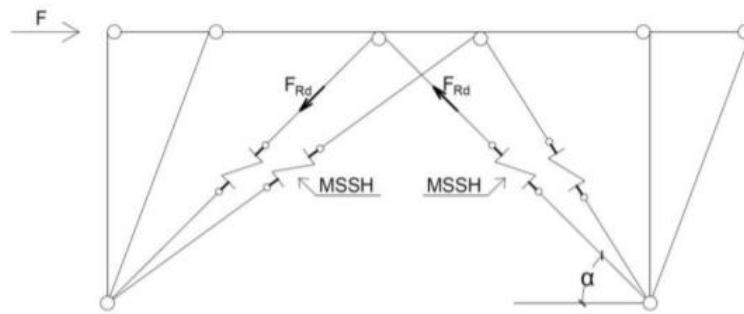


Fig. 2.7: Sketch of the behaviour of the structure (Vayas, 2017).

Repair works are easy, since they are restricted to the MSSH devices which are not subjected to vertical loads, as they are placed between storey levels. The devices are easy to replace and manufacture, offering a cost-effective solution.

2.2.3 CBF-MB- Centrally braced frame with modified braces

The innovations of this system are the introduction of a horizontal intermediate member called the splitter beam and modified frames with the variable "H" shaped weld. The modified brace are the main dissipative elements, while the splitter beam can partially participate. CBF-MB systems are representative of the strut frame family. Their topology does not differ much from the topology of the classical diagonal transverse brace frame. In this sense, they can be successfully implemented in office and commercial buildings and in industrial constructions for pipe support frames or engineering facilities (Vayas et al., 2017).

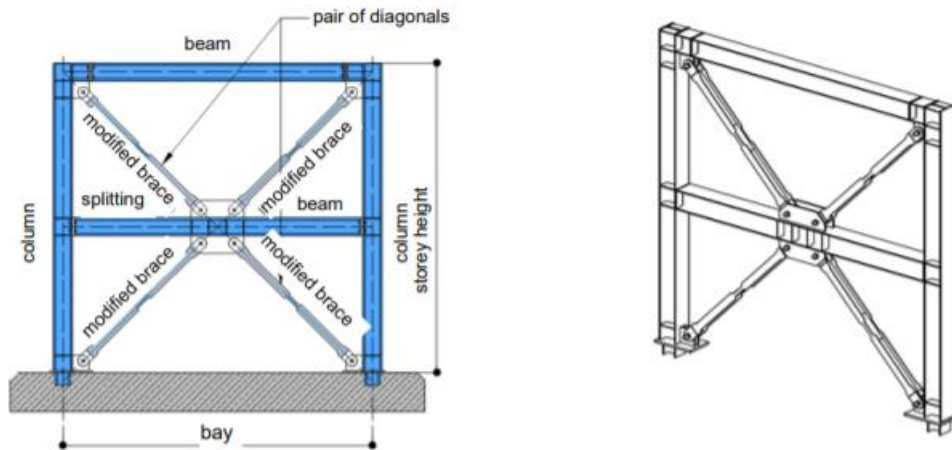


Fig. 2.8: CBF-MB system (Vayas et al., 2017).

2.2.4 CBF-INERD project

Keeping the trademark image of cantilevered frames that are those bars in "X's" the INERD project developed and investigated some dissipative systems (Plumier et al, 2004). With the action of lateral forces, braced frames form plastic hinges in the bracing connections with the beam-column structure and thus introduced energy dissipating devices provided by these forces.

The first test outlined was The INERD U-bond (Figure 2.9), which consists of the dissipative element of thick plates with variable radius, length, thickness, and position, while the design is essentially controlled by its deformation capacity. Research has led to the general conclusion that the best performance of the U-shaped device is obtained by increasing the thickness and decreasing the radius (Calado & Ferreira, 2004). This dissipative connection, due to its high deformability, is intended to be applied in structures that are not too sensitive to large displacements, buildings with a limited number of floors.

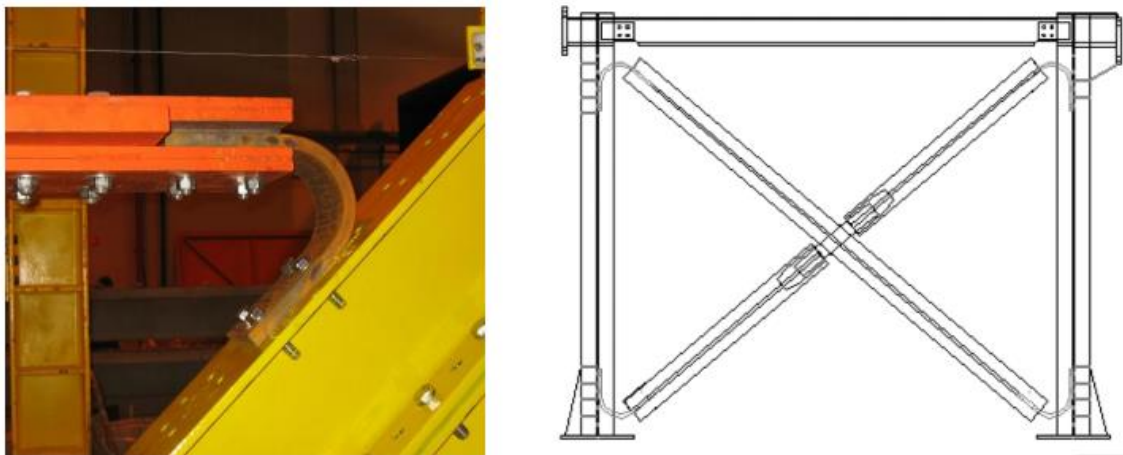


Fig. 2.9: INERD U-Connections (Calado & Ferreira, 2004).

With this limitation, a system was created that would revolutionize the dissipative systems philosophy. The INERD stud connection (Figure 2.10) is materialized by a pair of outer plates, connected to the column flanges, and two inner plates, connected to the brace. Last but foremost, a pin, the dissipative element, passes through all the plates. The axial force of the strut is transferred to the pin by the contact of the plates, which is in this way subjected to bending and its performance properties are exploited. Under a strong seismic event, the damage is restricted to the pin, allowing INERD pin connections to be easily repaired with less material, time, and equipment.

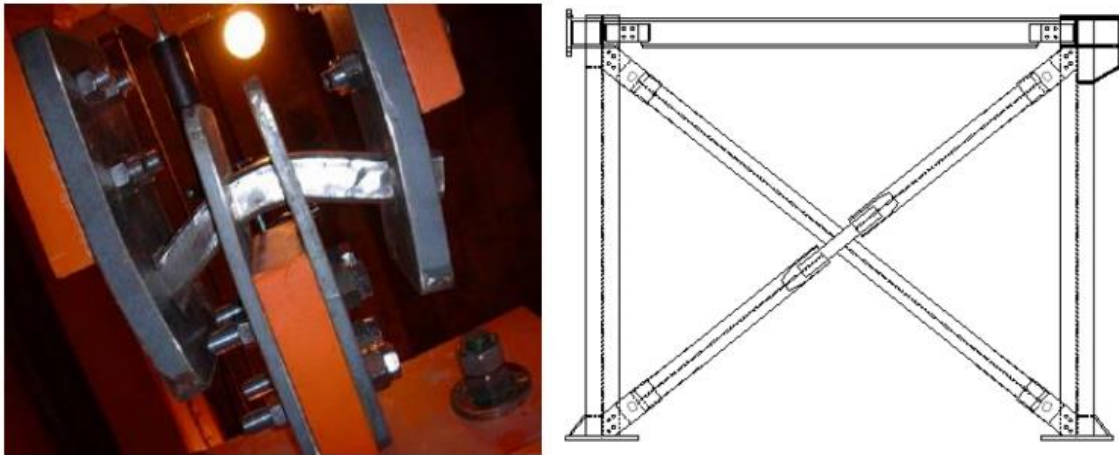


Fig. 2.10: INERD Pin-Connections (Calado & Ferreira, 2004).

To demonstrate the response of the dissipative element, the pin, can be modeled with a beam (Figure 2.11). In the first loading phase, the supports act as pins, so the beam is simply supported, and the moment is concentrated at mid-span, when the acting moment reaches the plastic moment strength of the pin, hinges are formed, and the location of the inner plates and significant deformation of the pin occurs. In the second loading phase, the end supports begin to act as fixed, further increasing the bond strength, until plastic hinges also form at the location of the outer plates (supports). In the final loading phase, the strength of the pins has been fully exploited and the remaining bond stiffness is given due to strain hardening and expansion of the plastic zones.

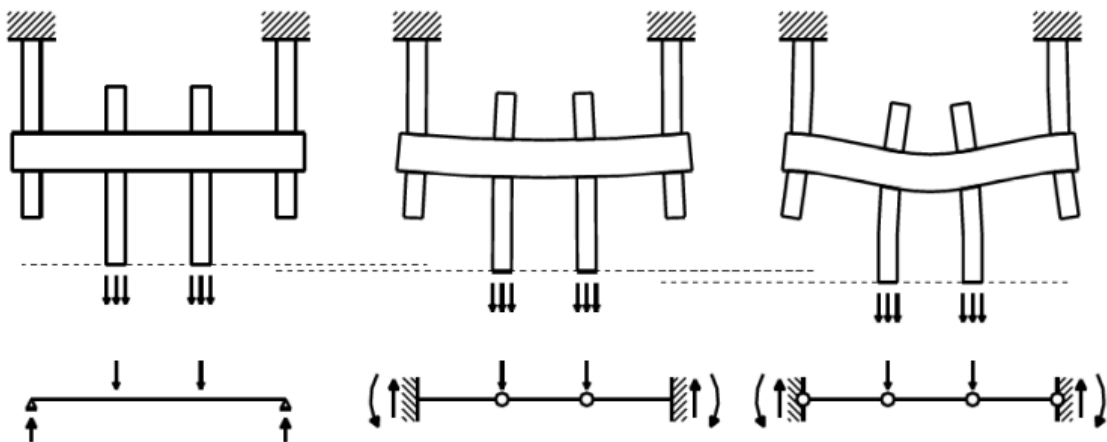


Fig. 2.11: Stages of loading of pin connection (Vayas et al., 2017).

The innovative pin connection has proven to be applicable to small, medium, or tall steel buildings, as they demonstrate adequate stiffness and ductility (Vayas et al., 2017). The proposed modifications to the INERD pin devices based on the issues consist of using appropriate spacers between the outer and inner plates of the eye bar, which would not interfere with the assembly, to avoid bending of the plates. Together with the introduction of the end plates welded to the outer and inner plates of the eye bar and connected by means of screws to the column and brace members, allowing easier replacement of the device.

2.3 DISSIPABLE project: DRBrC

Taking advantage of the fact that the use of bracings, or trusses, is an effective way to respond to a seismic event, because one bar works in compression while the other works in tension, there are studies of various types of trusses with local devices that have the function of dissipating the energy from an earthquake. Over the last 20 years these devices have been improved fig. 2.12.

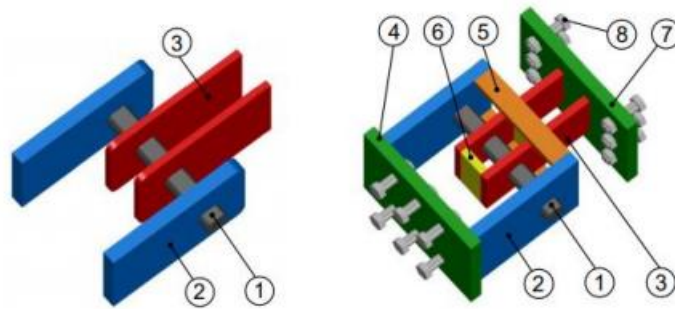


Fig. 2.12: INERD device, developed in 2004 (left) and the DISSIPABLE device, developed in 2019 (right) (Nascimento, 2020).

As shown in Figure 2.12, these two devices have a similar concept, in their dissipative function. The main difference in this evolution is that, once the pin (1) is damaged, it can be fully replaced. To achieve this, instead of welding the internal plates (3) to the diagonal member of the bracing, they are welded to a base plate (7) and the device is fixed to the diagonal member using bolts (8). The connection to the main structure is identical: the external plates (2) are welded to the opposite base plate (4) and this its bolts are used to fix this end of the device. It was also adopted spacers (5) and (6) to help the concentration of plastic deformations on the pin. Without then, like the INERD device, the external and internal plates would withstand deformation.

The main goal of developing this device is to create a mechanism capable of dissipating large amounts of energy so that the main structure does not suffer extensive damage throughout a strong earthquake. In addition, the design of the DRBrC was thought so that it would fill the lack of performance reparability, existent in other similar devices. As it is crucial to restore buildings and its functions as quickly as possible, this device was planned, so that it could be easily replaced, resulting in its considerable low weight (100Kg). This device consists of a pin fuse, mounted in the bracing system. The concept of this connection is a pin that is subjected to four-

point bending which behaves in a relatively simple and predictable way. It is supposed to fail due to low cycle fatigue, by accumulating permanent plastic deformations. In a broad sense the following points summarize the principal objective for the DRBrC (Farinha, 2020):

- Reduced failure probabilities.
- Reduced consequences from failure, in terms loss of lives, structural and non-structural damage, and negative economic and social consequences.
- Reduced time to recovery (restoration of a specific system to its functionality).

2.3.1 Predesign

DRBrC is a male-female split case which is connected by a metal pin. The DRBrC system is made up of a dissipative pin and of non-dissipative elements including steel plates and stiffeners. Stiffeners are welded among plates to improve the dynamic stability and the dissipative capacity of the system. During cyclic/seismic actions, the pin is subjected to plastic deformation due to the relative displacements between internal and external plates (along force direction).

The parameters directly influencing the behaviour of the system are the length of the pin (defined in relation to connected elements - l), the geometry of the section and its main dimensions, the plates' thickness (internal and external), the resulting free length of the pin (a) and the mechanical properties of the materials adopted for the different components (Fig. 2.13).

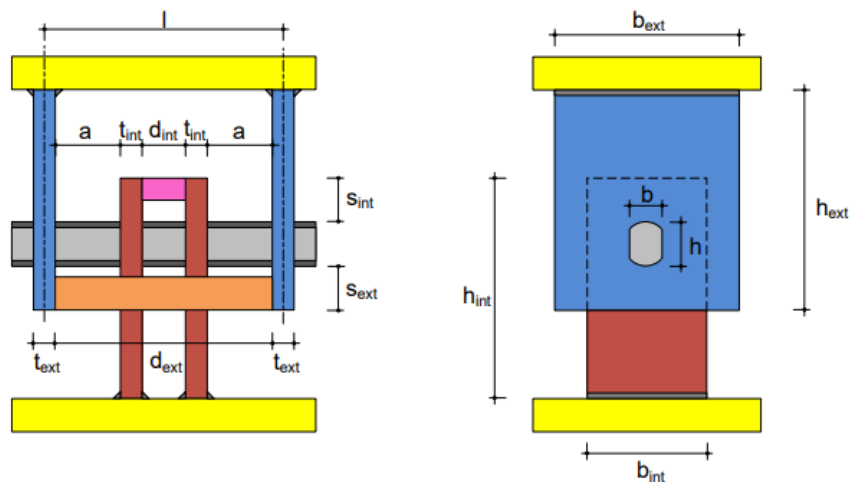
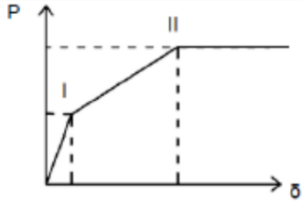


Fig. 2.13: Connection scheme: (a) top view and (b) side view. (DISSIPABLE, 2020b).

The starting point for pre-dimensioning DRBrC was the maximum force achieved in LERM, where the load cell only registered up to 500kN (Cabrita, 2020). This requirement was verified taking into consideration the pin connection ultimate resistant force definition presented in Table 2.1 and the moment diagram of the simplified beam model depicted on Figure 2.14, where a is the distance between the external the interior eye-bar plates.

Tab. 2.1: Forces and deflections of pin connection (Plumier et al., 2004)

	Force P	Deformation δ
Point I "yielding y"	$P_y = \frac{2 \times M_p}{a}$	$\delta_y = 1.5 \times \frac{M_p}{EI} \times l^2 \times \frac{a}{6} \times (3 - 4\alpha)$
Point II "ultimate u"	$P_u = \frac{4 \times M_p}{a}$	$\delta_{II} = 0.2 \times a$
Deformation capacity		$\delta_{lim} = 0.4 \times a$

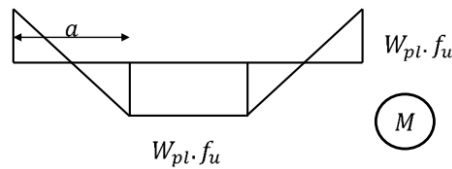


Fig 2.14: Moment diagram of the pin at the point of ultimate resistance.

Table 2.2: Geometric limitations for DRB systems (based on INERD devices) (Plumier et al., 2004 and Vayas et al., 2017).

Internal plates	$t_e \geq 0.75 \times h$
External plates	$t_i \geq 0.5 \times t_e$
Pin section dimensions	$h \leq b \leq 2 \times h$
Distance between plates	$a \geq h$
Steel grade	$pin < plate$

Using previously tested values, which also serve as a comparison, along INERD (Calado & Ferreira, 2004):

Tab 2.3: Predesign of the pin-device (Cabrita, 2020).

Pin	f_u (Mpa)	b (mm)	h (mm)	Φ (mm)	a (mm)	W_{pl} (mm^3)	M_u $= W_{pl} \times f_u$ (kNm)	P_u $= \frac{4 \times M_p}{a}$ (kN)	$P_{m\acute{a}x.}$ (kN)
Chamfered	360	40	50	-	80	2×10^4	7.1	354	<500
Circular	360	-	-	50	80	2.1×10^4	7.5	375	

After all the necessary checks and balancing, the result is this:

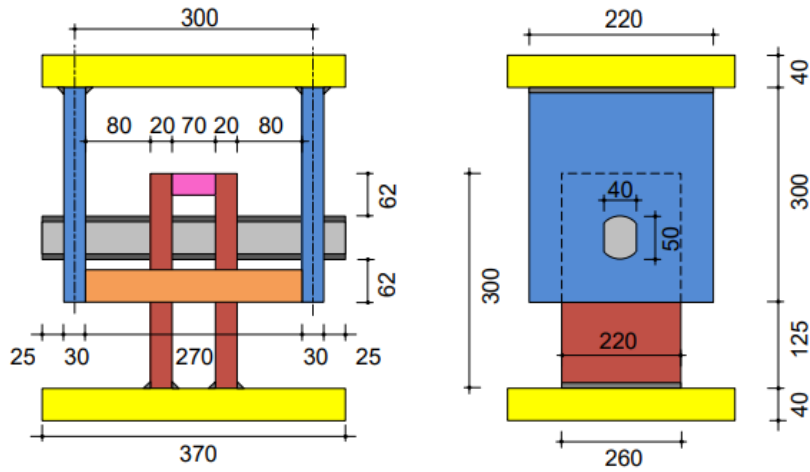


Fig 2.15: DRBrC current configuration: (left) top view and (right) side view. Dimensions in mm (Cabrita, 2020).

2.3.2 Experimental analysis

Previously to my dissertation, 8 tests were performed with different device configurations (fig 2.16).

No of test configuration	Configuration code (*)	Pin shape	Pin Φ	Pin steel	External plate thickness	External plate dimensions	Number of internal plates	Internal plate thickness	External plate dimensions	Plates steel	Load protocol
1	R_S235_S355_E	R	50	S235	30	220x300	2	20	140x300	S355	E
2	R_S235_S355_C1	R	50	S235	30	220x300	2	20	140x300	S355	C1
3	R_S235_S355_C2	R	50	S235	30	220x300	2	20	140x300	S355	C2
4	R_S235_S355_C3	R	50	S235	30	220x300	2	20	140x300	S355	C3
5	R_S235_HSS_E	R	50	S235	30	220x300	2	20	140x300	HSS	E
6	R_S235_HSS_C1	R	50	S235	30	220x300	2	20	140x300	HSS	C1
7	R_S235_HSS_C2	R	50	S235	30	220x300	2	20	140x300	HSS	C2
8	R_S235_HSS_C3	R	50	S235	30	220x300	2	20	140x300	HSS	C3
9	R_SiS_S355_E	R	50	SiS	30	220x300	2	20	140x300	S355	E
10	R_SiS_S355_C1	R	50	SiS	30	220x300	2	20	140x300	S355	C1
11	R_SiS_S355_C2	R	50	SiS	30	220x300	2	20	140x300	S355	C2
12	R_SiS_HSS_E	R	50	SiS	30	220x300	2	20	140x300	HSS	E
13	R_SiS_HSS_C1	R	50	SiS	30	220x300	2	20	140x300	HSS	C1
14	R_SiS_HSS_C2	R	50	SiS	30	220x300	2	20	140x300	HSS	C2
15	C_S235_S355_E	C	50	S235	30	220x300	2	20	140x300	S355	E
16	C_S235_S355_C1	C	50	S235	30	220x300	2	20	140x300	S355	C1
17	C_S235_S355_C2	C	50	S235	30	220x300	2	20	140x300	S355	C2
18	C_S235_S355_C3	C	50	S235	30	220x300	2	20	140x300	S355	C3
19	C_S235_HSS_E	C	50	S235	30	220x300	2	20	140x300	HSS	E
20	C_S235_HSS_C1	C	50	S235	30	220x300	2	20	140x300	HSS	C1
21	C_S235_HSS_C2	C	50	S235	30	220x300	2	20	140x300	HSS	C2
22	C_S235_HSS_C3	C	50	S235	30	220x300	2	20	140x300	HSS	C3
23	C_SiS_S355_E	C	50	SiS	30	220x300	2	20	140x300	S355	E
24	C_SiS_S355_C1	C	50	SiS	30	220x300	2	20	140x300	S355	C1
25	C_SiS_S355_C2	C	50	SiS	30	220x300	2	20	140x300	S355	C2
26	C_SiS_HSS_E	C	50	SiS	30	220x300	2	20	140x300	HSS	E
27	C_SiS_HSS_C1	C	50	SiS	30	220x300	2	20	140x300	HSS	C1
28	C_SiS_HSS_C2	C	50	SiS	30	220x300	2	20	140x300	HSS	C2

Dimensions in mm and steel grades in MPa

(*) Configuration code according to: #PinShape_#PinSteelGrade_#PlatesSteelGrade_#LoadProtocol

Color codes		
Protocol	Pin section	Steel grade
E = ECCS	R = Chamfered	S235
C1 = Constant 1	C = Circular	SiS
C2 = Constant 2		S355
C3 = Constant 3		HSS

Fig. 2.16: Full list of experimental test specimens (RFCS Project - Dissipable, 2017).

To have a more symmetrical behaviour, some plates, called guide plates, were installed. Initially, 2 plates were placed that are welded to the spacer outside, which significantly reduces the lateral clearance (GP1). The problem was not completely solved and to improve it, two more plates were installed on the inside of the box (GP2) (fig. 2.17). The application of these plates reduced 500%(!) the lateral displacement and thus allow the efficient channelling of the movement of the device (Cabrita, 2020).

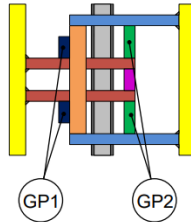


Fig. 2.17: Guiding plates

Besides this problem there was still another one to solve in the pins with circular section. Due to its geometry, there is a lower degree of recessions and thus for the pin not to have significant lateral movements we tested 4 ways of welding it (fig. 2.18).

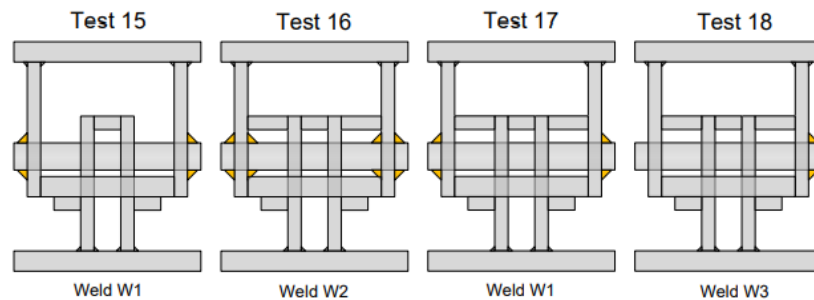


Fig. 2.18: Tested weld configurations (Cabrita, 2020).

The INERD studies show a pinching phenomenon (Vayas et al., 2017), due to rolling at the interface of the plates and pins, this is all since slippage caused by the hole ovalizations occurs.

The pins with chamfered section present a failure mode by bending in the middle section of the pin, which is assumed, while the other pins their rupture happens in a shear mode curiously where they are welded (until the weld breaks), which prevents greater freedom pin and thus a plastic hinge occurs. At this event it becomes more difficult to replace the pin, which is not intended. Test 18C was welded on one side and the elongation of the free side was noticeable.

It can be concluded that the use of welding is not favourable for the performance of the device, not only by premature failure but also prevents the elongation of the pin, compromising ductility. Consequently, the use of circular pins is not recommended. Pin elongation plays a key role in the failure mode and cyclic behaviour of specimens (Cabrita, 2020).

The figure 2.19 shows a scattering of values in case the pin section is circular, which shows unpredictable behaviour. The values are smaller than for pins with chamfered section.

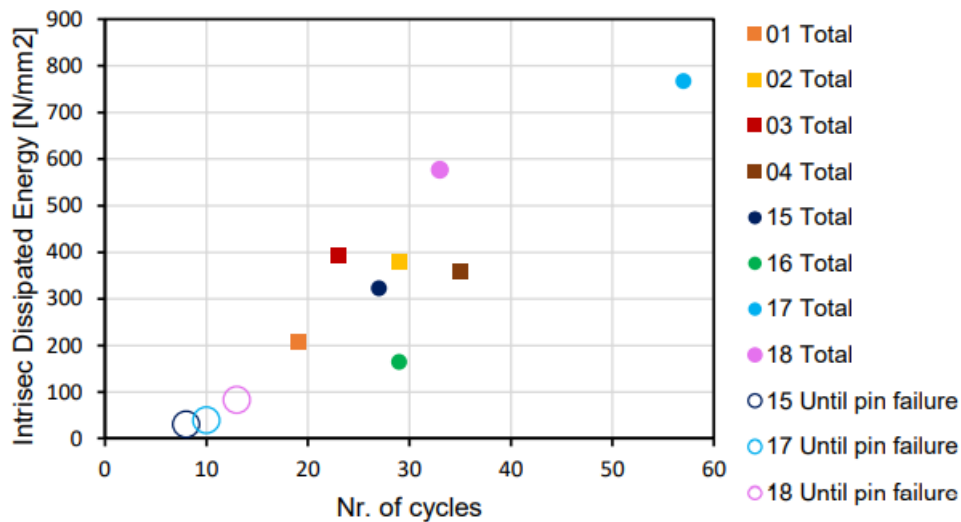


Fig. 2.19: Intrinsic Dissipated Energy (Cabrita, 2020).

The total intrinsic dissipated energy is used to have uniform values and is determined by the action between the total dissipated (area) and the intrinsic volume, which is the volume of the pin relative to the length between the central axis of the outer plates.

2.3.3 Numerical analysis

To have a comparison term at the theoretical level, DRBrC devices were created using the ABAQUS software, which simulates the tests. The device is built with its geometric configurations and the boundary conditions are defined, and finally an input of the load history is made from Excel. To better understand how a numerical model is developed the following scheme simplifies it (fig. 2.20).

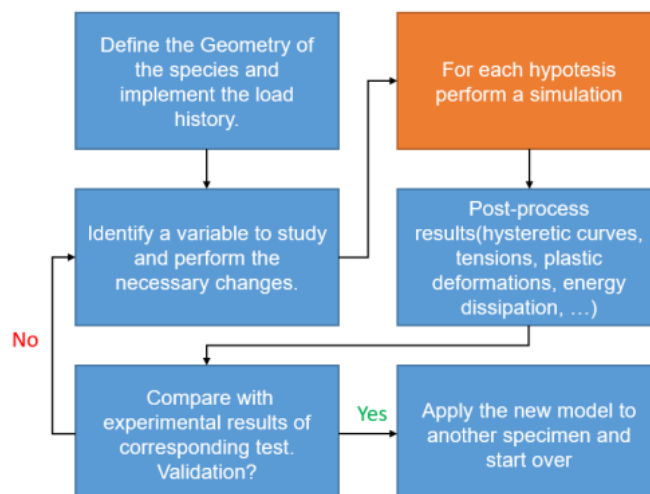


Fig. 2.20: Scheme of the general methodology used (Farinha, 2020).

To run this scheme, you need to solve 3 core topics to develop the numerical model:

-Finite Element Method.

-Material modelling.

-Contact modelling.

2.3.3.1 Finite Element Method

It is a numerical technique that calculates an approximate solution for partial differential equations.

In this simulation a quasi-static resolution was used because as the large displacements and velocity are small, inertial forces and impacts can be neglected. Being a dissipative device with plastic deformation capacity, it has a physical nonlinear behaviour, i.e., it is not enough just to define it by Hooke's law. It is also necessary to consider the 2nd order effects to capture the plasticity and failure's pin, that it's important for dissipative devices.

In ABAQUS, a mesh of 8-noded elements was chosen. Although not very precise, the model had enough elements to avoid discrepancy of values, with a 15mm edge for elements which are not expected to have plastic deformations. To have more accurate results, the mesh was refined in the interaction zone between the plates and the pin, where the elements subjected to plastic deformations have a 5mm edge (fig. 2.21). This figure also illustrates the boundary conditions, where the device is fixed (blue arrows) and where there is displacement increment (yellow arrows).

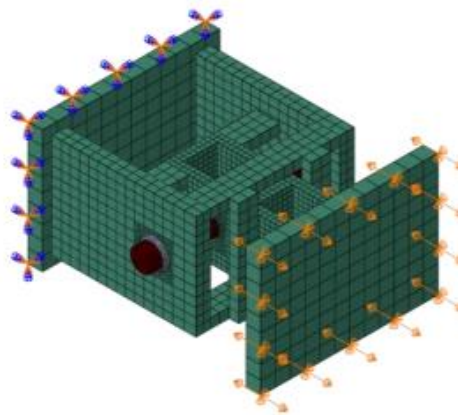


Fig. 2.21: Mesh of a generic example that achieved accurate results.

A finer mesh with the iterative implicit method was used. This method solves the equation in each increment to achieve equilibrium, making the simulation stable.

2.3.3.2 Material modelling

For this type of device, it is necessary to define a plastic ratio capable of dissipating considerable amounts of energy. Thus, it must include a law for the plastic domain. To complete a test, a

damage must be implemented so that the effects of total failure and material degradation can be captured in the numerical criterion (Farinha, 2020).

Before exploring the material, common and residual values were defined such as Poisson's ratio, which for steels takes the requirement of 0.3, and Young's modulus, which by prior knowledge is on the order of 210GPa.

To define the plastic evaluation there are 4 unknowns:

- C_1 Initial Hardening Parameter.
- γ_1 Kinematic Hardening Parameter.
- Q_∞ Isotropic hardening Parameter.
- b Isotropic hardening Parameter.

After the tensile tests carried out at LERM, the isotropic part of the hardening has been neglected without a significant loss of accuracy, so there remain two variables (C_1, γ_1), which are arbitrated in an Excel sheet to calibrate with the straight line originated from the tensile tests, namely with the true stress-strain curve.

These arbitrated values are smaller than the theoretical ones since the implemented plastic curve can only have a logarithmic evolution.

2.3.3.3 Contact modelling

Good literatures on this subject on which this problem was based are (Barber & Ciavarella, 2000) and (Adams & Nosonovsky, 2000), considering the topography and tribology of the contact surfaces.

If there is no modelling of the contact surfaces throughout the tests, the objects tend to penetrate with each other without any reaction/interaction. This is not realistic and thus the outer limits of each part had to be defined. The main option to use the contact formulation is to discretize the contact surfaces into a series of nodes, with the most common formula is master slave (fig. 2.22).

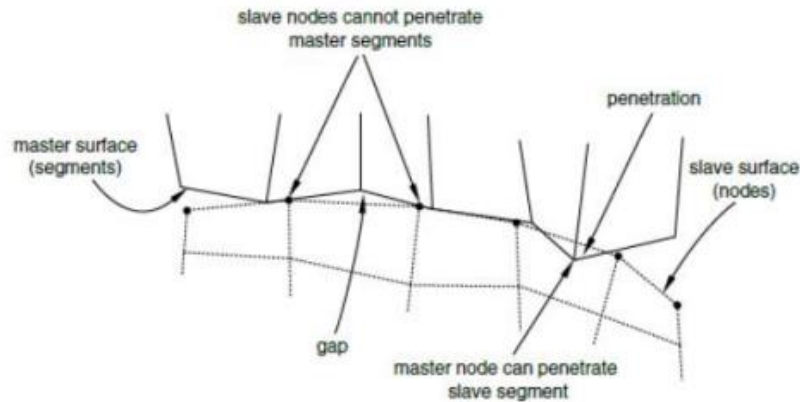


Fig. 2.22 Node to surface contact specifications (DASSAULT, 2014).

ABAQUS applies the following rules related to the assignment of the master-slave role for contact surfaces (ABAQUS, 2012):

- Analytical rigid surfaces and rigid-element-based surfaces must always be the master surface.
- A node-based surface can act only as a slave surface and always uses node-to-surface contact.
- Slave surfaces must always be attached to deformable bodies or deformable bodies defined as rigid.
- Both surfaces in a contact pair cannot be rigid surfaces except for deformable surfaces defined as rigid.

Generally, if a smaller surface contacts a larger surface, it is better to choose the smaller surface as the slave surface. If this distinction cannot be made, the master surface should be chosen as the surface of the stiffest or as the surface with the thickest mesh, if the two surfaces are on structures with comparable stiffness.

The choice of master and slave roles typically has much less effect on the results with a surface-to-surface contact formulation than with a node-to-surface contact formulation. In both formulations, during the test the normal direction of each surface experiences discontinuities, which can lead to instability in the pressure distribution (Farinha, 2020).

By software default, in ABAQUS there is always some penetration, even in the hard contact formulation, for reasons of numerical stability.

With all this, the type of contact used was surface-to-surface, which is standard in ABAQUS. This individually defines the interactions between each pair of elements, and its advantage over the others is that it is more stable than the surface-to-surface node formulation.

The slip formulation used was a finite slip which, although heavier, was necessary because the small slip could not achieve accurate results due to the large relative displacement between the plates and the pin. Using this formulation, the pin would not be able to deform as per the laboratory tests because the tangential motion would be restricted. To overcome this a formulation called Penalty was applied that allows the implementation of isotropic friction at the contacts, following Coulomb's law (DASSAULT, 2014):

$$f_s = \mu \times \rho \quad (2.1)$$

2.3.3.4 Results

- Pinching phenomena were not captured.
- The experimental tests have lateral displacement in which in ABAQUS is null (as expected).
- Regarding the forces, the values are very similar with those obtained in the laboratory, both for chamfered pin and circular pin.
- The test selected to analyse the circular pin tests was 16 and showed the greatest divergence because it had 4 welds (fig. 2.23). The welds were degraded over the course of the experimental test, ABAQUS it takes no recognition of this effect.

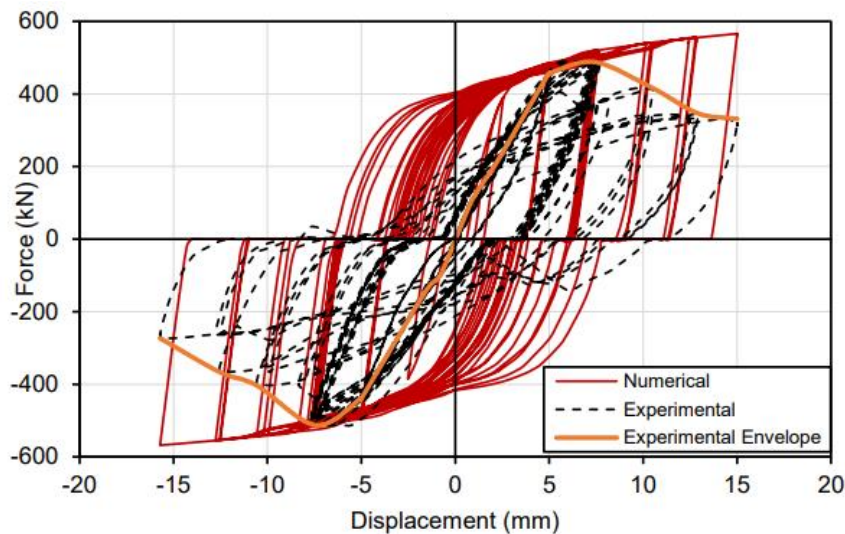


Fig. 2.23: Force-displacement curves comparison for test 16 (Cabrita, 2020).

- The test selected to analyse the bevelled pin tests was 2 and the results were quite positive within the context (fig. 2.24).

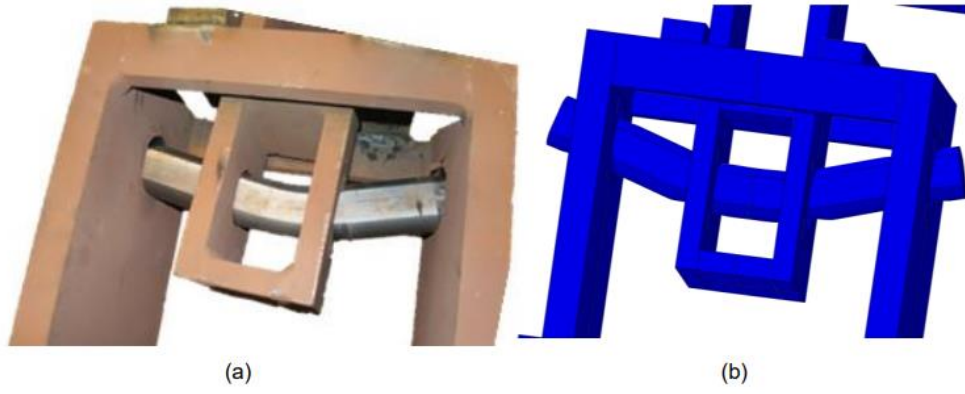


Fig. 2.24: Deformation of the pin in test 02: (a) experimental test, (b) numerical model (Cabrita, 2020).

3. Experimental Studies

3.1 Introduction

The experimental studies presented are part of the DISSIPABLE project schedule (RFCS-02-2017, 2017). These studies establish the second phase of experimental tests on the behaviour of the DRBrC (Dissipative Replaceable Bracing Connection) device, initially composed of six different pin device configurations presented in Figure 3.1.

The main objective is to analyse design issues and evaluate the influence of different parameters, namely material properties, pin material (S235 or StS) and plates (S355 or HSS), and geometric properties, specifically the inner plate spacing (D1 or D2), on the overall behaviour of the pin device in terms of power dissipation and failure modes.

Full list of experimental test specimens

No of test configuration	Configuration code (*)	Pin shape	Pin Φ	Pin steel	External plate thickness	External plate dimensions	Internal Plate spacing	Internal plate thickness	External plate dimensions	Plates steel	Load protocol
1	R_S235_S355_D1_E	R	50	S235	30	220x300	D1	20	140x300	S355	E
2	R_S235_S355_D1_C1	R	50	S235	30	220x300	D1	20	140x300	S355	C1
3	R_S235_S355_D1_C2	R	50	S235	30	220x300	D1	20	140x300	S355	C2
4	R_S235_S355_D1_C3	R	50	S235	30	220x300	D1	20	140x300	S355	C3
5	R_S235_HSS_D1_E	R	45	S235	30	220x300	D1	20	140x300	HSS	E
6	R_S235_HSS_D1_C1	R	45	S235	30	220x300	D1	20	140x300	HSS	C1
7	R_S235_HSS_D1_C2	R	45	S235	30	220x300	D1	20	140x300	HSS	C2
8	R_S235_HSS_D1_C3	R	45	S235	30	220x300	D1	20	140x300	HSS	C3
9	R_S35_S355_D1_E	R	45	S35	30	220x300	D1	20	140x300	S355	E
10	R_S35_S355_D1_C1	R	45	S35	30	220x300	D1	20	140x300	S355	C1
11	R_S35_S355_D1_C2	R	45	S35	30	220x300	D1	20	140x300	S355	C2
12	R_S35_HSS_D1_E	R	45	S35	30	220x300	D1	20	140x300	HSS	E
13	R_S35_HSS_D1_C1	R	45	S35	30	220x300	D1	20	140x300	HSS	C1
14	R_S35_HSS_D1_C2	R	45	S35	30	220x300	D1	20	140x300	HSS	C2
15	D_S235_S355_D1_E	R	50	S235	30	220x300	D1	20	140x300	S355	E
16	D_S235_S355_D1_C1	R	50	S235	30	220x300	D1	20	140x300	S355	C1
17	D_S235_S355_D1_C2	R	50	S235	30	220x300	D1	20	140x300	S355	C2
18	D_S235_S355_D1_C3	R	50	S235	30	220x300	D1	20	140x300	S355	C3
19	R_S235_HSS_D2_E	R	45	S235	30	220x300	D2	20	140x300	HSS	E
20	R_S235_HSS_D2_C1	R	45	S235	30	220x300	D2	20	140x300	HSS	C1
21	R_S235_HSS_D2_C2	R	45	S235	30	220x300	D2	20	140x300	HSS	C2
22	R_S235_HSS_D2_C3	R	45	S235	30	220x300	D2	20	140x300	HSS	C3
23	R_S35_S355_D2_E	R	45	S35	30	220x300	D2	20	140x300	S355	E
24	R_S35_S355_D2_C1	R	45	S35	30	220x300	D2	20	140x300	S355	C1
25	R_S35_S355_D2_C2	R	45	S35	30	220x300	D2	20	140x300	S355	C2
26	R_S35_HSS_D2_E	R	45	S35	30	220x300	D2	20	140x300	HSS	E
27	R_S35_HSS_D2_C1	R	45	S35	30	220x300	D2	20	140x300	HSS	C1
28	R_S35_HSS_D2_C2	R	45	S35	30	220x300	D2	20	140x300	HSS	C2

Dimensions in mm and steel grades in MPa
 (*) Configuration code according to: #PinShape_#PinSteelGrade_#PlatesSteelGrade_#InternalPlateSpacing_#LoadProtocol

Color codes			
Protocol	Pin section	Steel grade	Internal plate spacing
E = ECOS	R = Chamfered	S235	D1 = 80/70/60
C1 = Constant 1	S = Circular	S35	D2 = 70/60/70
C2 = Constant 2		S355	
C3 = Constant 3		HSS	

Fig. 3.1: Initial full list of experimental test specimens.

During the experimental tests, additional four tests were performed using recovered DRBrC device boxes (plates), tested on the current (second) phase of experimental tests, and the leftover pin material from the first phase of experimental tests (S235*) on the local behaviour of the DRBrC device (DISSIPABLE, 2020a).

Table 3.1 shows the list of the test configurations of the second phase of the experimental studies tested, on March 2021, including the additional four tests in red. In this table only the differentiating

parameters of each configuration are shown, which are the pin material, the plates material, the interior plates spacing, and the load history applied.

Tab. 3.1: Final list of tested configurations on the second phase.

Test No	Configuration Code	Pin Material	Plates Material	Plates Spacing	Load History
05	R_S235_HSS_D1_E	S235	HSS	80/70/80	ECCS
06	R_S235_HSS_D1_C1	S235	HSS	80/70/80	Constant 20 mm
07	R_S235_HSS_D1_C2	S235	HSS	80/70/80	Constant 30 mm
08	R_S235_HSS_D1_C3	S235	HSS	80/70/80	Constant 25 mm
09	R_StS_S355_D1_E	StS	S355	80/70/80	ECCS
10	R_StS_S355_D1_C1	StS	S355	80/70/80	Constant 30 mm
11	R_StS_S355_D1_C2	StS	S355	80/70/80	Constant 25 mm
11R	R_StS_S355_D1_E	S235*	S355	80/70/80	ECCS
12	R_StS_HSS_D1_E	StS	HSS	80/70/80	ECCS
13	R_StS_HSS_D1_C1	StS	HSS	80/70/80	Constant 30 mm
13R	R_StS_HSS_D1_E	S235*	HSS	80/70/80	ECCS
14	R_StS_HSS_D1_C2	StS	HSS	80/70/80	Constant 25 mm
19	R_S235_HSS_D2_E	S235	HSS	70/90/70	ECCS
20	R_S235_HSS_D2_C1	S235	HSS	70/90/70	Constant 20 mm
20R	R_S235_HSS_D2_E	S235*	HSS	70/90/70	ECCS
21	R_S235_HSS_D2_C2	S235	HSS	70/90/70	Constant 30 mm
22	R_S235_HSS_D2_C3	S235	HSS	70/90/70	Constant 25 mm
23	R_StS_S355_D2_E	StS	S355	70/90/70	ECCS
24	R_StS_S355_D2_C1	StS	S355	70/90/70	Constant 30 mm
25	R_StS_S355_D2_C2	StS	S355	70/90/70	Constant 25 mm
25R	R_StS_S355_D2_E	S235*	S355	70/90/70	ECCS
26	R_StS_HSS_D2_E	StS	HSS	70/90/70	ECCS
27	R_StS_HSS_D2_C1	StS	HSS	70/90/70	Constant 30 mm
28	R_StS_HSS_D2_C2	StS	HSS	70/90/70	Constant 25 mm

3.2 Drawings

As mentioned in section 2.3.2 (figure 2.12) in this second phase there was this evolution to improve the performance of the DRBrC. Thus, are present in the following figures the configurations of the boxes for both the inner plate spacing D1, figure 3.2, and for D2, figure 3.3.

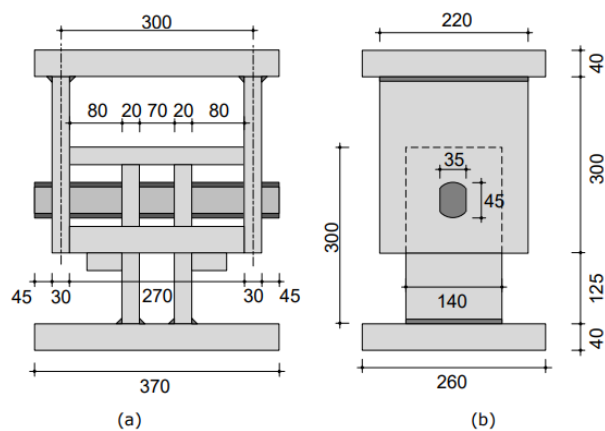


Fig. 3.2: Dimensions (mm) of DRBrC with spacing D1 (=70mm): (a) Top view, (b) Lateral view (DISSIPABLE, 2021).

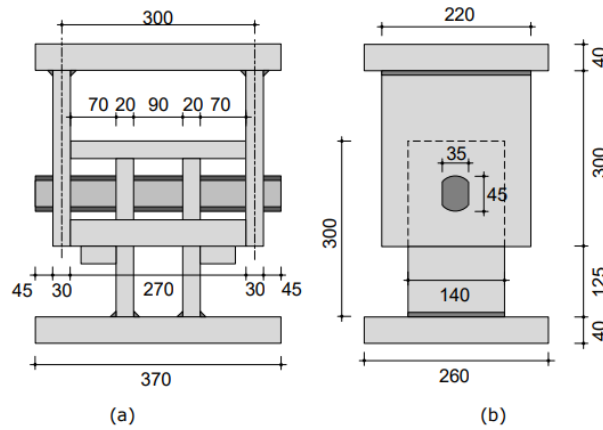


Fig. 3.3: Dimensions (mm) of DRBrC with spacing D2 (=90mm): (a) Top view, (b) Lateral view (DISSIPABLE, 2021).

3.3 Load Histories

Similarly, to the first phase of experimental tests on the dissipative device, the load histories applied differ in whether it is a constant cyclic test, of 20, 25 and 30 mm amplitudes, or a hysteretic cyclic test based on the ECCS (European Convention for Constructional Steelwork) protocol (ECCS, 1986), as seen in Table 3.2. The ECCS hysteretic cyclic load history is applied to standardize and better analyse the results. This protocol provides tools for easily comparing between experimental tests. The protocol is composed by a sequence of cycles presented in (Cabrita, 2020). The elastic displacement determined for the present experimental tests is $\delta_y=2.5\text{mm}$. This value was determined using the design guides developed for the device (DISSIPABLE, 2020b).

Tab. 3.2: ECCS load history (ECCS, 1986).

Step	Imposed displacement interval	Number of Cycles
1	$+\frac{1}{4}\delta_y, -\frac{1}{4}\delta_y$	1
2	$+\frac{1}{2}\delta_y, -\frac{1}{2}\delta_y$	1
3	$+\frac{3}{4}\delta_y, -\frac{3}{4}\delta_y$	1
4	$+\delta_y, -\delta_y$	1
5	$+2\delta_y, -2\delta_y$	3
>5	$+(2 + 2n)\delta_y, -(2 + 2n)\delta_y, n = 1, 2, \dots$	3

3.4 Experimental Setup

Experimental tests took place in Laboratório de Estruturas e Resistência dos Materiais (LERM), in figure 3.4, hosted in Departamento de Engenharia Civil, Arquitetura e Georrecursos (DECivil)

of Instituto Superior Técnico (IST), from Universidade de Lisboa (UL). The facilities are considered appropriate for the intended experimental study, since:

- It has the necessary facilities, equipment and knowledge to perform the tests.
- The previous design of the pin (Calado et al., 2004) and the first phase of experimental tests on the pin current design (DISSIPABLE, 2018) were successfully tested in LERM.
- The team leading the project is very experienced not only on experimental tests, but also in energy dissipation and seismic engineering.
- Also, the researchers involved in the project have the engineering skills required to actively meet the project needs.



Fig. 3.4: Overall view of LERM.

“The experimental test process consists of imposing uniaxial displacements, through a mechanical actuator, on a brace equipped with the dissipative device. These displacements are controlled manually through the control console and can be either in forward or backward directions, corresponding to compression or tension, respectively. An installed load cell then measures the force that the pin device is subjected.” (Cabrita, 2020).

The general idea of the loading system is to react against a rigid concrete wall (reaction wall) existing in the LERM. This concept preforms ideally for monotonic unidirectional tests. But, since the tests of the hysteretic pin device are cyclic, another rigid end is needed. Thus, another “rigid” end is built using existing steel elements to erect a rigid frame. The main concept of the test setup is represented in Figure 3.5.

Based on the setup illustration, an identification of key elements composing the setup and its description is summarized next. DRBrC is identified and rigid coupling elements fabricated are represented in purple.

In Figure 3.6 and Figure 3.7, overall perspectives of the experimental setup are shown, with the identification the DRBrC specimen positioning and other relevant elements.

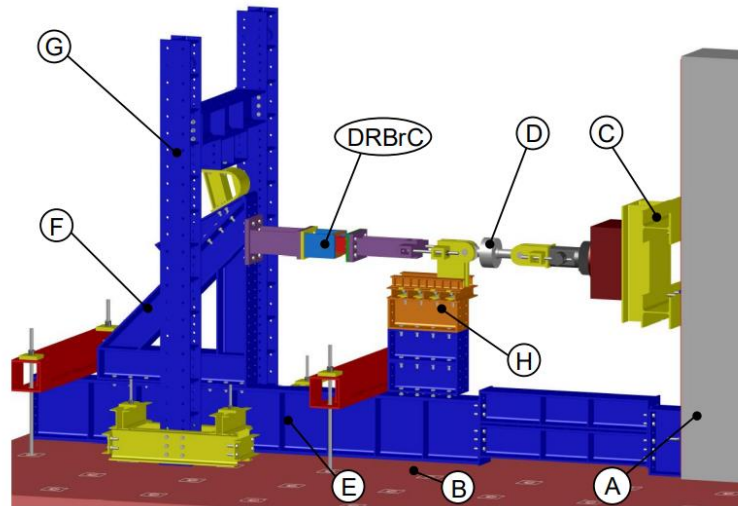


Fig. 3.5: General overview of experimental setup (DISSIPABLE, 2021).

(A) Reaction wall: a rigid reinforced concrete wall where several elements can be attached by means of pre tensioned Dywidag bars. Is expected to behave like a rigid support.

(B) Reaction floor: the main floor is a very stiff reinforced concrete slab. To attach elements to it, distributed holes in a 1.00x1.00 m² mesh were considered in its design, to connect and restrain elements using Dywidag bars. In the test setup region, the floor has thickness of 1.00 m. Is also expected to work as rigid support to other elements.

(C) Actuator: One electric worm-screw actuator with 1000kN load capacity in both tension and compression, that shall unload against a rigid element. Its displacement range is 400 mm;

(D) Load cell: This element is a force transducer. It converts the force into an electric signal that can be measured and standardized through a software. As described in DRBrC specimens' restrictions, this element reads force values in the range of -500 to 500kN. It is connected to hinged steel eyelets, which are linked to the structures via threaded bars $\Phi 30$ cl 12.9.

(E) Base: The base is made by coupling several elements. One 4500mm long HEB600 element one the left-hand side, two 1700mm HEB300 steel beams on the middle and finally a coupling device on the right-hand side to connect steel elements to reaction wall hole design. The base is fixed to the rigid floor by means of Dywidag bars, preventing its rotation.

(F) Rigid triangular frame: Triangular frame composed by welded HEB300 elements, which is expected to support the load received by the specimen in test. This element is bolted to the base elements and its tip is connected to a frame using coupling elements.

(G)Frame: A steel frame composed by two HEB300 columns, a HEB300 beam and transition elements that restrains the possible displacements of the rigid triangle frame. These elements are all connected through bolts. Plus, the frame structure is founded to the rigid floor using UNP transition elements and Dywidag bars, distributed in the load direction to increase the stiffness of the column's bases.

(H)Railway base: A base to support the rolling tip of the actuator, preventing unnecessary stresses on the actuator. This base is made using three 700mm long HEB300 elements. On top of these elements, a small railway is fixed, manufactured using two 720mm long HEB100 Also, this rail ensures that the introduced force on the testing device is uniaxial, avoiding second order effects.

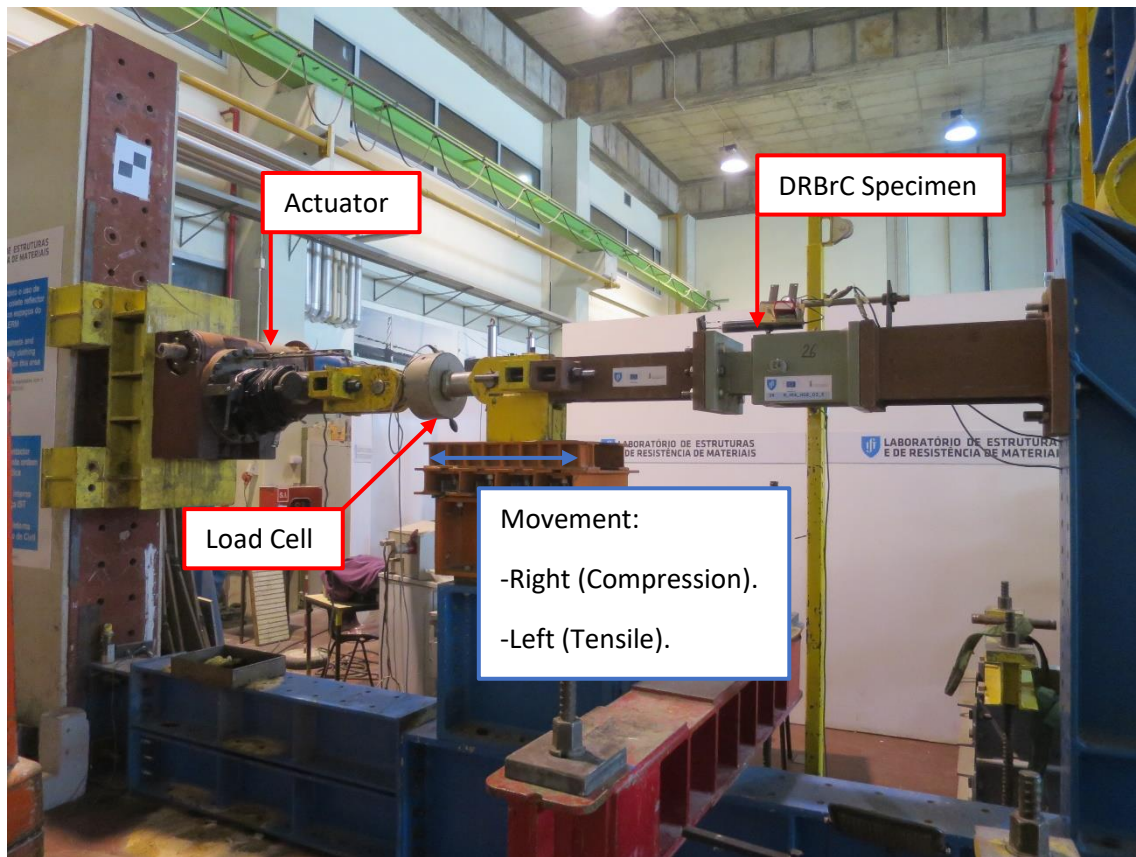


Fig. 3.6: View from north of the experimental setup.

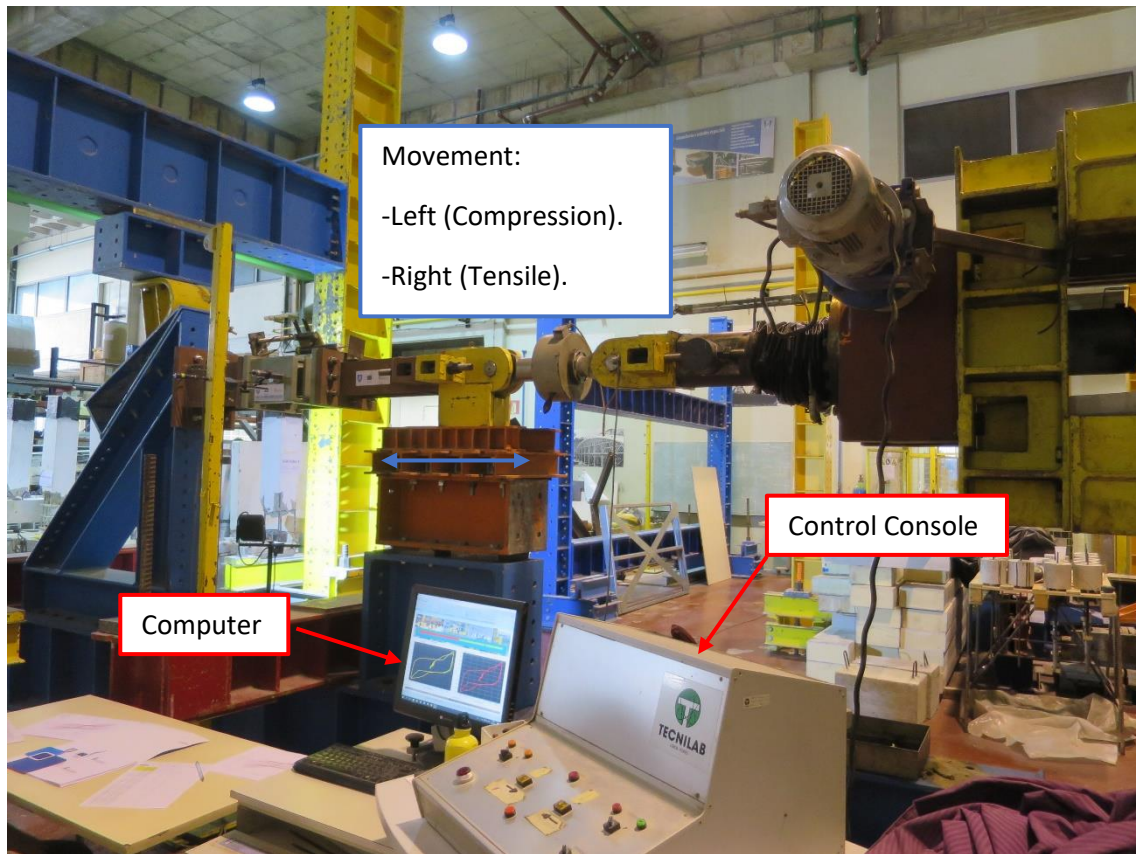


Fig. 3.7: View from south of the experimental setup.

Together with the live visualization of the experimental tests, data acquisition is fundamental for postprocessing and understating the dissipative device behaviour in study. To get this information, measuring instruments shall be considered in the experimental setup.

In Table 3.3, the main quantities expected to be measured (determined), its physical dimension, the sensors used for that purpose, and their location is defined.

Tab. 3.3: Principal quantities to be measured.

Quantity	Dimension	Measure instrument
Length (L)	Millimeter (mm)	Displacement transducer
Force (F)	Kilonewton (kN)	Load cell
Time (t)	Second (s)	Computer software

The full list of instruments used are presented in Table 3.4, together with their codenames, sensibility, scale and organized by the channel to which they are connected to the data logger. Figure 3.8 and Figure 3.9 show the location of all selected instruments. Also, the signal orientation concept of the sensors is shown.

LVDT1 and the wire transducer evaluates the principal displacement in the load direction of the device. The wire transducer presents less accuracy than the LVDT1, but it is needed to measure displacements greater than 50mm (in one direction), also serving as a backup in case LVDT1 fails for some reason. The remaining displacement transducers, LVDT2, are selected to control

the possible lateral displacements of the device box. The load cell evaluates the exerted force in the specimen when applying the imposed displacements.

Table 3.4: Measuring instruments configurations.

Channel	Instrument	Name	Codename	Sensibility	Scale	Location
4-0	LVDT1	CDP-100	561656	5mV/V	100	Device (above)
4-1	Load Cell	HBM 500	F846	2mV/V	500	Between device actuator
4-2	LVDT2	CDP-50	511662	5mV/V	50	Device lateral tip (South)
4-3	Wire Transducer	DP-500 E	BGD130526	5mV/V	500	Device (above)

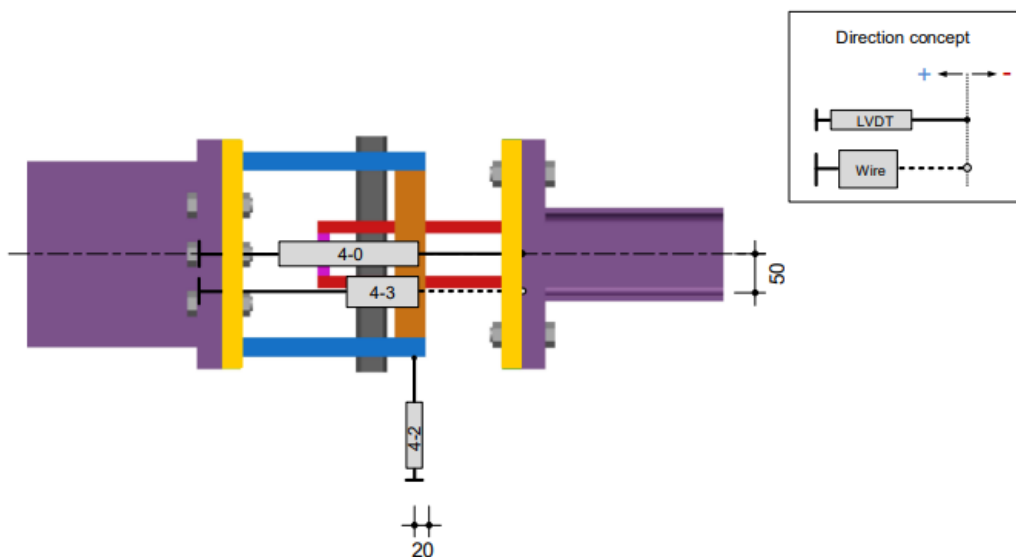


Fig. 3.8: Position of the displacement transducers and direction criterion. View from above (Dimensions in mm) (DISSIPABLE, 2021).

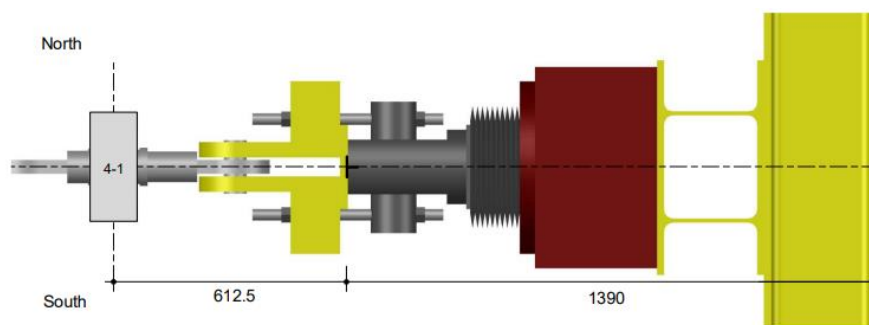


Fig. 3.9: Location of the load cell. View from above (Dimensions in mm) (DISSIPABLE, 2021).

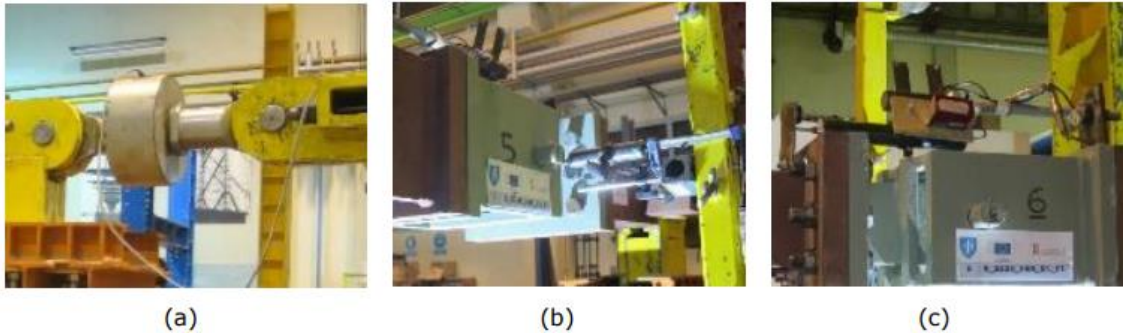


Fig. 3.10: Examples of instruments selected for tests: (a) Load cell, (b) lateral displacement transducer and (c) principal displacement transducer and wire transducer (DISSIPABLE, 2021).

The electric signal generated by the instruments is transmitted to a computational interface via cable, which completes the connection between the sensor and a data logger, finalizing the measuring system.

Cable connection between data logger and computer, conduces the signal to a normalized and calibrated software, that is used to correlate the simultaneous and permanent electrical signals measured, with the physical quantities intended to read in the first place (Figure 3.11 (a)). Despite the electric signal being continuous, multichannel data logger chosen has 2 seconds (0.5 Hz) discrete acquisition rate. The software (Figure 3.10 (b)) is capable to program the displacement control of the actuator, but manual control is preferential due to the uncertainty of the automatic (Figure 3.10 (c)). A computer display is used to visualize live measurements. Data recording is completed and stored using the computer's hard disc drive.

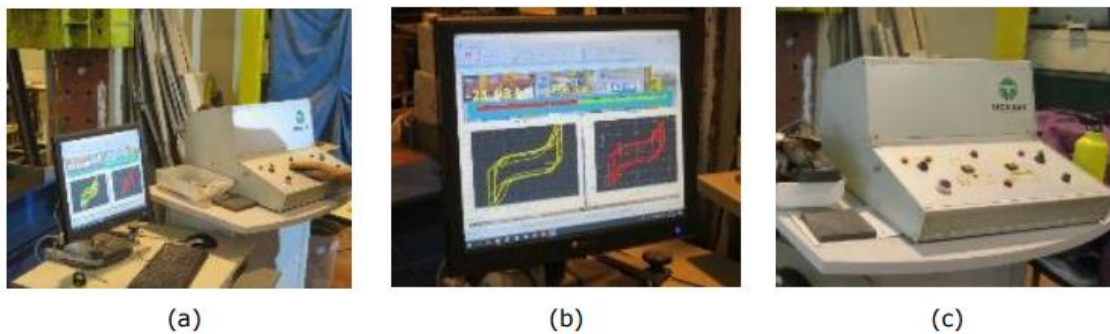


Fig. 3.11: Examples of equipment used: (a) Computer setup, (b) software and (c) actuator manual control (DISSIPABLE, 2021).

All tests are permanently recorded to a video format using video camera strategically located to obtain a bottom view of the test. The resulting camera view is presented in Figure 3.12. The video camera positioning observed in the first phase of experimental tests was changed from the top of the device to the bottom. In the second phase of the experimental tests the principal displacement transducers are placed in the top, allowing to install the video camera in the bottom, with a free view of the device and an unimpeded access to the video camera.



Fig. 3.12: Video camera view (DISSIPABLE, 2021).

3.4.1 Procedures before the first test

Like the first phase of experimental tests, an exhaustive review of the chosen cables, acquisition equipment and sensors is performed to assess their correct functionality, accuracy, and precision. This process was done with a set of repetitive tests on the sensors. A signal concept shall be logically decided, so every measurement can be criticized during the test. Every sensor was mounted in the respective position according to Table 3.4, Figure 3.8, and Figure 3.9. Next, instructions from “Procedures before test” were applicable.

3.4.2 Procedures before a test

In this step, all measured quantities in each channel are set to zero. Also, an overall inspection of the elements and connections must be performed.

If no issues arise, before each test initiates, a pre-test run is recommended. The objective of pre-test procedure is to evaluate every measuring instrument in what concerns its functionality, signal, scale, precision, accuracy, and reproducibility of a measurement. This practice is repeated until satisfactory results are obtained. This examination is made using a known quantity, like a distance measure (e.g., a 50 cent's coin with thickness=2.80 mm), repeatedly on each sensor.

Signal and scale are assessed by critically analysing a measurement value. Accuracy is attained if several measures are in accordance with the agreed “real” value (the coin thickness). Reproducibility is a sign of the consistency of measurements made under certain different conditions (like time, location of the instrument, observer, method, etc.), while precision evaluates the influence of random factors in several different result outputs of a certain quantity. Its workability is simply evaluated recurring to status quo state, where a “random” event (flicker, which relies on different velocity of the electric current in the cables due to semiconductors

materials imperfections), higher than the discrimination threshold, “activates” the measuring instruments, resulting in a readable measure in the control software. For example, when not loaded, the load cell reading is fluctuating between values $[-0.037, +0.026]$ kN, with 3 significant digits. This measurement needs to be enough representative to resolution of the sensors.

If pre-test comes out acceptable, the test system reproducibility and its measurements is ensured. Thus, recording devices are started, measuring instruments set to zero and the test is ready to begin. As introduced, the tests take around 2 to 4 hours, depending on the specimen tested.

3.4.3 Procedures during a test

Main procedures to be taken during a test are the control of a set of parameters like force and actuator displacement. The tests are always performed with two persons controlling it. One controlling the actuator displacement at the control table while other should check the begin of each half cycle on a spreadsheet. The two must be able to evaluate and control the parameters live on the computer screen. Every pause (for photographs, etc.) or occurrence (system malfunction, not expected noises, etc.) were registered and, if needed, pictured/recorded.



Fig. 3.13: Computer and Control Table control of parameters during a test.

3.4.4 Procedures after a test

After completing an experimental test, all acquired information is backup to external devices (pen drive). Video recording equipment is safely dismantled and stored. Plus, every electrical device is disconnected from its energy source. Lastly, every displacement transducer is disconnected and dismantled, to avoid further precision problems and its lifetime span. After been done these procedures that ensure workability for the laboratory technicians, disconnection of the load cell and tested device removal, followed by its replacement with a new device is conceivable.

3.5 Material Characterization (Steel's)

Material characterization data was received from the steel manufacture SOFMAN. The material main characteristics determined by SOFMAN for each material are shown in Table 3.5.

Tab. 3.5: Material main characteristics determined by SOFMAN.

Material	Component	f_y (MPa)	f_u (MPa)	Elongation (%)
S235	Pin	238	344	37
StS	Pin	348	646	50
S355	Plates	387	489	25.5
HSS	Plates	442	533	26
S235*	Pin	235	360	40

Note (*) – material from the first phase of experimental tests.

Nonetheless, to draw the complete stress-strain curves for each material, tensile tests on the material of the specimens received were performed. Allowing for a more accurate definition of the numerical models that are being developed in this investigation.

The tensile tests were performed using Instron machine with 250 kN capacity and 100 mm scale range available in LERM (Figure 3.14).



Fig. 3.14: Instron test machine (DISSIPABLE, 2021).

Tensile test specimens were produced using the material removed from tested DRBrC specimen. The pin material S235 was removed from the pin of test 06. The pin material StS was removed from the pin of test 12. The plate material HSS was removed from the exterior plate of test 06 specimen (Figure 3.15). The plate material S355 was removed from the exterior plate of test 09 specimen.

Tensile test specimens of S355, HSS, StS and S235 materials are presented in Figure 3.16.

The pin material S235*(1) and S235*(2) was removed from the pin of an untested device of the first phase (DISSIPABLE, 2020) of experimental tests (Figure 3.17).



Fig. 3.15: Test 06 DRBrC specimen material (DISSIPABLE, 2021).



Fig. 3.16: Tensile test specimens of S355, HSS, StS and S235 materials, respectively (DISSIPABLE, 2021).



(a)



(b)

Fig. 3.17: Tensile test specimen S235*(1) – (a) removed pin and (b) pin processing (DISSIPABLE, 2020).

The dimensions of the tensile test specimens used, respectively for S235, StS, S355, HSS, S235*(1) and S235*(2) materials, are presented from Figure 3.18 to Figure 3.23.

Table 3.6 shows the summary of the tensile test specimen dimensions, regarding the free initial length, the width and thickness (in the case of the rectangular specimens) and diameter (in the case of the circular specimens).

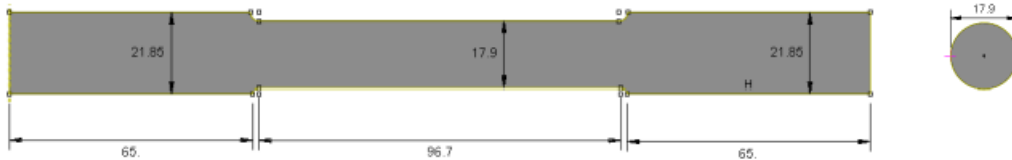


Fig. 3.18: Dimensions of S235 material tensile test specimen (DISSIPABLE, 2021).

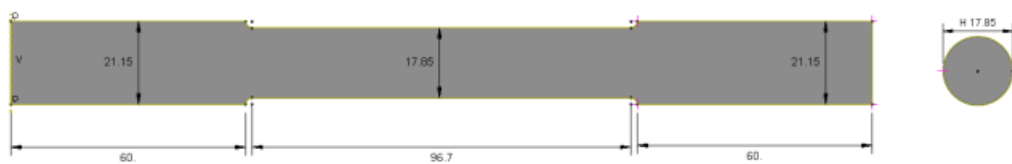


Fig. 3.19: Dimensions of StS material tensile test specimen (DISSIPABLE, 2021).

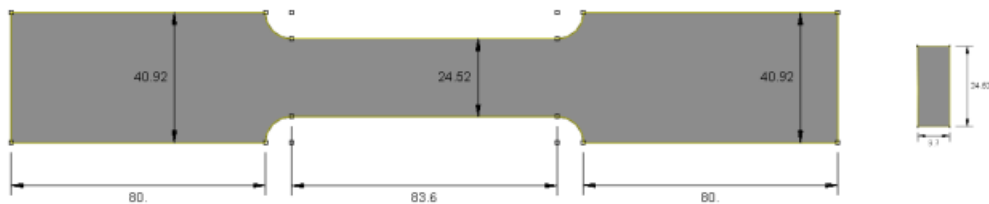


Fig. 3.20: Dimensions of S355 material tensile test specimen (DISSIPABLE, 2021).

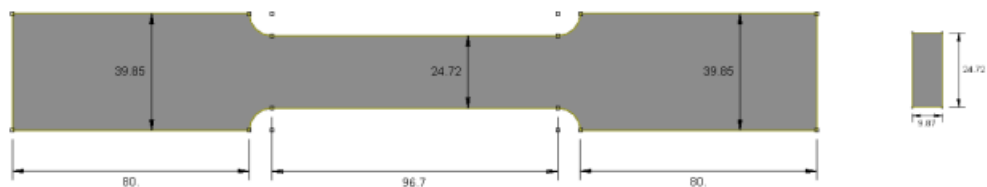


Fig. 3.21: Dimensions of HSS material tensile test specimen (DISSIPABLE, 2021).



Fig. 3.22: Dimensions of S235*(1) material tensile test specimen (DISSIPABLE, 2021).



Fig. 3.23: Dimensions of S235*(2) material tensile test specimen (DISSIPABLE, 2021).

Tab. 3.6: Dimensions of the tensile test specimens (dimension in mm).

Tensile test specimens	S235	StS	S355	HSS	S235*(1)	S235*(2)
(Free) Length	80.75	81.50	80.00	80.00	180.00	107.00
Width	-	-	24.52	24.72	-	-
Thickness	-	-	9.70	9.87	-	-
Diameter	17.9	17.85	-	-	20.00	20.00

Note (*) – material removed from untested device of the first phase of experimental tests.

The engineering and true stress-strain curves for all the materials are presented in Figure 3.25. True stress-strain curves were determined from the engineering stress-strain curves obtained experimentally and will be used to model the device behaviour with ABAQUS (DISSIPABLE, 2020). The pin materials, S235 and StS did not exhibit yielding plateau. In these cases, 0.2% offset strain method was applied to determine the yield strength. It is important to take into consideration that the pin material used in the tensile tests had already been deformed past the elastic limit from the previously dissipative device tests and may have developed plastic hardening. Anyhow, the tensile test pieces were manufactured using the interior and less undamaged volume of the pins. The engineering stress-strain curve for the pin material S235 contains higher stresses than the main characteristics determined by SOFMAN. The remaining materials, StS, S355 and HSS, show a conforming yield and tensile strength between the tensile test stress-strain curves and the characteristics determined by SOFMAN. The plate materials, S355 and HSS, did exhibit yielding plateau.

Figure 3.24 shows the tensile test specimens after failure.

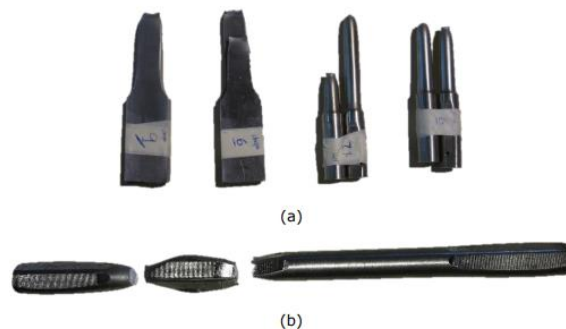


Fig. 3.24: Tested specimens of – (a) S355, HSS, StS and S235 materials, respectively and (b) S235*(1) and S235*(2) material (DISSIPABLE, 2021).

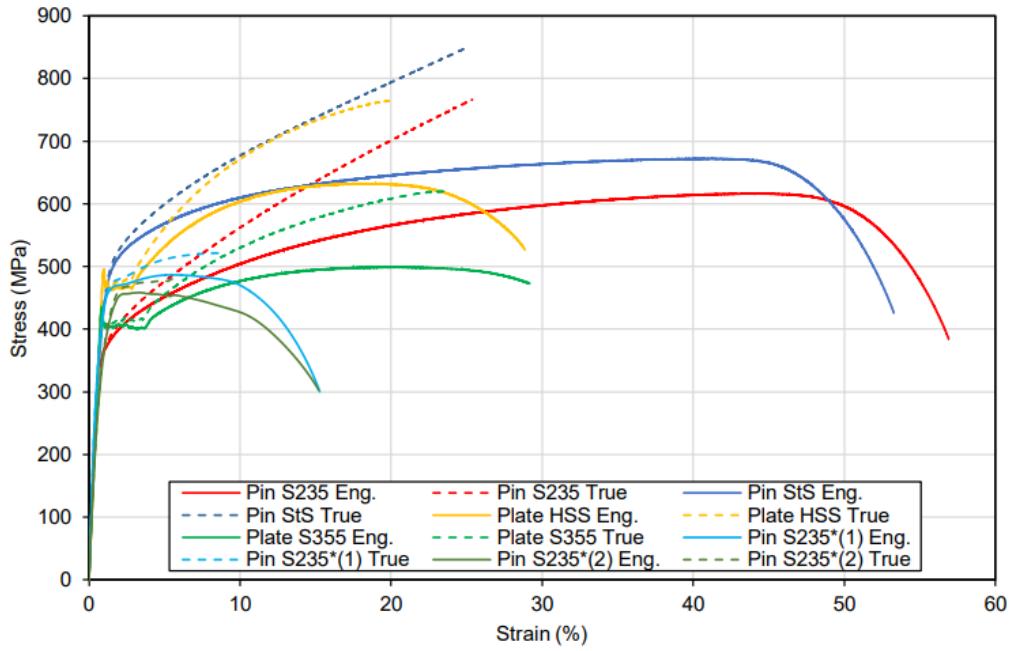


Fig. 3.25: Engineering and true stress-strain curves for all the materials.

To calculate the true stress (σ_t)-distension (ε_t) curve of the material the logarithmic law is accepted to perform the conversion accurately (equations 3.1 and 3.2) (Faridmehr et al., 2014).

$$\sigma_t = \sigma_e \times (1 + \varepsilon_e) \quad (3.1)$$

$$\varepsilon_t = \ln(1 + \varepsilon_e) \quad (3.2)$$

Average yield stress and tensile strength values obtained from the tensile tests at LERM for each tensile test performed are presented in Table 3.7.

Tab. 3.7: Main engineering characteristics obtained from the tensile tests.

Material	Component	f_y (MPa)	f_u (MPa)
S235	Pin	355	617
StS	Pin	394	672
S355	Plates	425	499
HSS	Plates	494	632
S235*(1)	Pin	370	487
S235*(2)	Pin	430	459

3.6 Results

All the experimental results are present in the report 2nd Phase Experimental Full-Scale Tests Behaviour of DRBrC Devices Results by Luís Calado, Diogo Cabrita and Nuno Rosas, 2021.

In this final dissertation some experimental tests with interesting results at the quantitative level will be presented, i.e., the devices with the highest and lowest values of significant parameters of this study will be presented: force, accumulated dissipated energy and number of cycles.

The next chapter will discuss all the results in a brief and objective way.

Translating the configuration code that serves to distinguish devices:

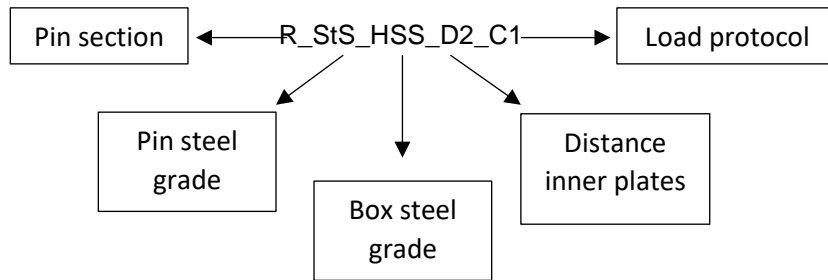


Fig. 3.26: Codename for the experimental test configurations, which is Test 26.

3.6.1 Test 05: R_S235_HSS_D1_E

It was the first experimental test to be performed.

It dictated lower values in terms of strength, although it was, within the ECCS range, the one with the most accumulated dissipated energy. It was also the ECCS test that required the fewest cycles to bring the pin to failure.

The test specimen tested, 05-R_S235_HSS_D1_E, is composed by a steel grade S235 chamfered pin and high strength steel (HSS) plates with 80/70/80 mm (D1) spacing (Fig. 3.27).

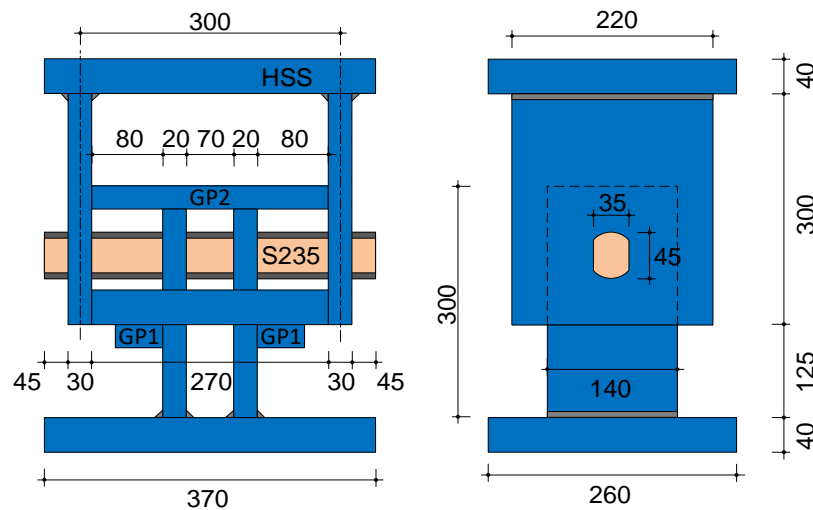


Fig. 3.27: Specimen model of test number 5.

The loading history applied consists of a hysteretic cycle following the ECCS protocol (Fig. 3.28). The test lasted 02h00m.

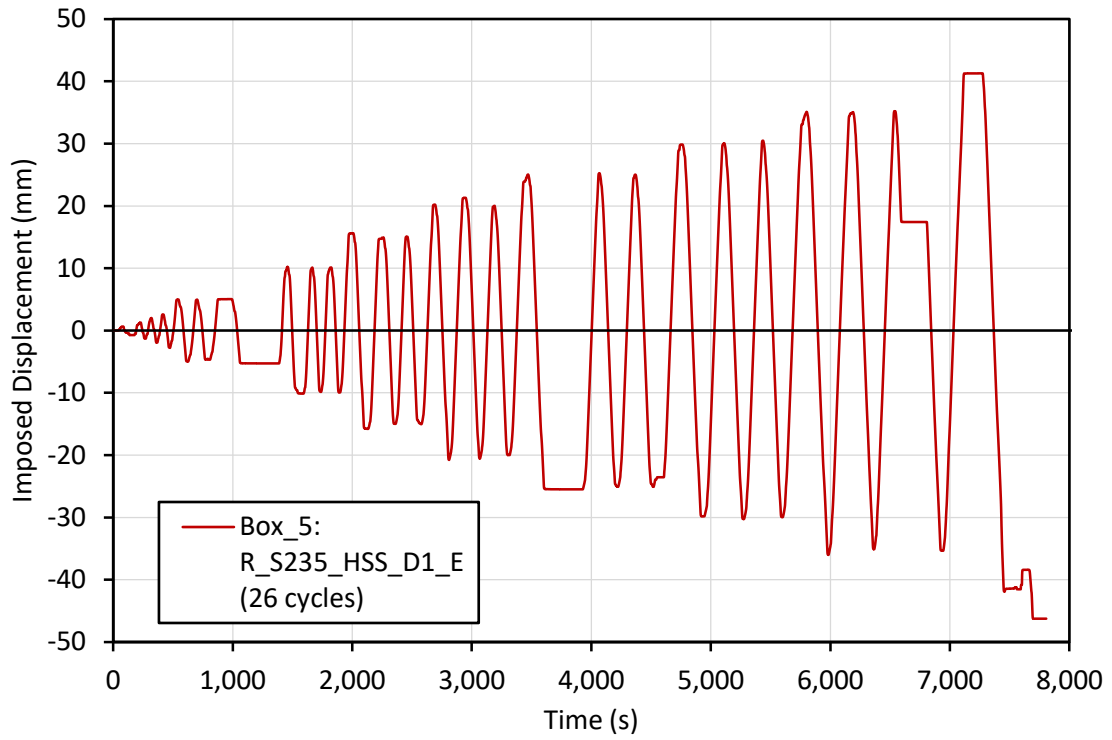


Fig.1 3.28: Load history for test number 5.

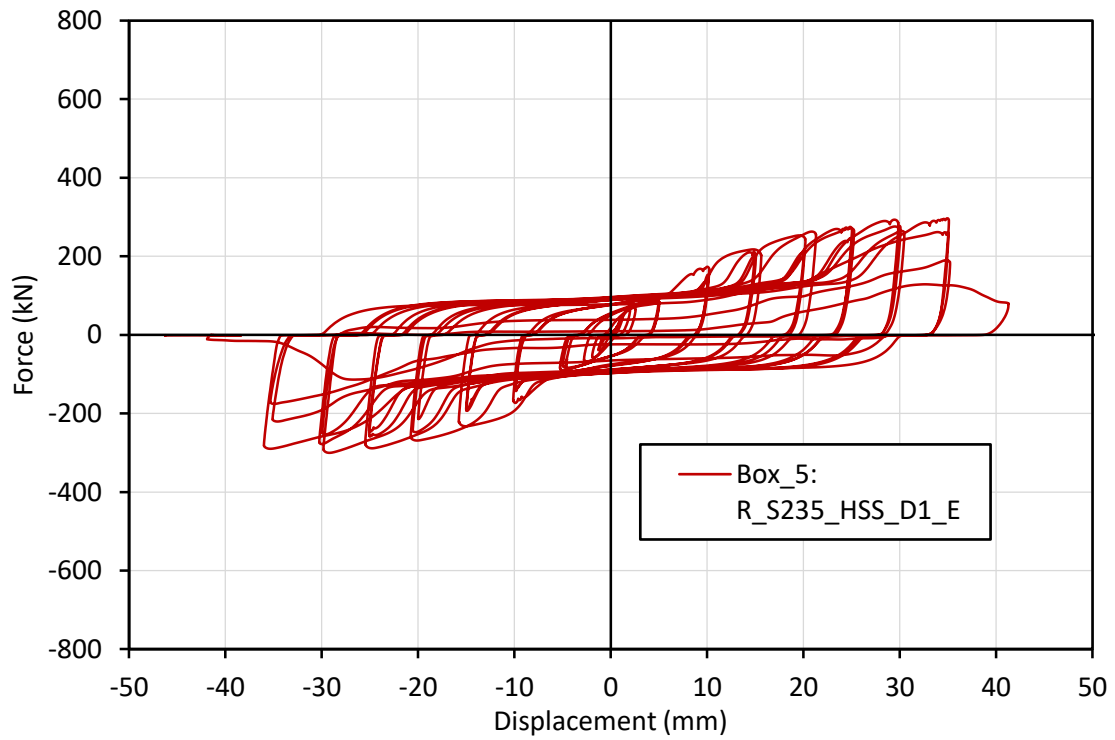


Fig. 3.29: Force-Displacement curve of test number 5.

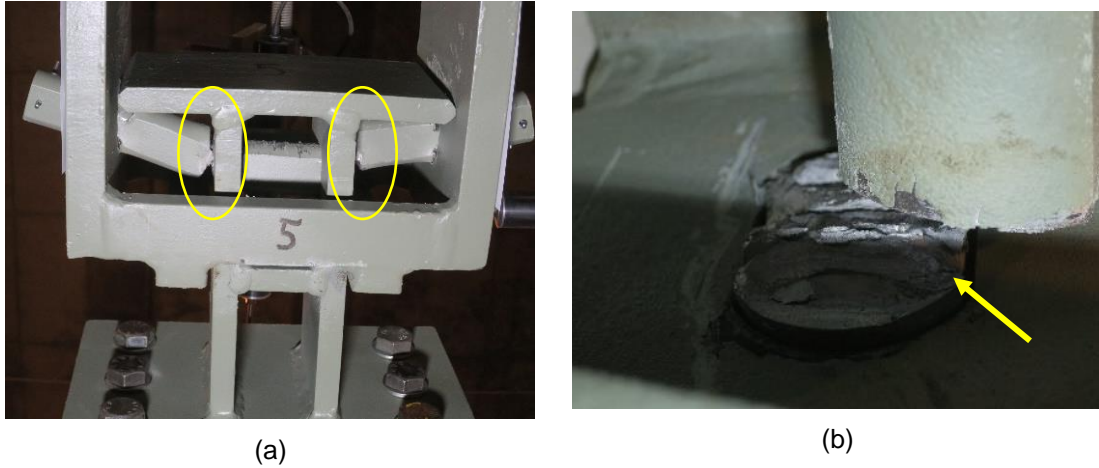


Fig. 3.30: Experimental test number 5: (a) and (b) pin failure.

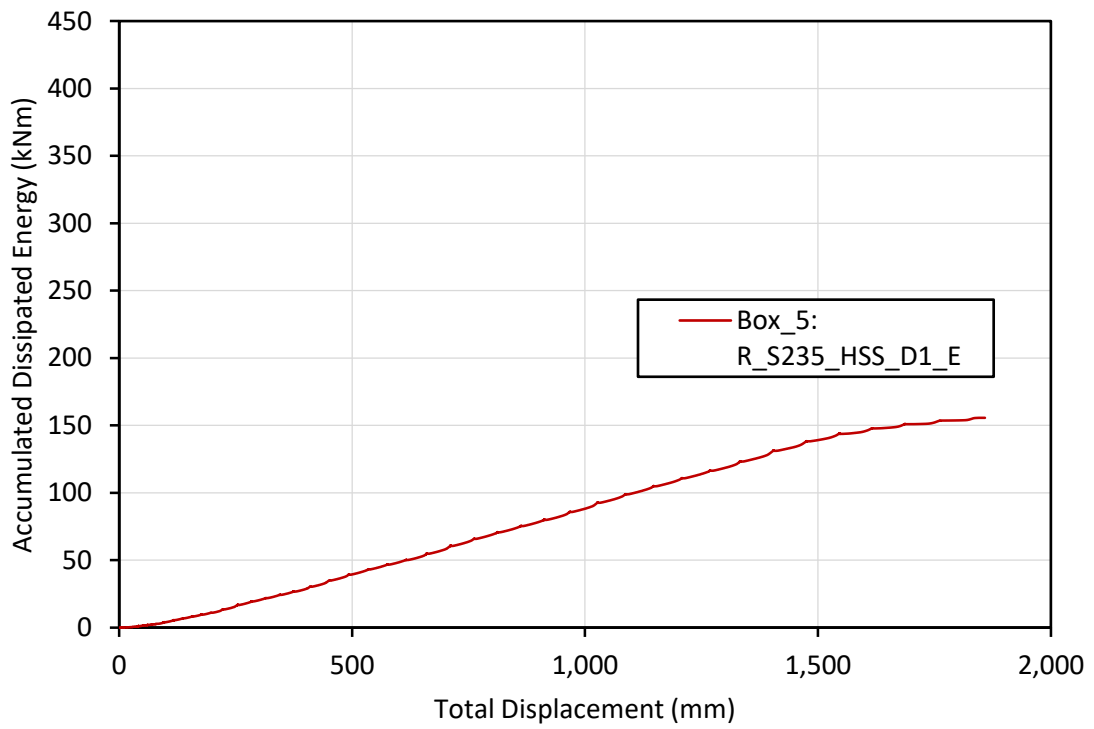


Fig. 3.31: Accumulated Dissipated Energy curve of test number 5.

Tab. 3.8: Results for experimental test 5.

	Positive	Negative
F_{max} (kN)	296.61	-300.33
δ_{max} (mm)	41.28	-46.26
Dissipated Energy (kNm)	155.64	
Nr. of cycles	26	

Note: Reached pin failure.

3.6.2 Test 13: R_StS_HSS_D1_C1

This was the test that gave the lowest results namely with the number of cycles and consequently the accumulated dissipated energy.

The test specimen tested, 13-R_StS_HSS_D1_C1, is composed by a stainless steel (StS) chamfered pin and high strength steel (HSS) plates with 80/70/80 mm (D1) spacing (Fig. 3.32).

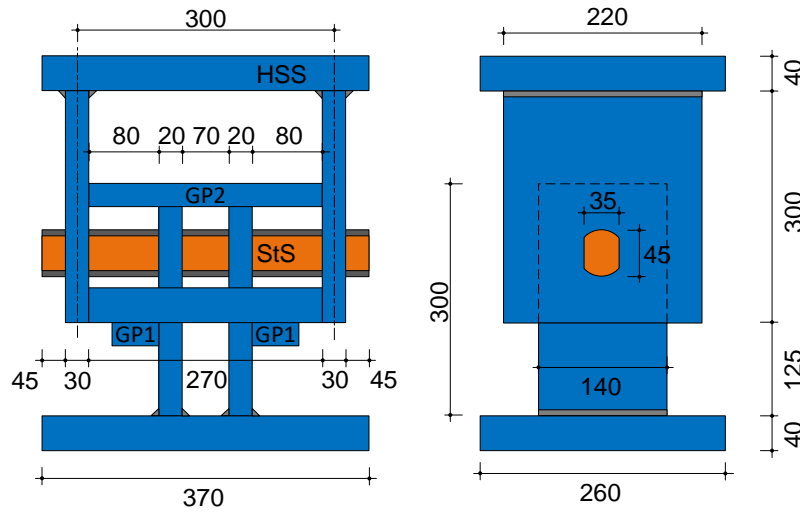


Fig. 3.32: Specimen model of test number 13.

The loading history applied consists of a constant amplitude cycle of 30mm (Fig. 3.33). The test lasted approximately 2h.

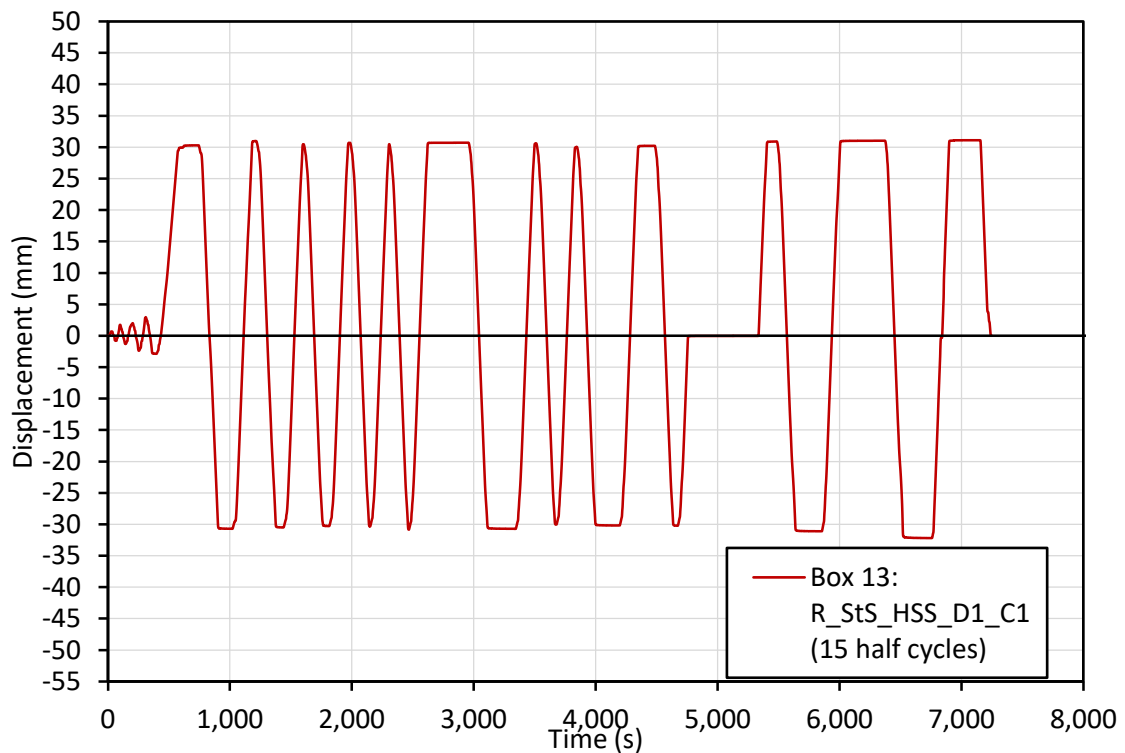


Fig. 3.33: Load history for test number 13.

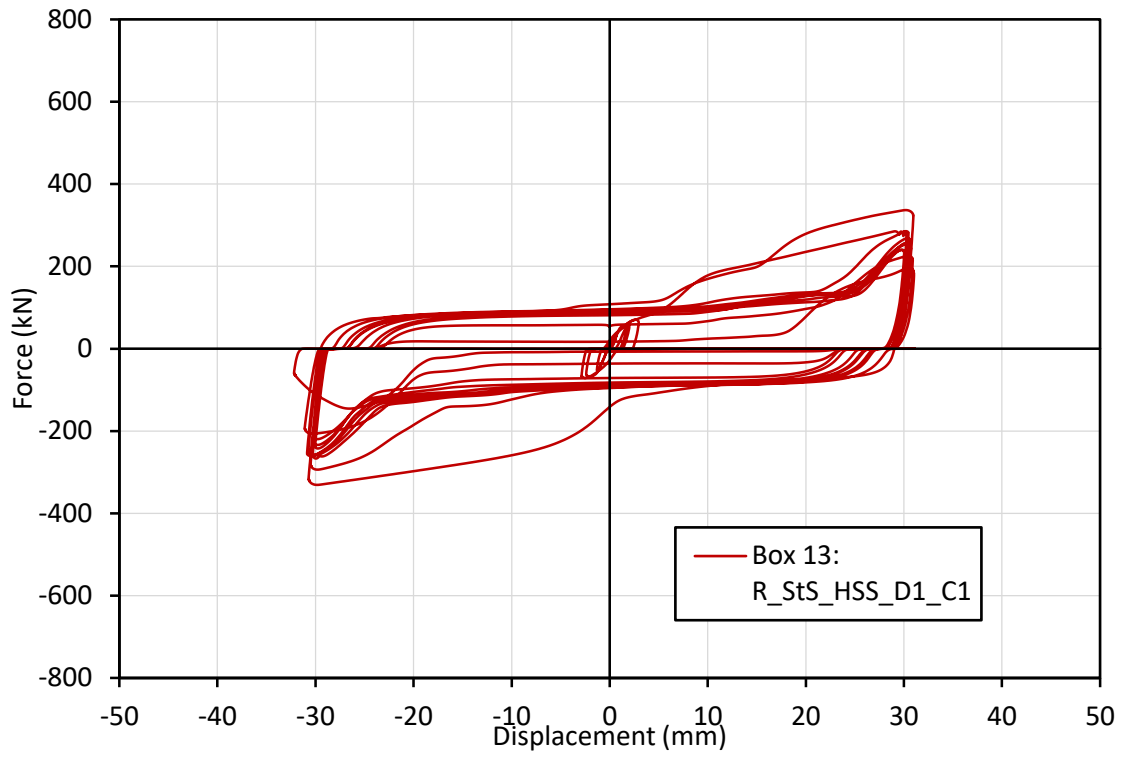
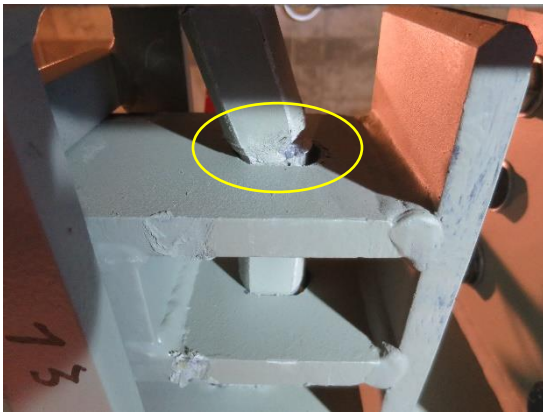
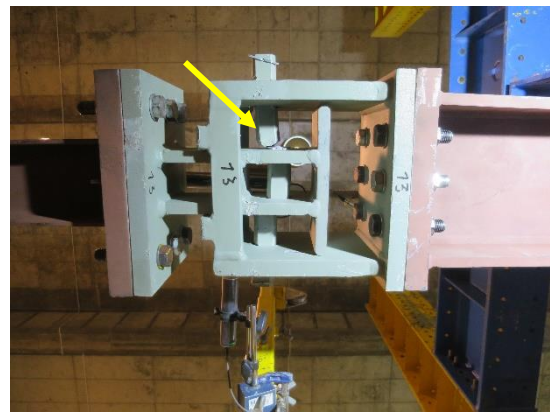


Fig. 3.34: Force-Displacement curve of test number 13.



(a)



(b)

Fig. 3.35: Experimental test number 13: (a) pin failure; (b) division of the pin.

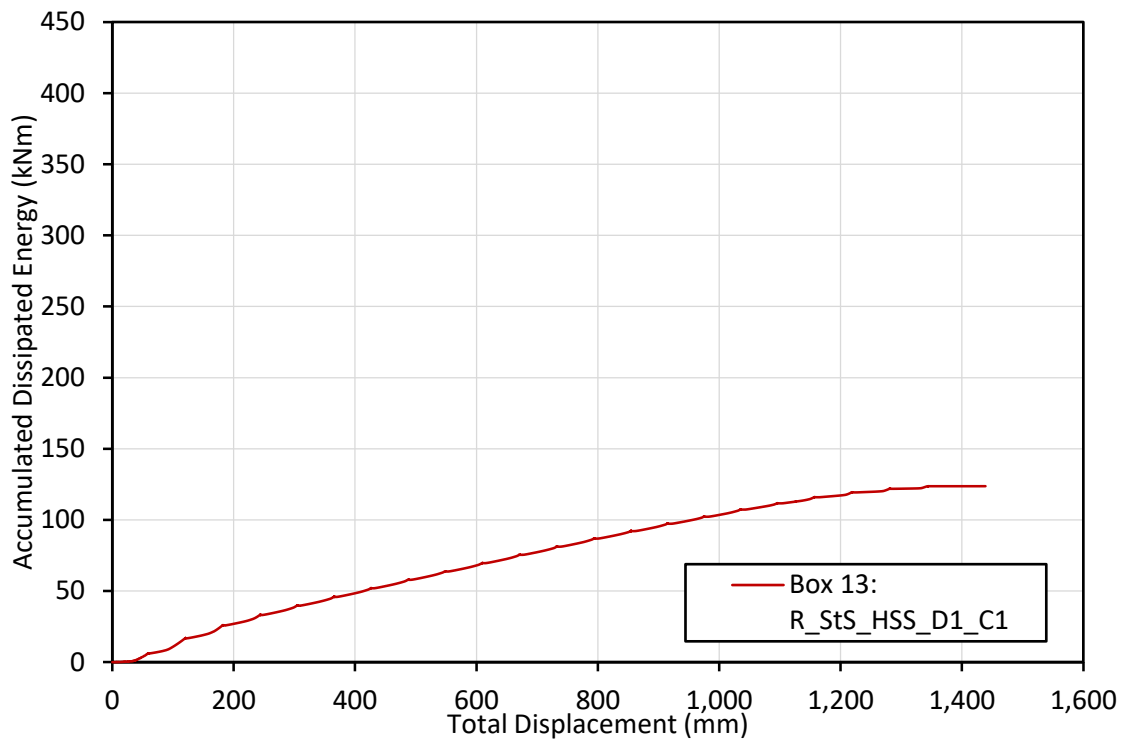


Fig. 3.36: Accumulated Dissipated Energy curve of test number 13.

Tab. 3.9: Results for experimental test 13.

	Positive	Negative
F_{max} (kN)	336.69	-330.80
δ_{max} (mm)	31.10	-32.19
Dissipated Energy (kNm)	123.70	
Nr. of cycles	15.5	

Note: Reached pin failure.

3.6.3 Test 19: R_S235_HSS_D2_E

In contrast, this was the test that gave the highest values for the three parameters mentioned in 3.6. It should be noted that the number of cycles is comparative to all the ECCS's performed, since there was another test that needed more cycles to lead to failure which is presented in the following subchapter.

The test specimen tested, 19-R_S235_HSS_D2_E, is composed by a steel grade S235 chamfered pin and high strength steel (HSS) plates with 70/90/70 mm (D2) spacing (Fig. 3.37).

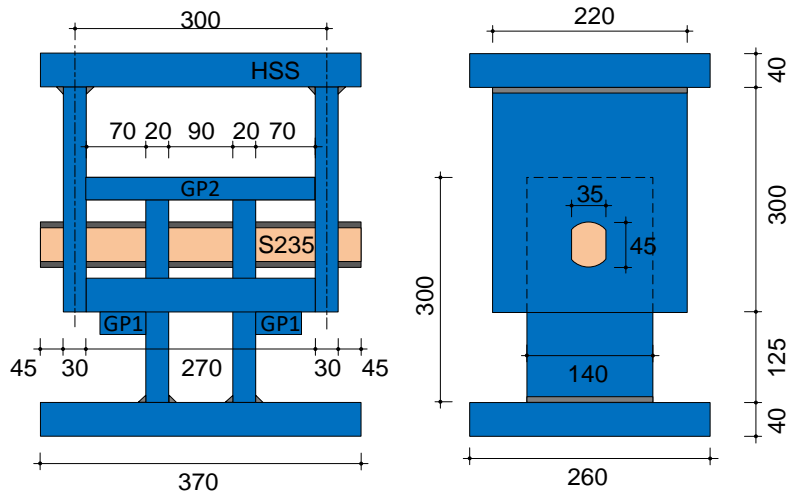


Fig. 3.37: Specimen model of test number 19.

The loading history applied consists of a hysteretic cycle following the ECCS protocol (Fig. 3.38). The test lasted 3h00m.

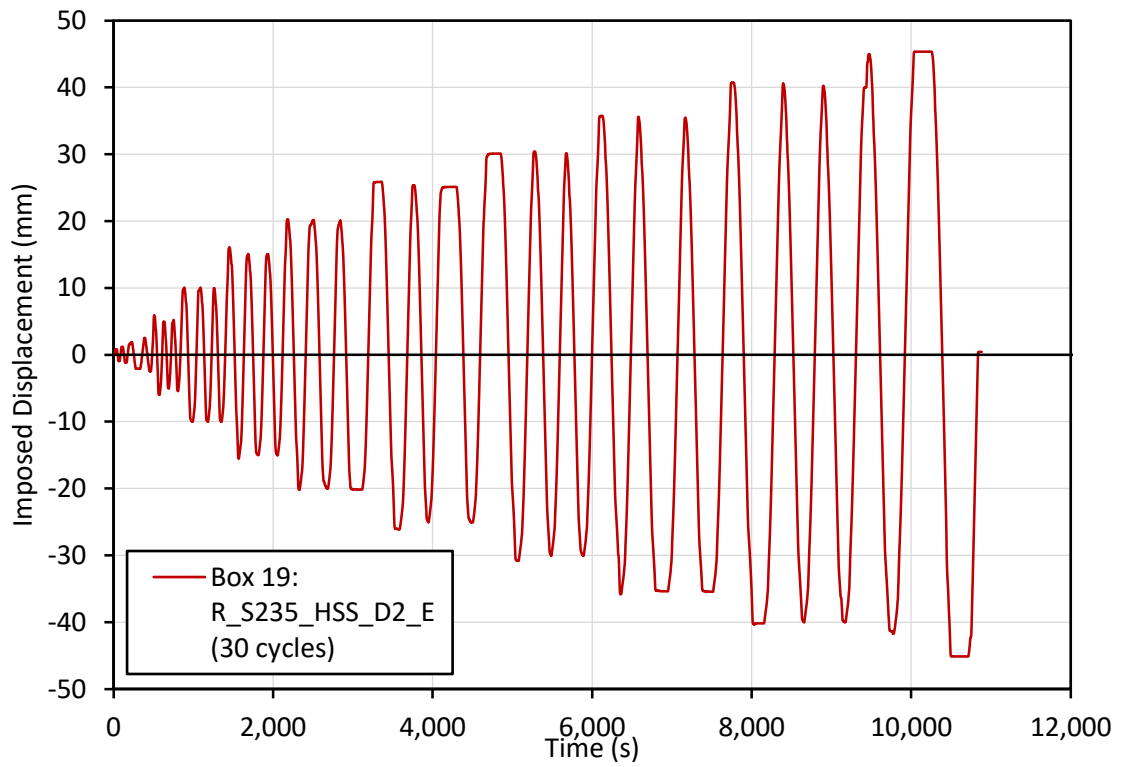


Fig. 3.38: Load history for test number 19.

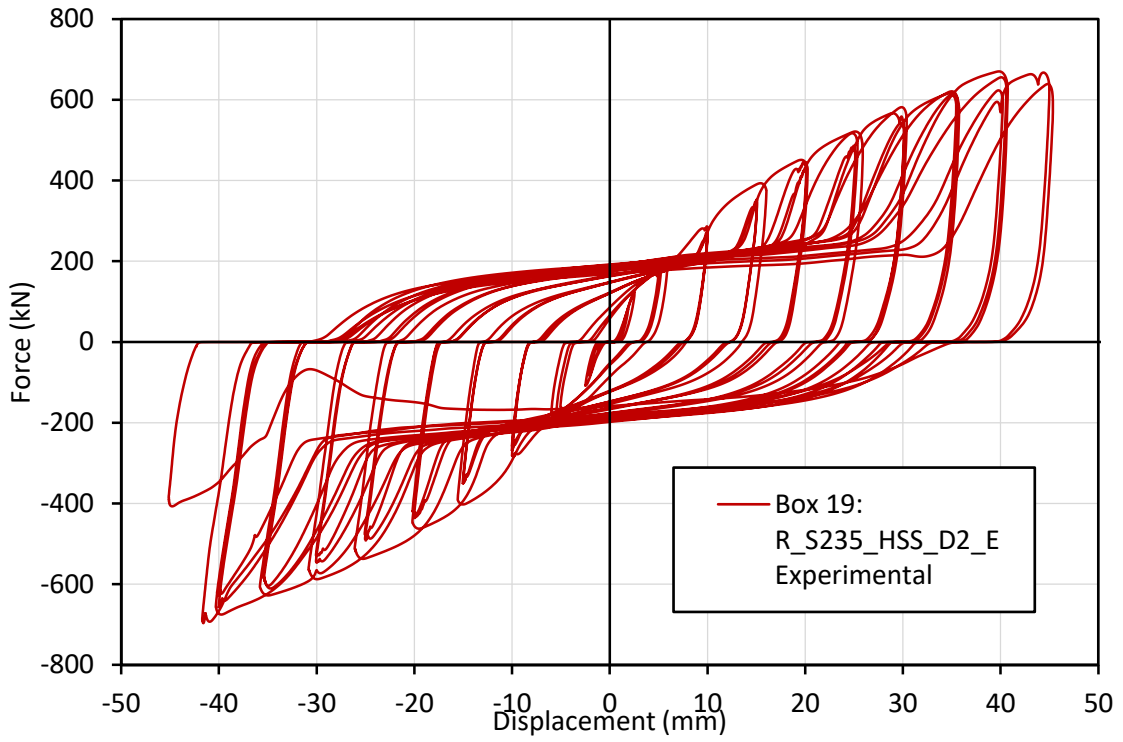
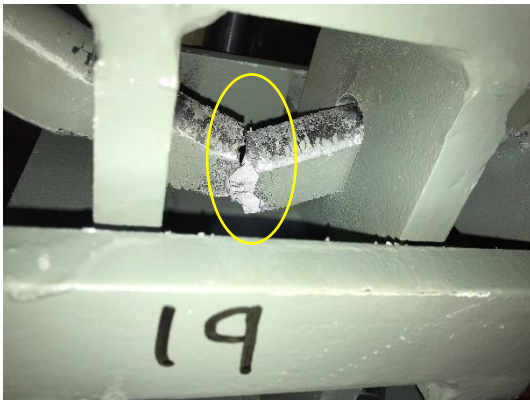


Fig. 3.39: Force-Displacement curve of test number 19.



(a)



(b)

Fig. 3.40: Experimental test number 19: (a) failure mode; (b) pin elongation.

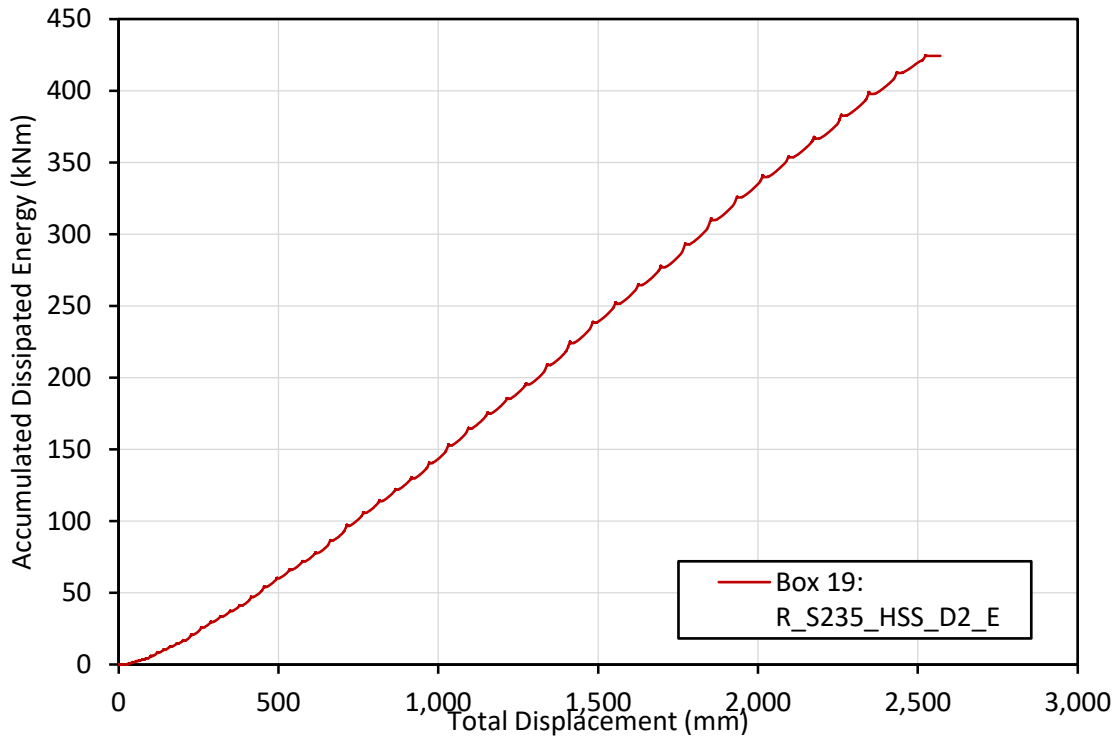


Fig. 3.41: Accumulated Dissipated Energy curve of test number 19.

Tab. 3.101: Results for experimental test 19.

	Positive	Negative
F_{max} (kN)	670.23	-696.33
δ_{max} (mm)	45.35	-45.14
Dissipated Energy (kNm)	424.30	
Nr. Of cycles	30	

Note: Reached pin failure.

3.6.4 Test 20: R_S235_HSS_D2_C1

It was a test in which the force presented low values, the lowest compared to the other tests in which a constant amplitude was applied, and thus a greater number of cycles was required as well as a graduation of amplitudes for the failure of the pin, in which was the test with more cycles.

The test specimen tested, 20-R_S235_HSS_D2_C1, is composed by a steel grade S235 chamfered pin and high strength steel (HSS) plates with 70/90/70 mm (D2) spacing (Fig. 3.37).

The loading history applied consists of a constant amplitude cycle of 20 mm, with a crescent amplitude of 5mm after cycle 61 (Fig. 3.42). The test lasted 5h00m.

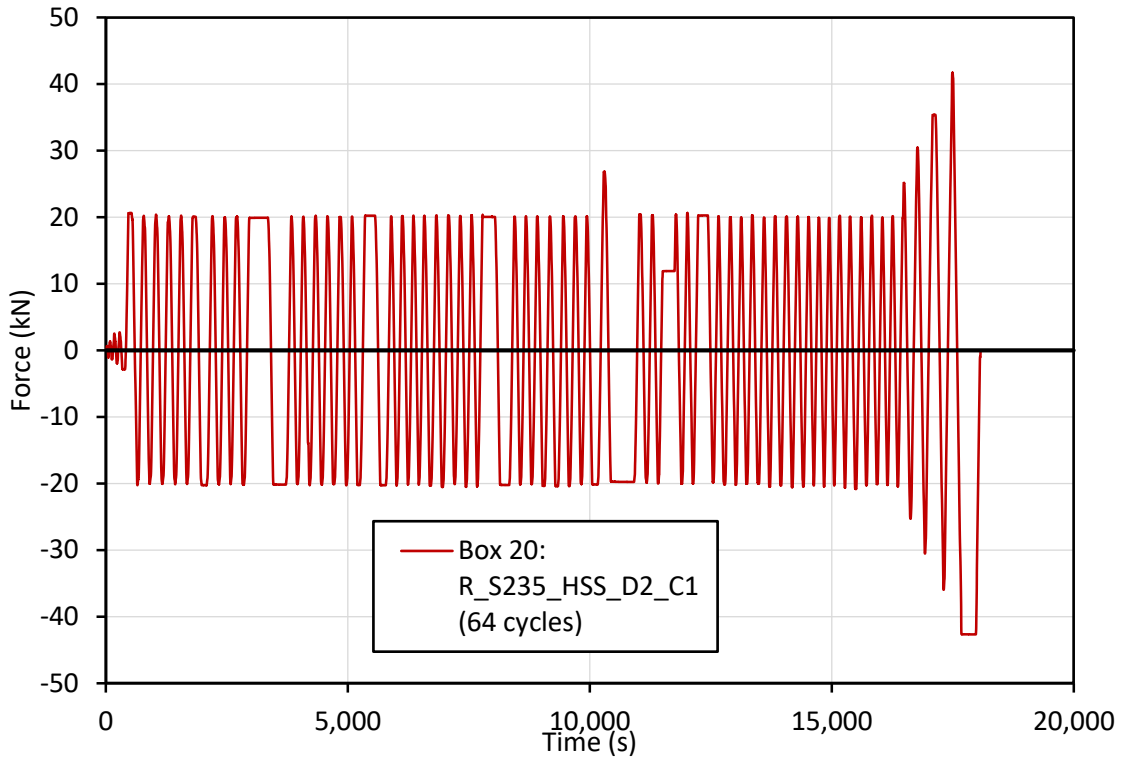


Fig. 3.42: Load history for test number 20.

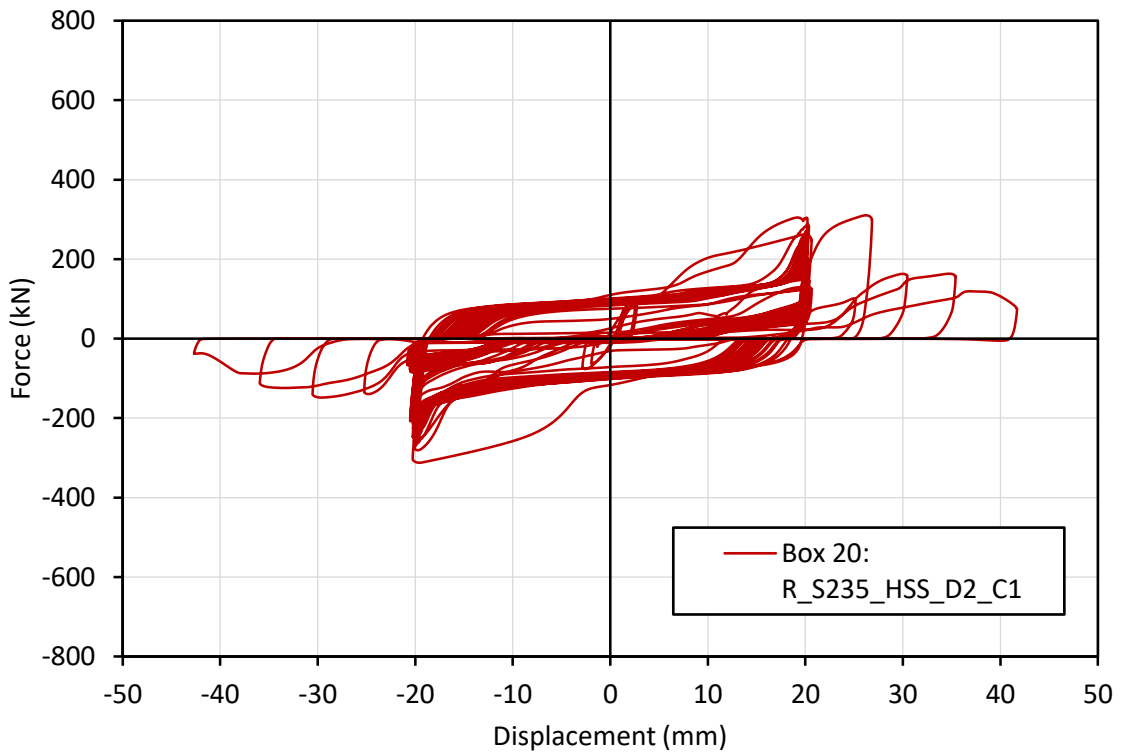
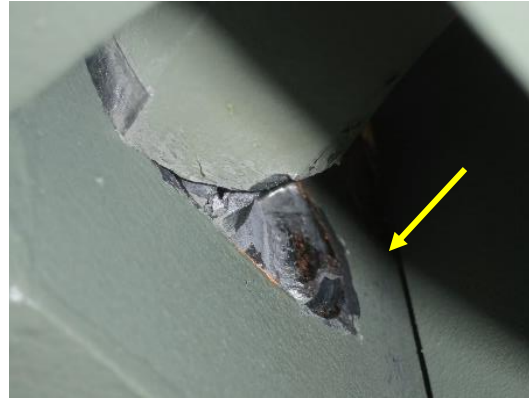


Fig. 3.43: Force-Displacement curve of test number 20.



(a)



(b)

Fig. 3.44: Experimental test number 20: (a) failure mode; (b) pin failure.

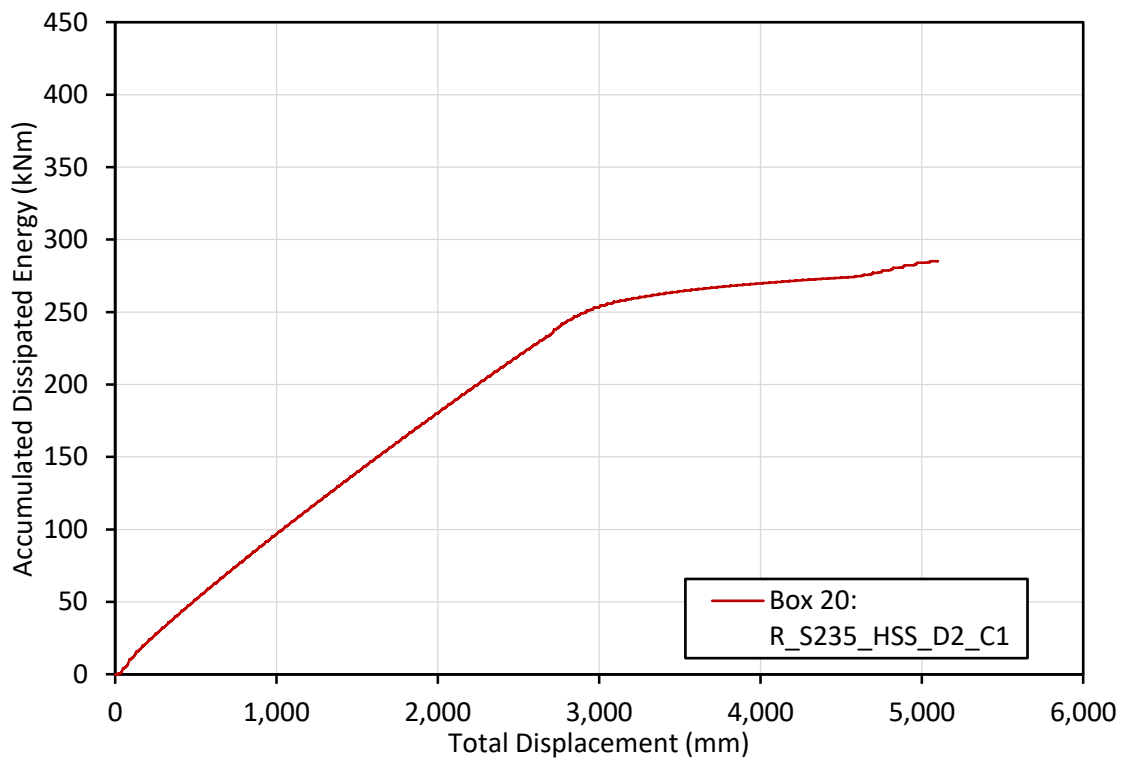


Fig. 3.45: Accumulated Dissipated Energy curve of test number 20.

Tab. 3.11: Results for experimental test 20.

	Positive	Negative
F_{max} (kN)	310.20	-312.24
δ_{max} (mm)	41.70	-42.67
Dissipated Energy (kNm)	285.09	
Nr. of cycles	64	

Note: Reached pin failure.

4. Parametric Analysis

The parameters for comparative analysis between specimens are the same as mentioned in subchapter 3.6 where specimens with the highest and lowest values were selected.

In this 2nd phase of the DISSIPABLE project we tested 6 combinations of different specimen configurations and thus there are several ways to analyse and compare results like:

- Pin: S235vsStS.
- Box: S355vsHSS.
- Distance between inner plates: D1vsD2.

It should be noted that in the following graphs there are no units due to the single fact of visualization. Therefore, the Force-Displacement graphs (left) on the abscissae are the displacements in mm and on the ordinates are the forces in kN, while the Accumulated Dissipated Energy graphs (right) on the abscissae are the total displacement, i.e., the sum of the imposed amplitudes, and the ordinates are then the energy.

4.1 Pins: S235vsStS

The type of steel of the pins must be less resistant than that of the box plates so that they can distribute the seismic force by contact with the plates as if they were mobile supports and thus be the easiest element to replace.

4.1.1 HSS+D1

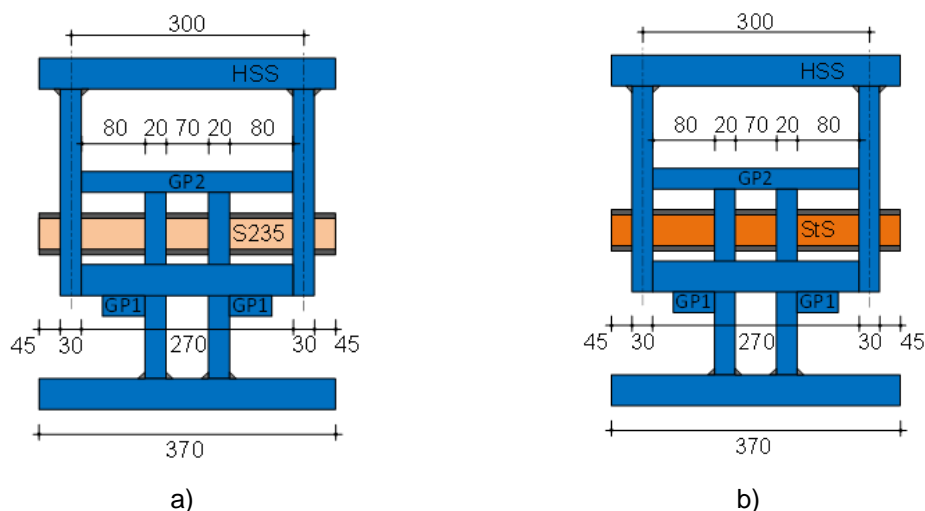


Fig. 4.1: Specimen S235_HSS_D1 (a) and StS_HSS_D1 (b).

This subchapter will compare devices 05 with 12 (ECCS) (fig. 4.2 a)), 07 with 13 (C=30mm) (fig. 4.2 b)) and 08 with 14 (C=25mm) (fig. 4.2 c)). The overlapping graphs are shown in the following figure.

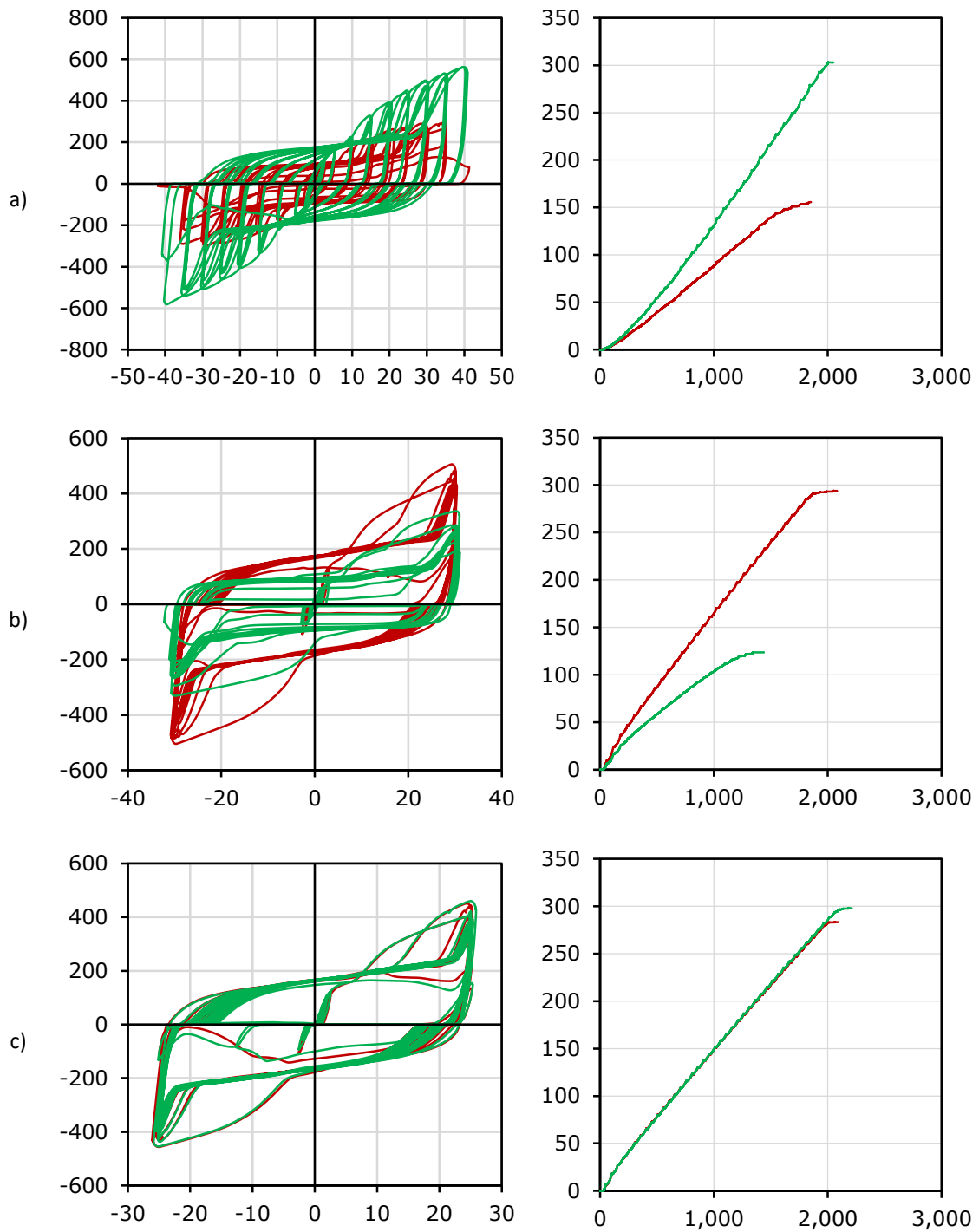


Fig. 4.2: Comparisons between S235_HSS_D1 (red) with StS_HSS_D1 (green).

S235 has lower values in the ECCS test, but at constant amplitude of 30mm it is the opposite. At 25mm, the values are similar. The discrepancy in values is present if we compare the S235_HSS_D1 in the constant amplitude tests, where they are double compared to the ECCS. In StS_HSS_D1, it is the other way round, i.e., the imposed constant amplitude values of 30mm are half of the ECCS. StS in constant amplitude imposed tests is less efficient than in ECCS and S235 is the inverse.

It should be noted that regardless of its configuration the maximum accumulated dissipated energy is 300kNm and the pin does not resist more than 2m of imposed amplitudes.

The following table makes a comparison at the level of maximum values.

Tab. 4.1: Variation percentage of Force and Energy.

	F _{máx} (kN)	F _{mín} (kN)	ΔF (%)	E _{máx} (kNm)	E _{mín} (kNm)	ΔE (%)
ECCS	581.64 (StS)	300.33 (S235)	93.67	303.00 (StS)	155.64 (S235)	82.00
C25	459.81 (StS)	456.12 (S235)	0.81	297.91 (StS)	283.27 (S235)	5.17
C30	505.77 (S235)	336.69 (StS)	50.22	293.86 (S235)	123.70 (StS)	137.56

4.1.2 HSS+D2

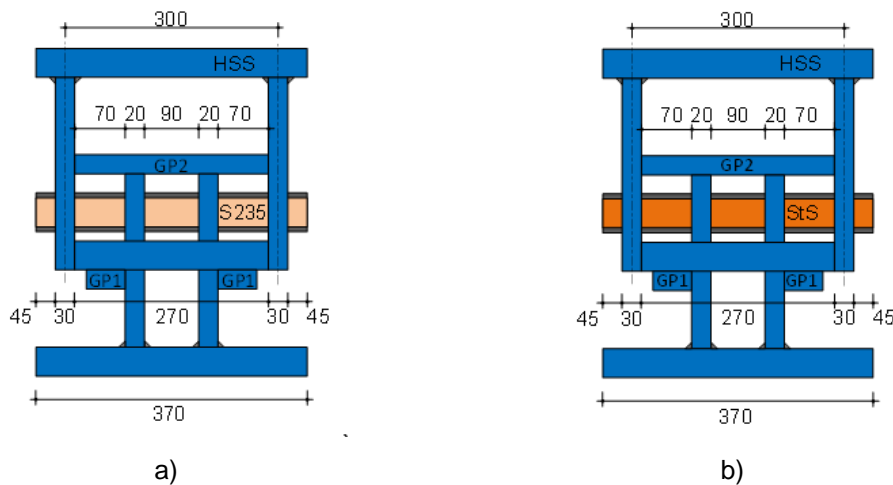


Fig. 4.3: Specimen S235_HSS_D2 (a) and StS_HSS_D2 (b).

This subchapter will compare devices 19 with 26 (ECCS) (fig. 4.4 a)), 21 with 27 (C=30mm) (fig. 4.4 b)) and 22 with 28 (C=25mm) (fig. 4.4 c)). The overlapping graphs are shown in the following figure.

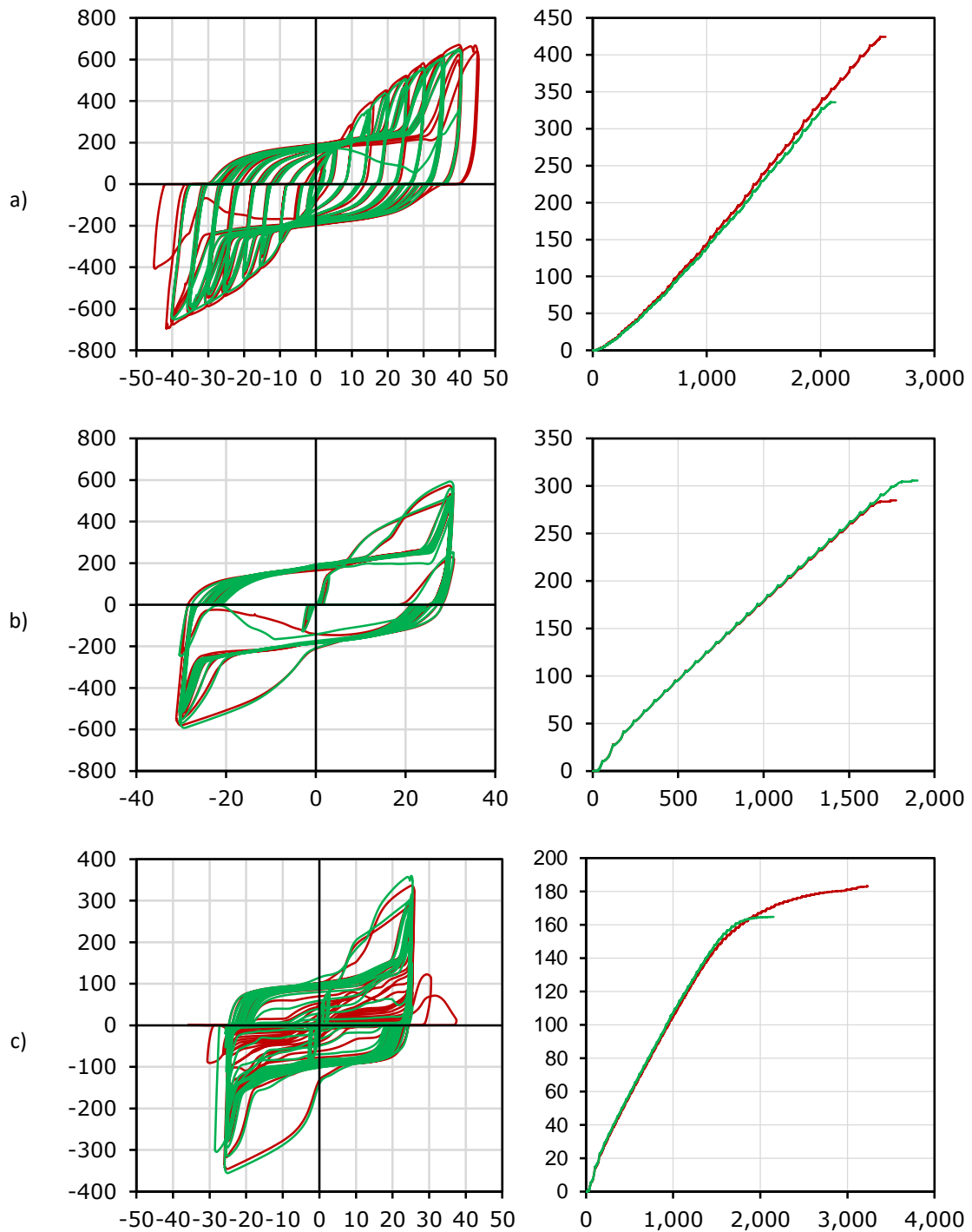


Fig. 4.4: Comparisons between S235_HSS_D2 (red) with StS_HSS_D2 (green).

The tests have very similar results. It should be noted that the device S235_HSS_D2 had a good fatigue resistance which was necessary to increase amplitude to bring it to failure (fig. 4.4 c)). In comparison of values, the ECCS had inferior compared to the constant imposed amplitude of 25mm.

The following table makes a comparison at the level of maximum values.

Tab. 4.2:2 Variation percentage of Force and Energy.

	F _{máx} (kN)	F _{mín} (kN)	ΔF (%)	Emáx (kNm)	Emín (kNm)	ΔE (%)
ECCS	696.33 (S235)	651.33 (StS)	6.45	424.30 (S235)	335.76 (StS)	26.37
C25	359.52 (StS)	345.45 (S235)	4.07	183.19 (S235)	164.74 (StS)	11.20
C30	593.40 (StS)	580.62 (S235)	2.20	305.72 (StS)	284.84 (S235)	7.33

4.2 Plates: S355vsHSS

As mentioned 4.1, the plates of the boxes are made of a type of steel with greater strength in order to confine much of the earthquake energy in the pin.

4.2.1 StS+D1

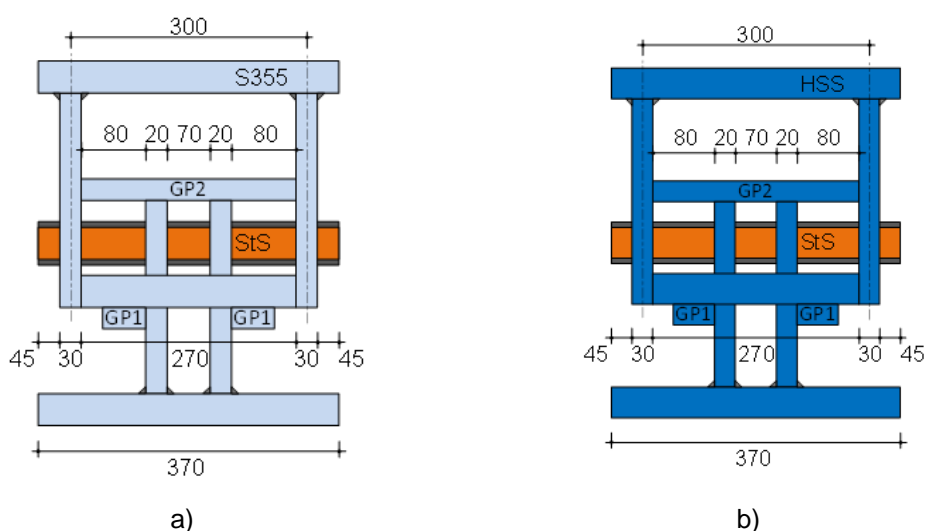


Fig. 4.5: Specimen StS_S355_D1 (a) and StS_HSS_D1 (b).

This subchapter will compare devices 09 with 12 (ECCS) (fig. 4.6 a)), 10 with 13 (C=30mm) (fig. 4.6 b)) and 11 with 14 (C=25mm) (fig. 4.6 c)). The overlapping graphs are shown in the following figure.

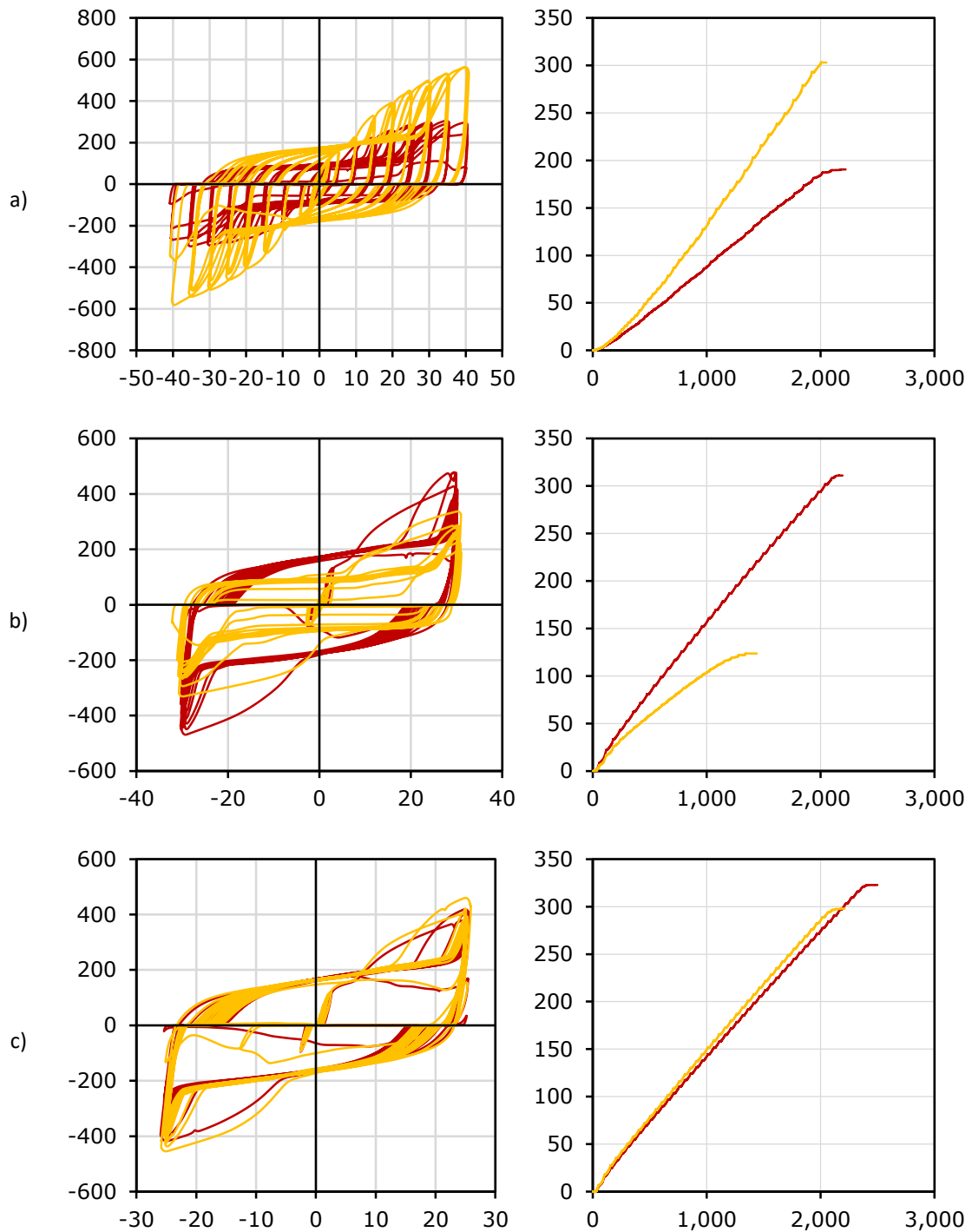


Fig. 4.6: Comparisons between StS_S355_D1 (red) with StS_HSS_D1 (yellow).

In this analysis the HSS device had lower values in the imposed constant amplitudes, what in ECCS was the opposite compared with S355. The HSS has compatible values with the amplitude of 25mm, already with amplitude of 30mm these values are twice higher. With S355 the imposed amplitudes resulted values also twice higher in relation to ECCS. Finally, it should be noted that the HSS in tests with constant imposed amplitudes became less efficient than in ECCS and vice-versa with S355.

As explicit in the comparison of the pin with HSS+D1 devices, here too the maximum accumulated dissipated energy does not go much beyond 300kNm as the imposed amplitudes are not much more than 2m.

The following table makes a comparison at the level of maximum values.

Tab. 4.3:3 Variation percentage of Force and Energy.

	Fm _{áx} (kN)	Fm _{ín} (kN)	ΔF (%)	Em _{áx} (kNm)	Em _{ín} (kNm)	ΔE (%)
ECCS	581.64 (HSS)	305.88 (S355)	90.15	303.00 (HSS)	190.45 (S355)	59.10
C25	459.81 (HSS)	418.29 (S355)	9.23	321.10 (S355)	297.91 (HSS)	7.78
C30	478.20 (HSS)	336.69 (S355)	42.03	311.02 (S355)	123.70 (HSS)	151.43

4.2.2 StS+D2

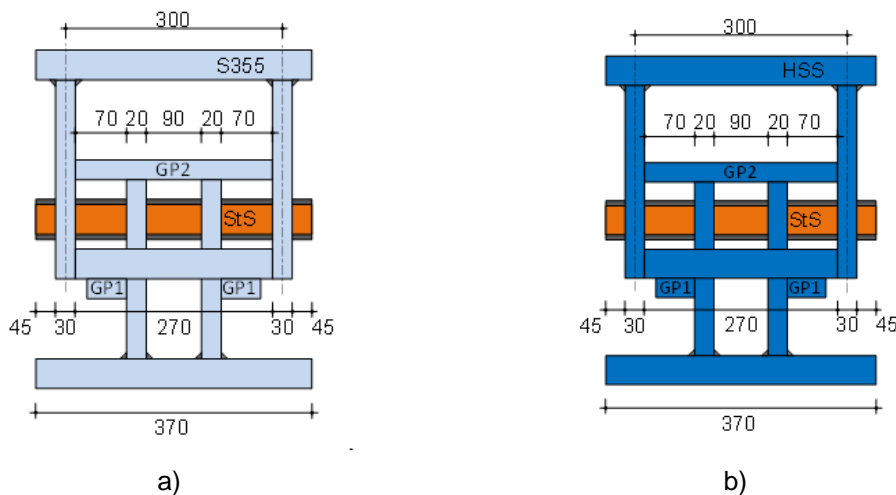


Fig. 4.7: Specimen StS_S355_D2 (a) and StS_HSS_D2 (b)).

This subchapter will compare devices 23 with 26 (ECCS) (fig. 4.8 a)), 24 with 27 (C=30mm) (fig. 4.8 b)) and 25 with 28 (C=25mm) (fig. 4.8 c)). The overlapping graphs are shown in the following figure.

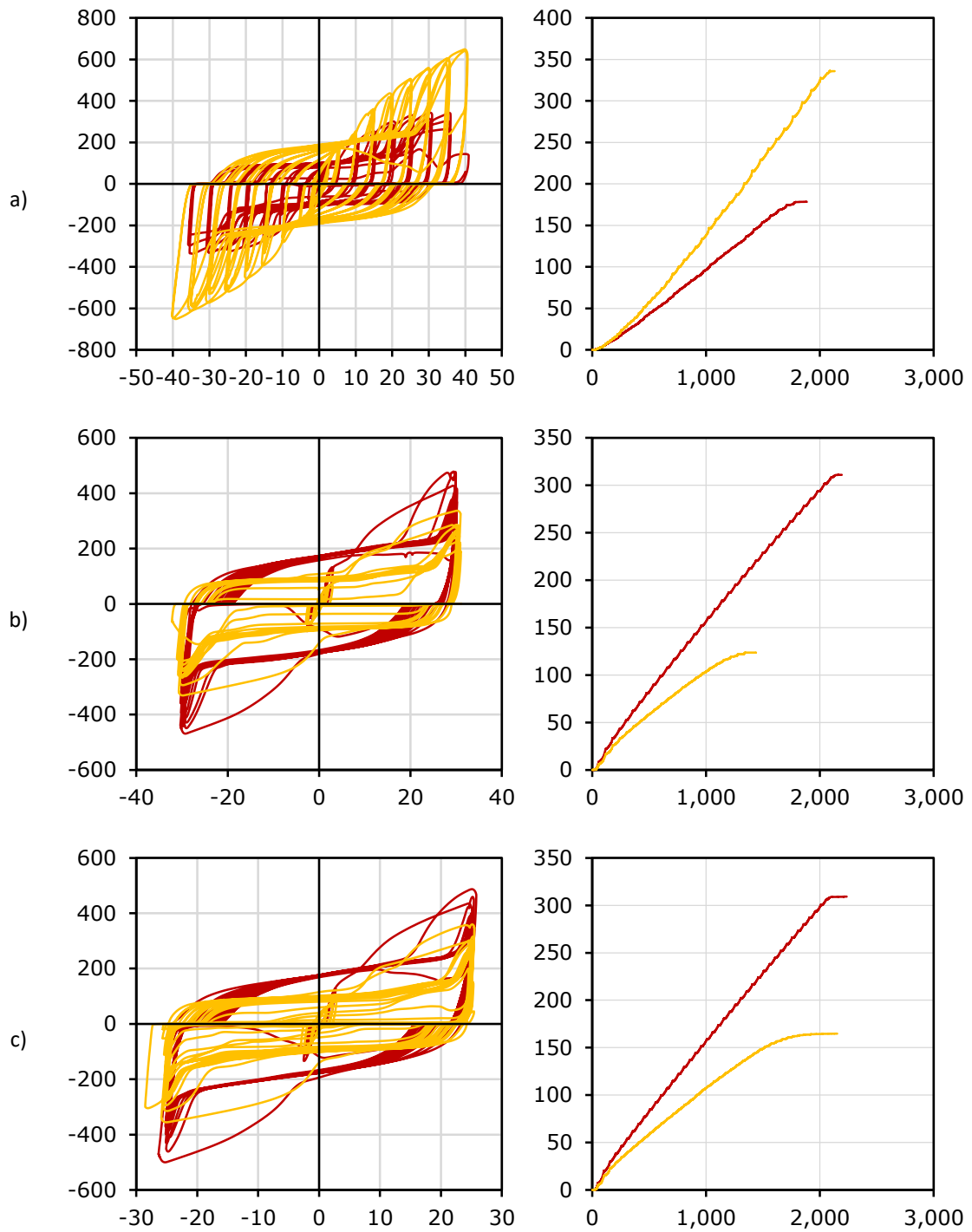


Fig. 4.8: Comparisons between StS_S355_D2 (red) with StS_HSS_D2 (yellow).

Very similar conclusions were obtained with D1. Comparing ECCS with the imposed constant amplitudes, the HSS case had much lower values with 30mm, while with 25mm HSS had +100kN and the other case -100kN.

The following table makes a comparison at the level of maximum values.

Tab. 4.4: Variation percentage of Force and Energy.

	Fmáx (kN)	Fmín (kN)	ΔF (%)	Emáx (kNm)	Emín (kNm)	ΔE (%)
ECCS	651.33 (HSS)	343.20 (S355)	89.78	335.76 (HSS)	178.51 (S355)	88.09
C25	500.04 (S355)	359.52 (HSS)	39.09	309.20 (S355)	164.74 (HSS)	87.69
C30	593.40 (S355)	366.78 (HSS)	61.79	305.72 (HSS)	236.96 (S355)	29.02

4.3 D1vsD2

The distance between plates is central to the study of ovalizations, since the greater this distance, the greater the interior ovalization, and vice versa.

4.3.1 S235+HSS

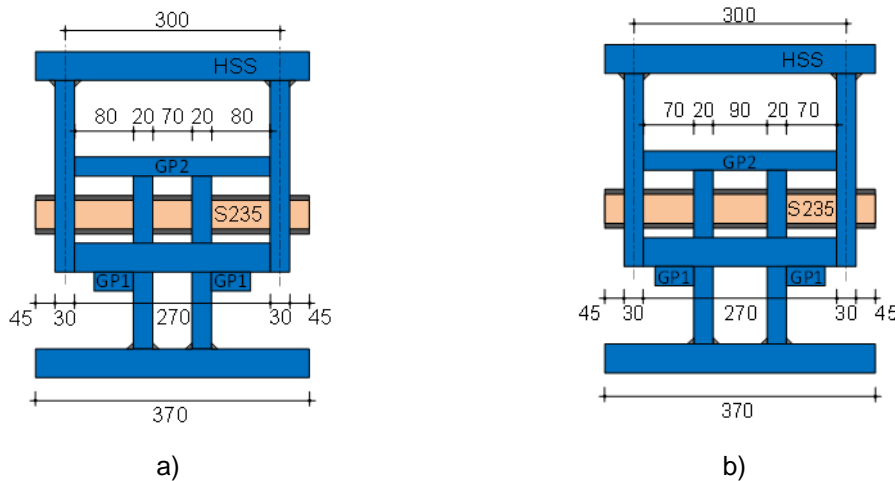
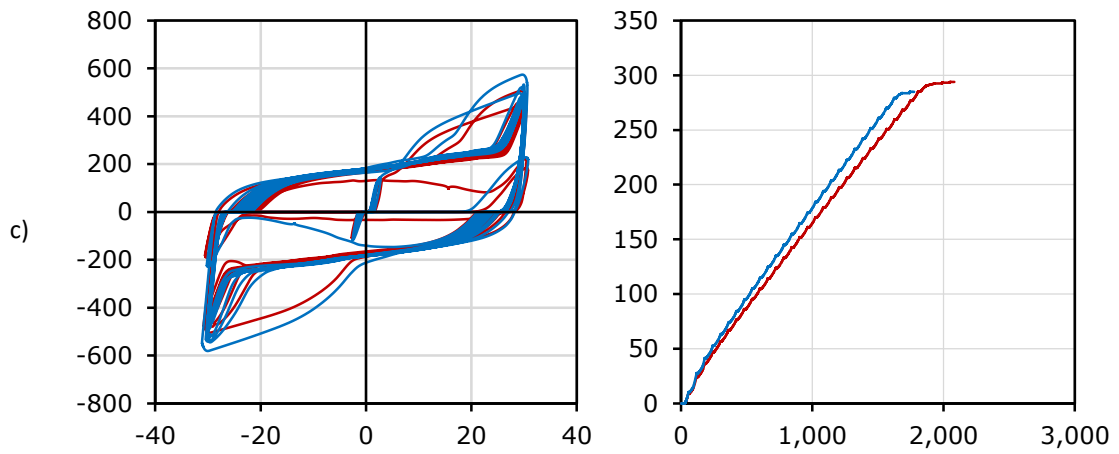
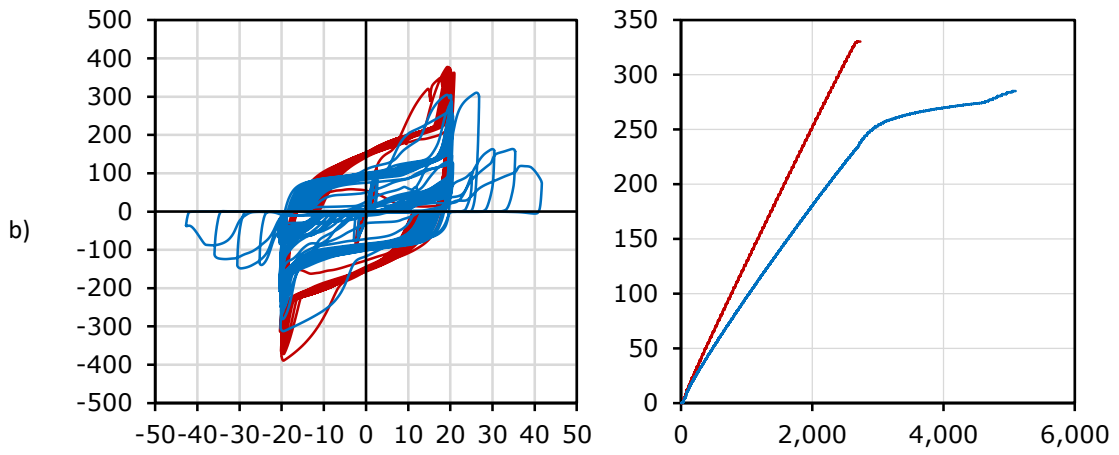
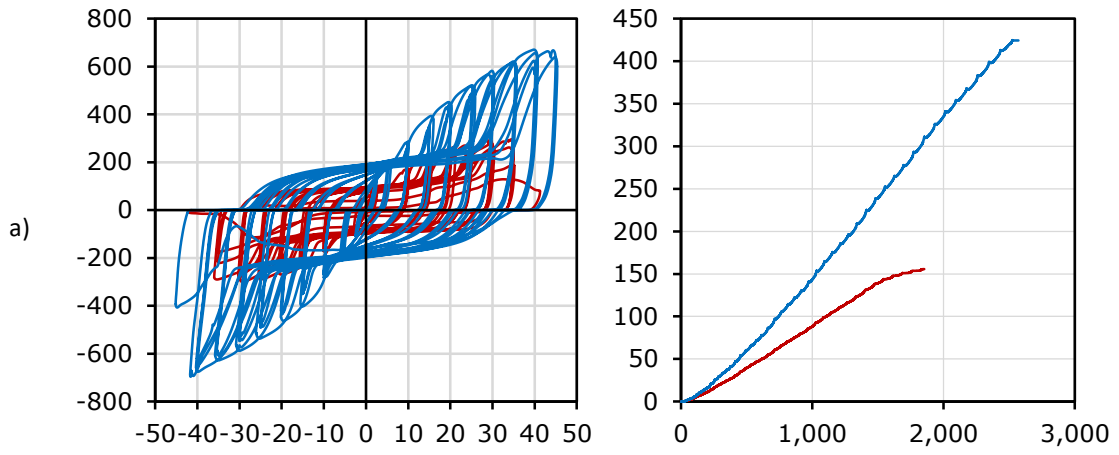


Fig. 4.9: Specimen S235_HSS_D1 (a) and S235_HSS_D2 (b).

This subchapter will compare devices 05 with 19 (ECCS) (fig. 4.10 a)), 06 with 20 (C=20mm) (fig. 4.10 b)), 07 with 21 (C=30mm) (fig. 4.10 c)) and 08 with 22 (C=25mm) (fig. 4.10 d)). The overlapping graphs are shown in the following figure.



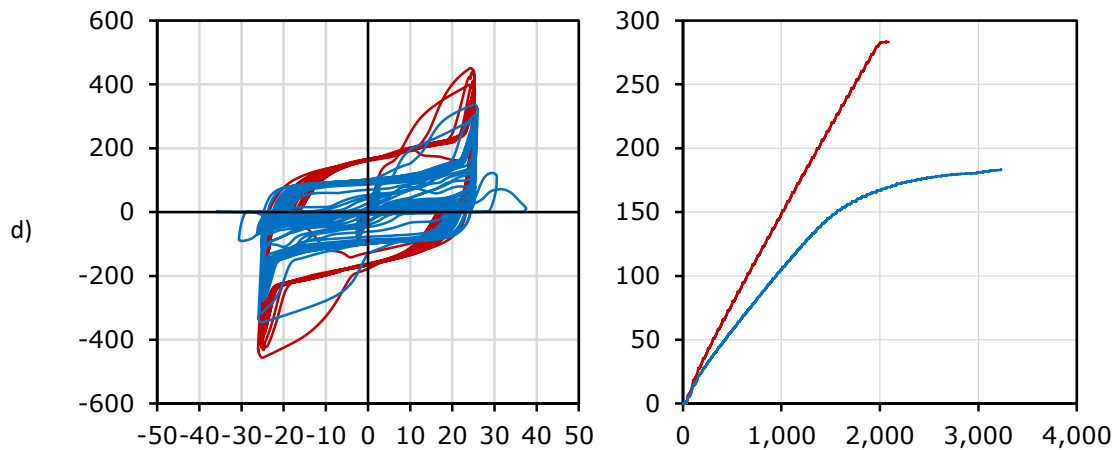


Fig. 4.10: Comparisons between S235_HSS_D1 (red) with S235_HSS_D2 (blue).

In this analysis we found that D1 had lower values in ECCS, but higher in constant imposed amplitude of 20mm compared to D2. In the remaining amplitudes everything was similar. Note the high ductility, that sometimes was necessary to increase the amplitude to bring the pin to rupture (Fig. 4.10 b) and d)). Besides, D1 values in ECCS are half with the values originated by the constant amplitudes, the same happens in D2 except with constant imposed amplitude of 30mm.

The following table makes a comparison at the level of maximum values.

Tab. 4.5: Variation percentage of Force and Energy.

	F _{máx} (kN)	F _{mín} (kN)	ΔF (%)	E _{máx} (kNm)	E _{mín} (kNm)	ΔE (%)
ECCS	696.33 (D2)	300.33 (D1)	131.85	424.30 (D2)	155.64 (D1)	172.62
C20	389.16 (D1)	312.24 (D2)	24.63	330.33 (D1)	285.09 (D2)	15.87
C25	456.12 (D1)	345.45 (D2)	32.04	283.27 (D1)	183.19 (D2)	54.63
C30	580.62 (D2)	505.77 (D1)	14.80	293.86 (D1)	284.84 (D2)	3.17

4.3.2 StS+S355

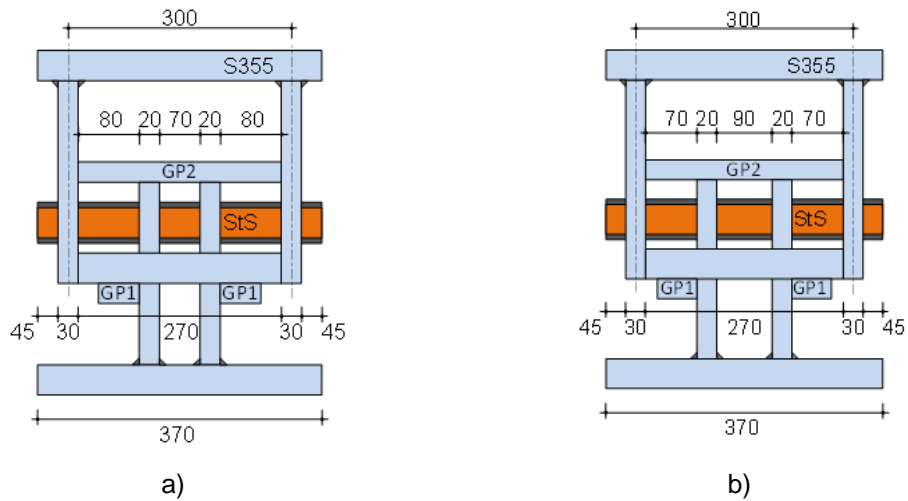
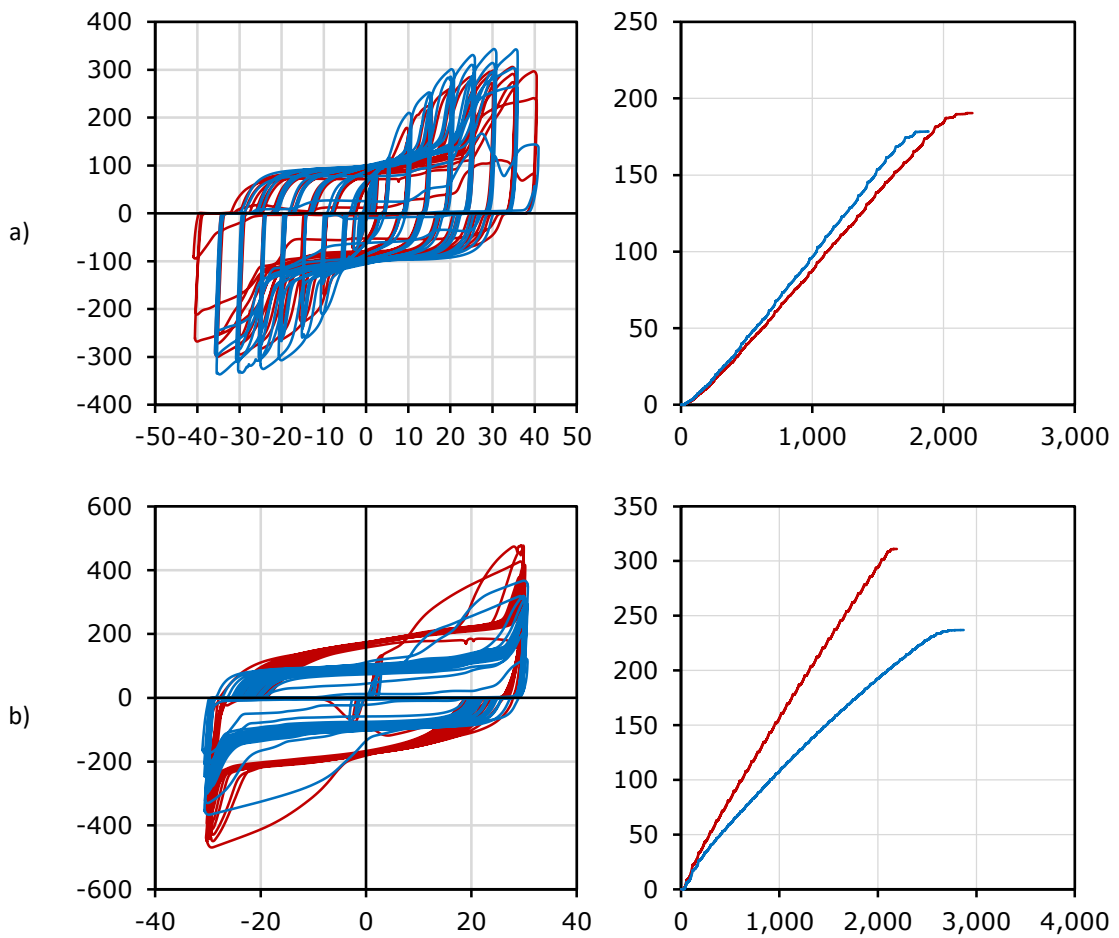


Fig. 4.11: Specimen StS_S355_D1 (a) and StS_S355_D2 (b)).

This subchapter will compare devices 09 with 23 (ECCS) (fig. 4.12 a)), 10 with 24 (C=30mm) (fig. 4.12 b)) and 11 with 25 (C=25mm) (fig. 4.12 c)). The overlapping graphs are shown in the following figure.



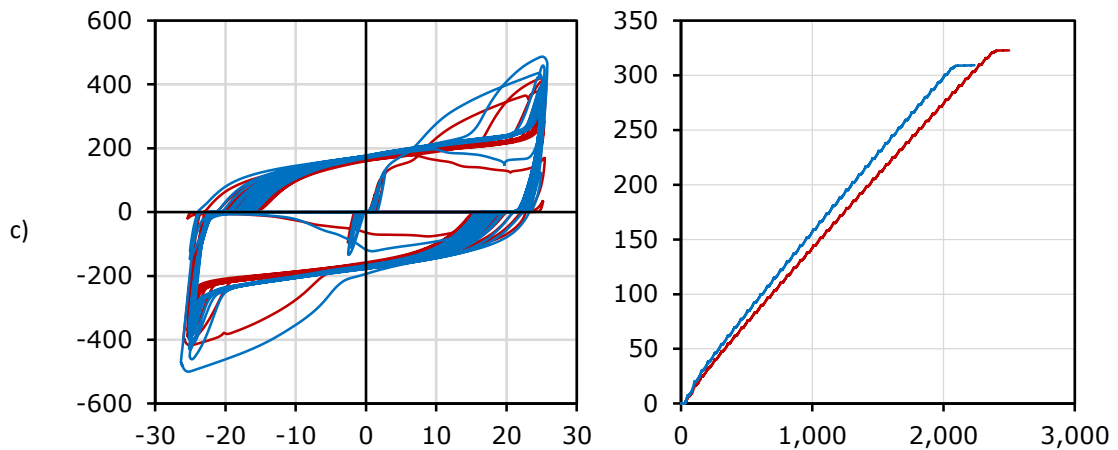


Fig. 4.12: Comparisons between StS_S355_D1 (red) with StS_S355_D2 (blue).

In this analysis D1 had lower results with imposed constant amplitude of 30mm, oppositely with 25mm and in similar ECCS with D2. Finally comparing the ECCS values with the constant amplitudes, at 25mm both were lower. At 30mm, D2 similar and D1 half.

The following table makes a comparison at the level of maximum values.

Tab. 4.6:4 Variation percentage of Force and Energy.

	Fmáx (kN)	Fmín (kN)	ΔF (%)	Emáx (kNm)	Emín (kNm)	ΔE (%)
ECCS	343.20 (D2)	305.88 (D1)	12.20	190.45 (D1)	178.51 (D2)	6.69
C25	500.04 (D2)	418.29 (D1)	19.54	321.10 (D1)	309.20 (D2)	3.85
C30	478.20 (D1)	366.78 (D2)	30.38	311.02 (D1)	236.96 (D2)	31.25

4.3.3 StS+HSS

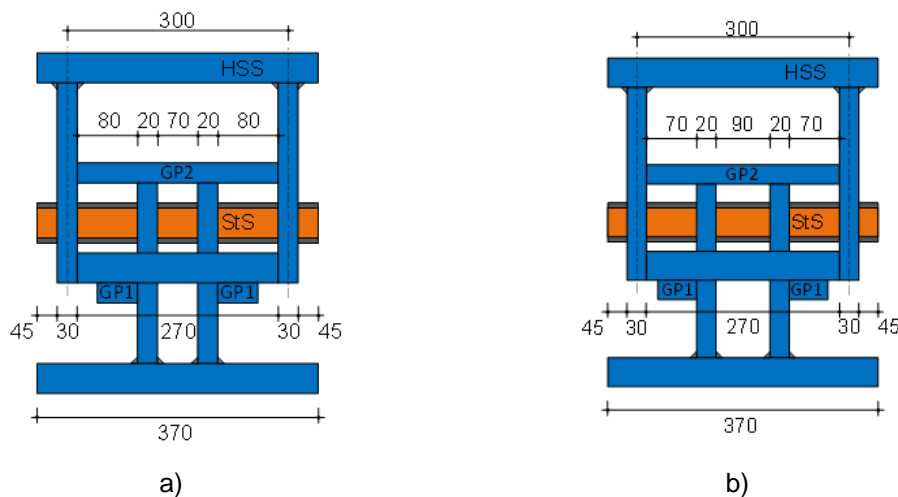


Fig. 4.13: Specimen StS_HSS_D1 (a) and StS_HSS_D2 (b).

This subchapter will compare devices 12 with 26 (ECCS) (fig. 4.14 a)), 13 with 27 (C=30mm) (fig. 4.14 b)) and 14 with 28 (C=25mm) (fig. 4.14 c)). The overlapping graphs are shown in the following figure.

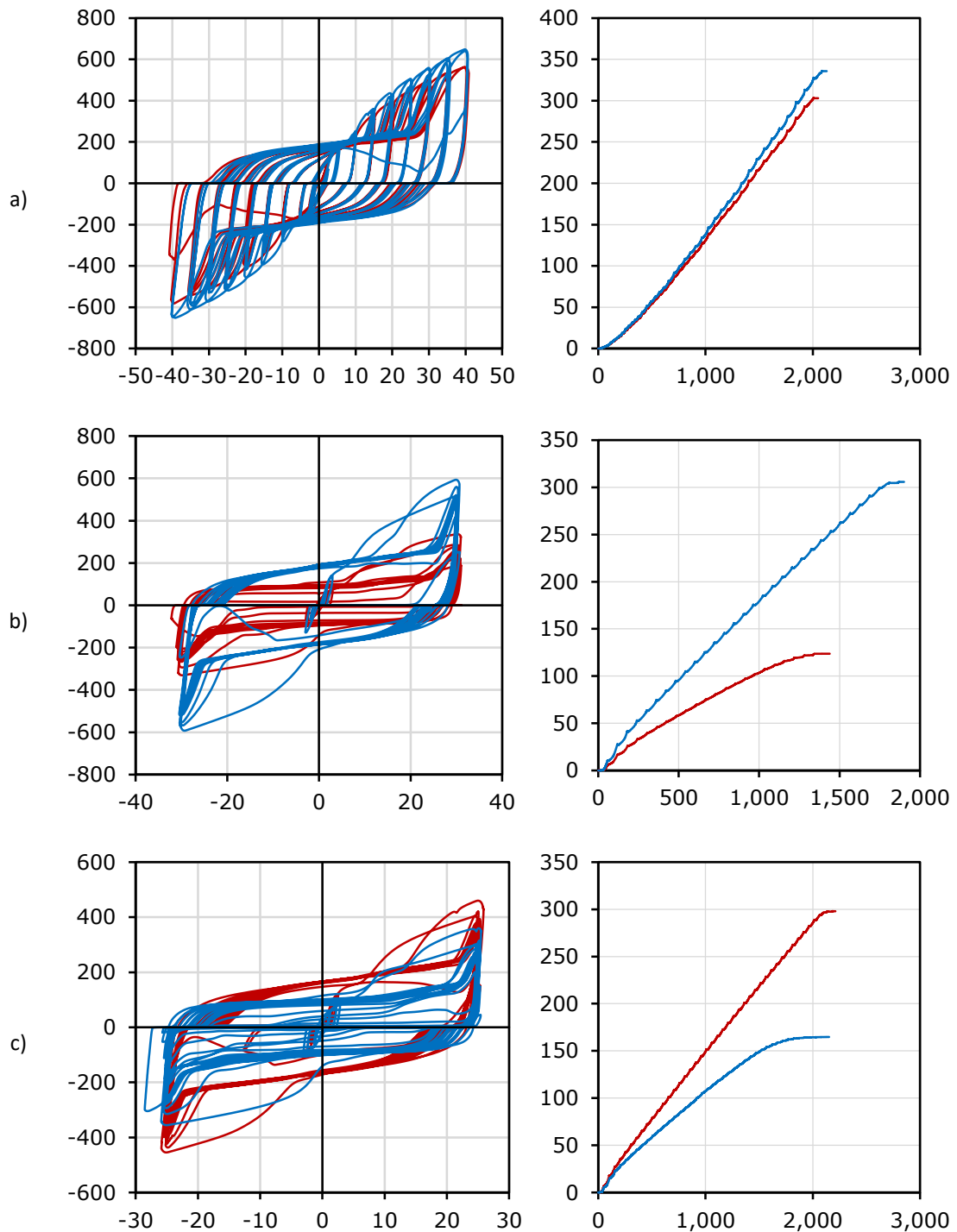


Fig. 4.14: Comparisons between StS_S355_D1 (red) with StS_S355_D2 (blue).

There were very similar tests with interesting ductility in D2 at the imposed constant amplitude of 30mm, which was not seen in the other tests. The ECCS values are slightly lower relative to the imposed constant amplitudes.

The following table makes a comparison at the level of maximum values.

Tab. 4.7: Variation percentage of Force and Energy.

	F _{máx} (kN)	F _{mín} (kN)	ΔF (%)	E _{máx} (kNm)	E _{mín} (kNm)	ΔE (%)
ECCS	651.33 (D2)	581.64 (D1)	11.98	335.76 (D2)	303.00 (D1)	10.81
C25	459.81 (D1)	359.52 (D2)	27.90	297.91 (D1)	164.74 (D2)	80.84
C30	593.40 (D1)	336.69 (D2)	76.25	305.72 (D2)	123.7 (D1)	147.15

5. Numerical Analysis

As mentioned in the literature review, the simulation of the specimens is done using the ABAQUS software. Continuing the work developed by Diogo Cabrita and Tiago Farinha there was no need to create a new device but to introduce the guide plates even though they are unnecessary for the software. The tests performed with ABAQUS did not detect any lateral displacement.

5.1 Calibration of the materials

The tested steels can be considered ductile, as they exhibit large inelastic stresses at orders of magnitude lower than Young's modulus. The input stress-strain values entered in the finite element models should be the "true" ones (ABAQUS, 2012), for example, the S235 steel has a standard yield strength of 235MPa, but in the tensile tests it shows a much higher stress as shown in table 5.1, and these are the "true" values. The value "235" is just for safety margin.

In this regard and according to the provisions of the Eurocode (EN 1993-1-5, 2006) the true stress, σ_t , and the true strain, ε_t , are obtained by expressions 3.1 and 3.2.

It should be noted that these expressions are only valid in the plastic range up to the ultimate tensile strength point, since after this point the stress and strain are no longer distributed by equal cross section because of the neck phenomenon (Soboyevo, 2002). Modeling of plastic hardening for cyclic steel components is done by considering the theoretical combination of hardening present in ABAQUS, based on the formulations developed by Armstrong-Frederick and Chaboche (Myers et al., 2009 - Appendix D). The isotropic hardening component σ^0 is defined by the instantaneous size of the yield surface derived from the following expression, ABAQUS, the calculation model for actions, predicts material behaviour, and defines plasticity:

$$\sigma^0 = f_y + Q_\infty \times (1 - e^{-b \times \bar{\varepsilon}^p}) \quad (5.1)$$

Where,

f_y : initial yield surface size.

$\bar{\varepsilon}^p$: equivalent plastic strain.

Q_∞ and b : isotropic hardening parameters.

Whereas the evolution of the non-linear kinematic hardening component is derived from the expression:

$$\bar{\alpha}_i = C \times \bar{\varepsilon}^p \times \frac{1}{f_y} \times (\bar{\sigma} - \bar{\alpha}) - \gamma \times \bar{\alpha} \times \bar{\varepsilon}^p + \bar{\alpha}_{i-1} \quad (5.2)$$

Where,

C and γ : kinematic hardening parameters.

$\bar{\alpha}$: equivalent back stress.

$\bar{\sigma}$: equivalent stress or Von Mises stress.

Finally, the nonlinear combined isotropic and kinematic stress tensor, in the case of a tensile load test, is given by:

$$\bar{\sigma} = f_y + \bar{\alpha} \tag{5.3}$$

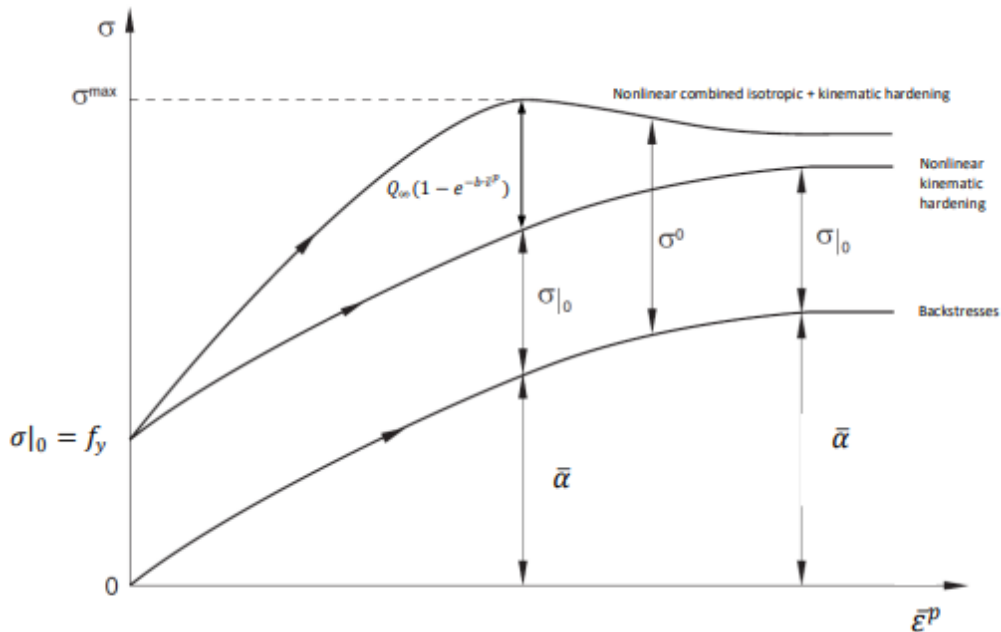


Fig. 5.1: Evolution of isotropic and kinematic hardening for combined hardening model under uniaxial stress state (adapted from ABAQUS, 2012).

These parameters are developed preliminarily in a curve fitting process, where the expressions are applied analytically and against the true stress-strain curve obtained in the tensile tests shown in figure 3.25.

Finally, isotropic hardening was not considered because it does not capture the Bauschinger effect (figure 5.2), where a hardening in tension will lead to softening in subsequent compression, whereas kinematic hardening does (Kelly, 2013). As also tensile test is only pulling the steel, isotropic parameters are not considered because don't test the steel in cycles.

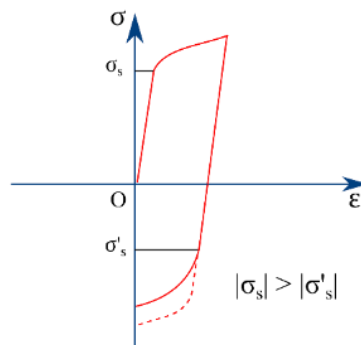


Fig. 5.2: Representation of the Bauschinger Effect (Stahleisen & Hoff, 1958).

The kinematic hardening considers the Bauschinger effects and states that the yield surface remains the same shape and size but merely translates in stress space. Refers to the property, where materials stress and strain changes as a result of the microscopic stress distribution of the material. For example, the increase of tensile yield strength can occur at the expense of compressive yield strength.

Only interpolated these values, nonlinear kinematic hardening, because these two could get good curves was well as, the more information input in ABAQUS, even more likely the simulation aborted.

Thus, the values that characterize the materials under study to put into ABAQUS are as follows:

Tab 5.1: Combined hardening parameters

Materials	σ^0, f_y (MPa)	C	γ	Q_∞	b
S235 (pin)	355	4400	19,0	0	
StS (pin)	394	3250	5,0		
S355 (plate)	400	2400	9,6		
HSS (plate)	494	3600	12,0		

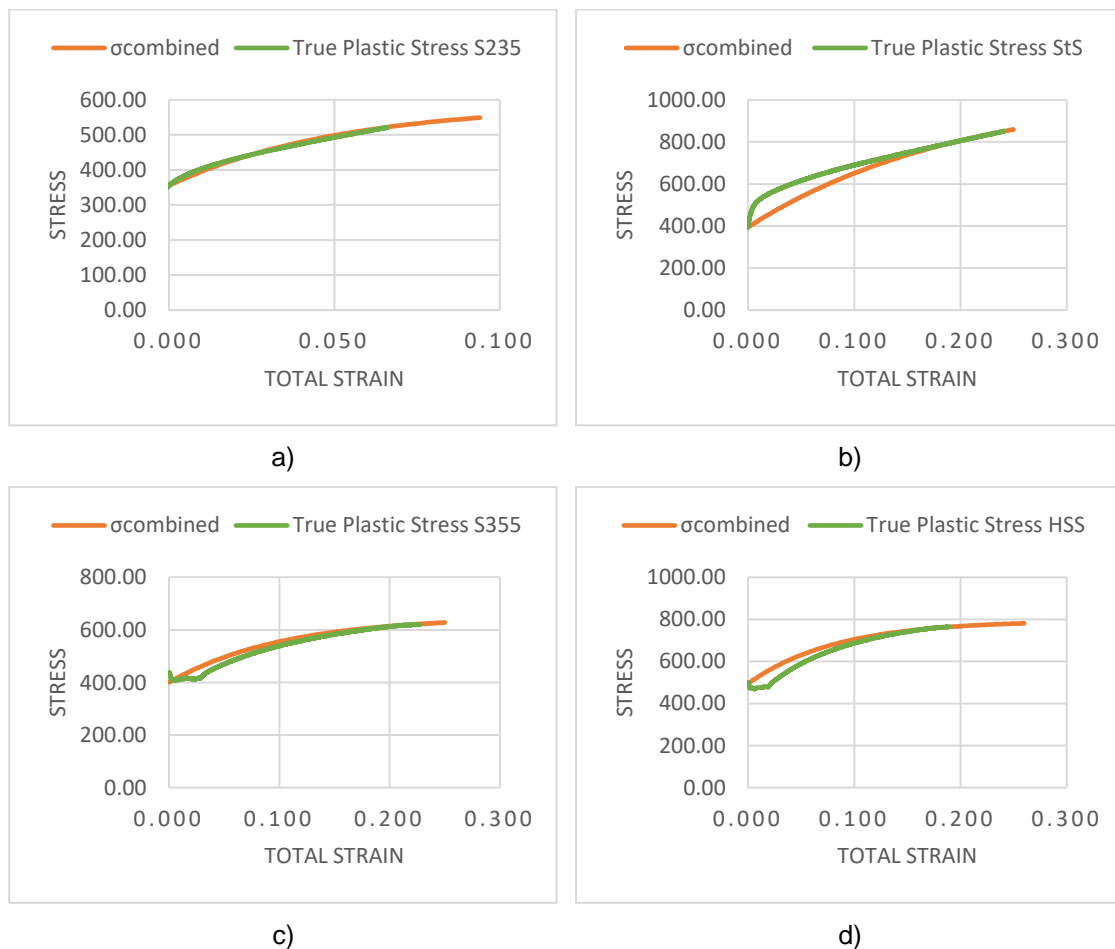


Fig. 5.3: Plastic range calibration: (a) pin S235, (b) pin StS, (c) plate S355 and (d) plate HSS.

5.2 Damage criteria: Ductile damage

When modeling steel, the most common type of failure is ductile, except under certain conditions, such as low temperatures, that it can be brittle. Ductile damage can be seen as the appearance of microscopic voids, which during plastic deformation tend to grow and coalesce. This phenomenon creates large, localized deformations that lead to failure. This physicist has been studied thoroughly and, in recent years, numerical models have been developed to simulate this behaviour using microscope images of real specimens being tested with various load cases (Bandstra et al, 2004). This failure mechanism manifests itself in yield stress softening and elastic stiffness degradation (Figure 5.4) and is defined using a damage initiation criterion and a damage evolution law.

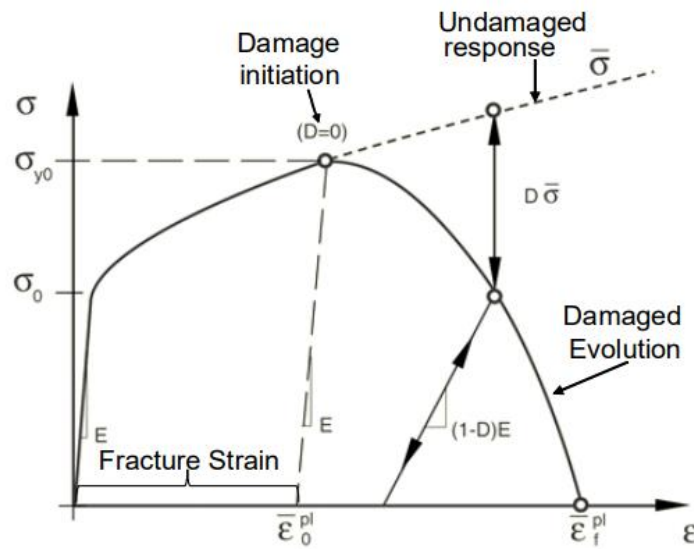


Fig. 5.4: Stress-strain curve with progressive damage degradation (Cabrita, 2020).

The fracture strain is the total sum of the plastic deformation that an element withstands.

When using ABAQUS, the modelling of damage is divided into two steps, the damage initiation criteria ($D=0$) and the damage evolution ($D=1$) (DASSAULT, 2014), observed during the tests by the stress levels. The damage initiation criteria are defined by the fracture strain value, which corresponds to the plastic strain equivalent to the true plastic strain at damage initiation, $\bar{\epsilon}_0^{pl}$. The fracture strain is related to the strain at the onset of damage, which corresponds to the ultimate strain, $\sigma_{y0} = \sigma_u$. Once the damage onset criterion is reached, the stress tensor in the material follows the damage evolution law, resulting in an increasing loss of element stiffness and can be adjusted to remove the element from the mesh when the failure point is reached.

$$\sigma = (1 - D) \times \bar{\sigma} \quad (5.4)$$

Where,

D is the damage parameter.

$\bar{\sigma}$ is the undamaged stress tensor.

The damage evolution can be defined in various forms, in the present study it is specified in terms of fracture energy G_f (Hillerborg, 1978). The fracture energy is obtained through the expression (5.5).

$$G_f = \int_{\bar{\varepsilon}_0^{pl}}^{\bar{\varepsilon}_f^{pl}} L \times \sigma \, d\bar{\varepsilon}^{pl} = \int_0^{\bar{u}_f^{pl}} \sigma \, d\bar{u}^{pl} \quad (5.5)$$

Where,

L is the characteristic length of the element determined by the cube root of the volume of the initial geometry.

This variable is introduced in the formulation to reduce the mesh dependence, that way the stress-strain relationship no longer accurately represents the behaviour of the material and instead of defining the strain after the onset of damage as plastic deformation, it is defined as an equivalent plastic displacement. (Levanger, 2012). In this case, the energy dissipated during the damage process is specified per area unit, not per volume unit. Since the pin is the only element that breaks it is only to it that this damage criterion applies. These values are based on previous simulations.

Tab. 5.2: Damage parameters for the tensile tests.

Materials (pins)	Fracture Strain	Fracture Energy (N/mm)
S235 (Cabrita, 2020)	0.11	6800
StS (Al-Khazraji et al., 2017)	0.22	

The following simulations show the differences in the results with and without damage criteria, where the difference in values from one to the other will be visible. Without the damage criteria the pin just plasticizes and thus throughout the loading history will continue to resist high forces within the test range. The tests tested for this were one with an ECCS load history (figure 5.5 and 5.6) where the loss of strength of the StS pin is observed each time the amplitude is increased until failure. The other test has a load history with constant imposed amplitudes (figure 5.7 and 5.8), and it is observed that the stiffening of the S235 pin decreases until then to its rupture. The stiffening is the straight lines "parallel" to the abscissa axis.

Finally, it is important to say that the failure of the pins was the equivalent to the experimental tests, which was by shear (figure 5.9).

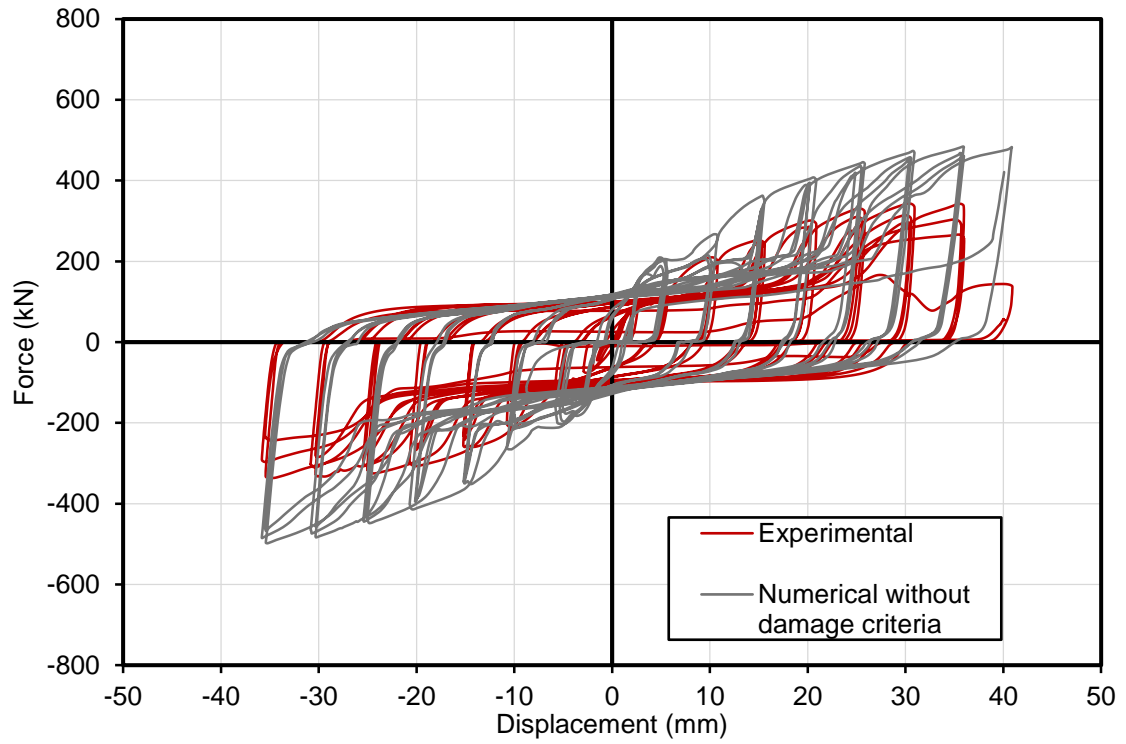


Fig. 5.5: Force-Displacement Curve of the simulation without damage criteria over the experimental one (Box 23: R_StS_S355_D2_E).

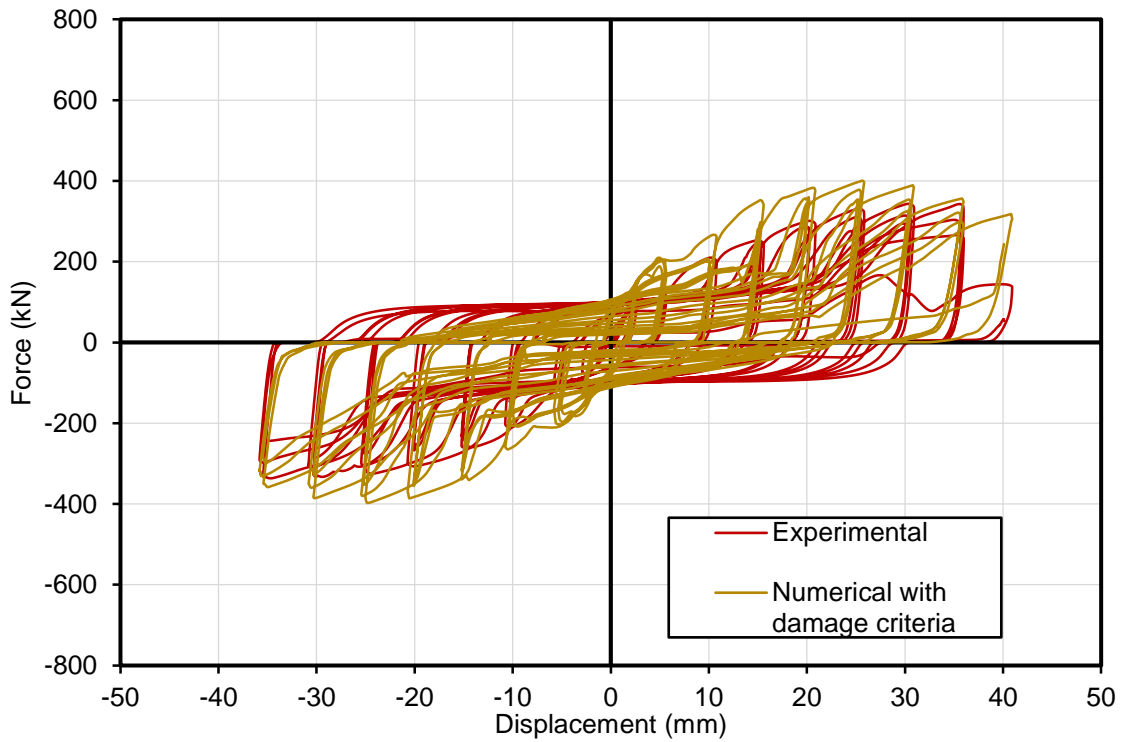


Fig. 5.6: Force-Displacement Curve of the simulation with damage criteria over the experimental one (Box 23: R_StS_S355_D2_E).

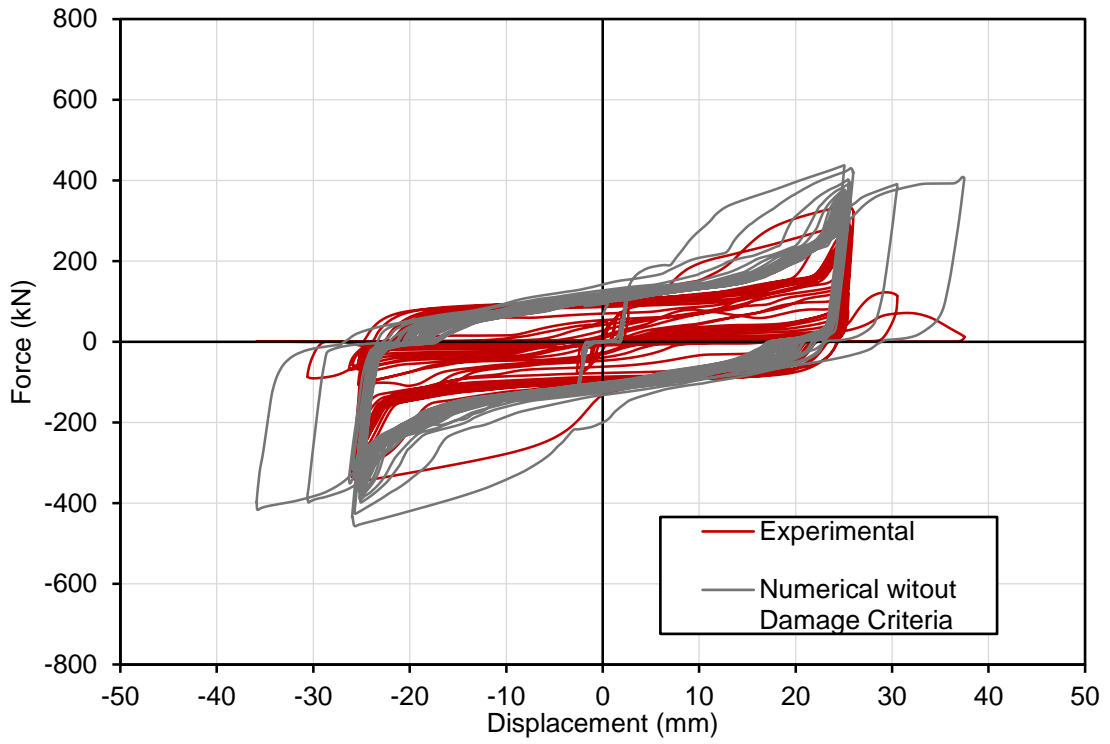


Fig. 5.7: Force-Displacement Curve of the simulation without damage criteria over the experimental one (Box 22: R_S235_HSS_D2_C3).

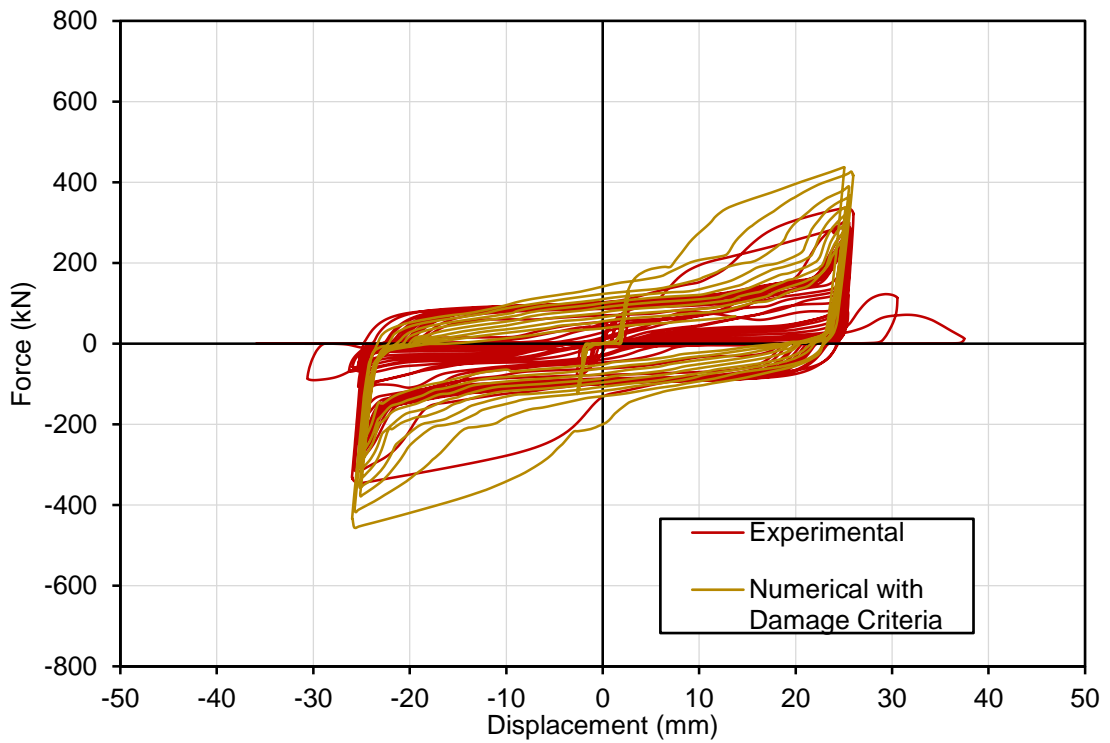
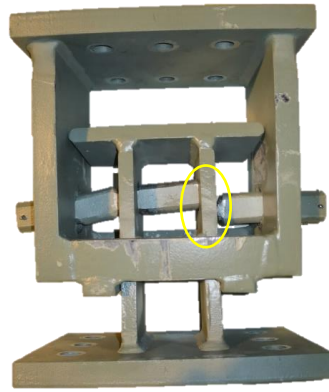


Fig. 5.8: Force-Displacement Curve of the simulation with damage criteria over the experimental one (Box 22: R_S235_HSS_D2_C3).

a)



b)

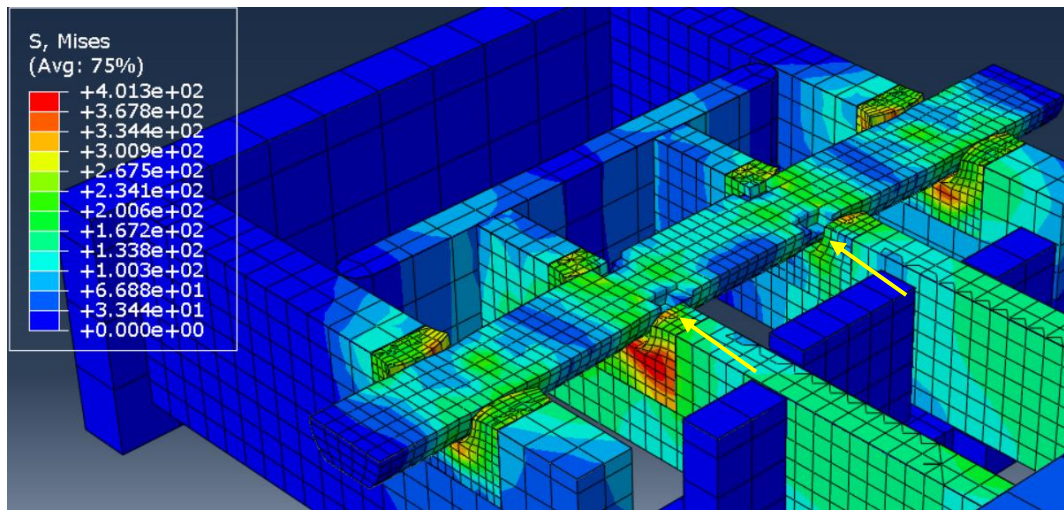


Fig. 5.9: StS pin failure: experimental (a) and numerical (b).

But there were simulations that the pin damage did not match those obtained in the lab. As it was also not expected that certain pins would break by shear effect and in a random way, i.e., it was not only in a specific feature/configuration. In these cases, ABAQUS gives coherent and not random results, which shows that it is more coherent for the pin to break by cutting. The advantage of this type of breakage is that the pin when breaking is still able to hold longer (ductility), as is the case of case 22 (fig. 5.7). The following figure shows the breakage tendency of the StS pin of case 14 (HSS).

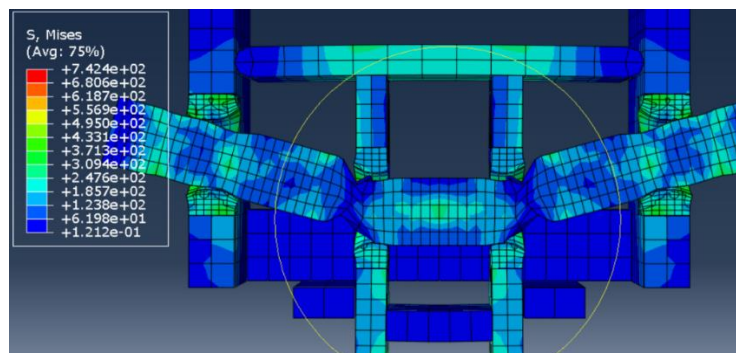


Fig. 5.10: Rupture trend of the StS pin numerically.

However, there were cases where without the damage criteria interesting results were obtained (fig. 5.10).

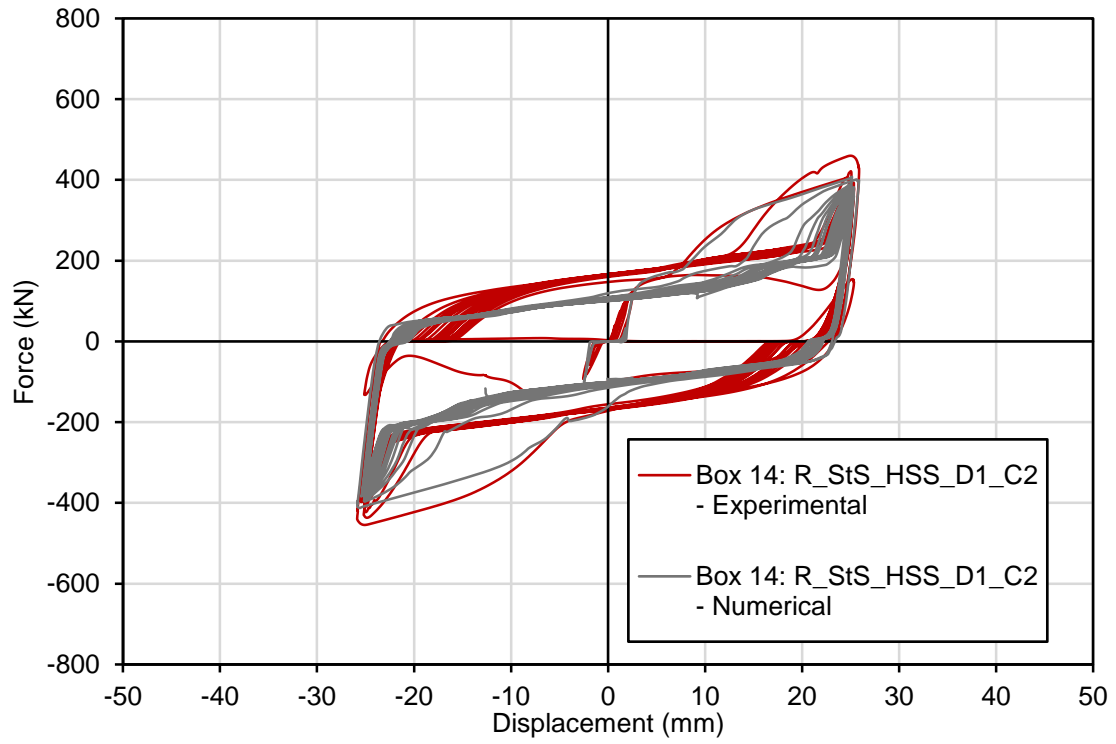


Fig. 5.11: Force-Displacement Curve of the simulation without damage criteria over the experimental.

6. Reusable boxes

Not being part of the DISSIPABLE project, 4 boxes were reused to understand the behaviour during and after a second test.

The choice of the 4 boxes was solely due to the final state of the first tests, measuring the ovalizations suffered by the respective pin. This measurement was made using a digital ruler and a ring pliers. The following figures shows an example of the measurement made in the laboratory. The rest of the measurements are present in the report DISSIPABLE, 2021.

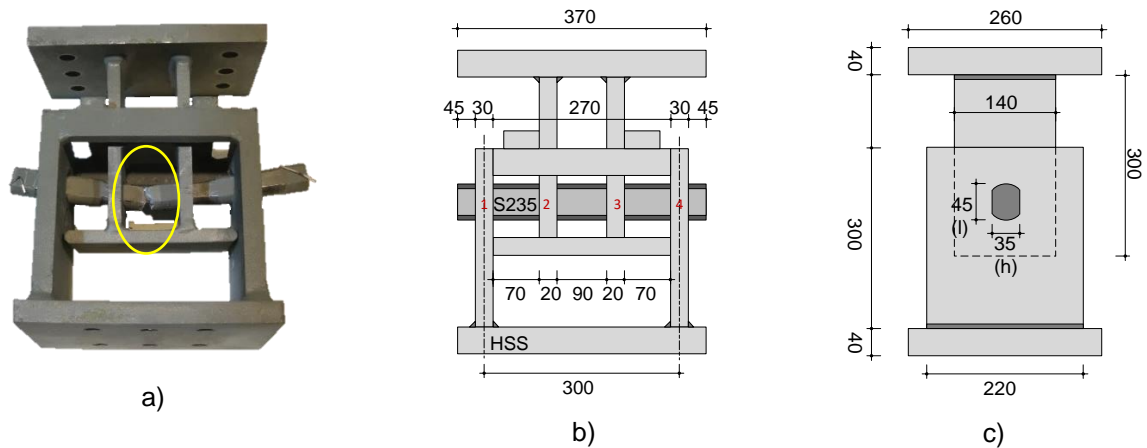


Fig. 6.1: Failure mode of test number 19 (a) and numeration of the plates to evaluate de ovalization (b) & (c).

Tab. 6.1: Ovalization of the plates HSS and the pin S235 of the box 19.

	1		2		3		4	
Box	External (mm)	Internal (mm)	External (mm)	Internal (mm)	Internal (mm)	External (mm)	Internal (mm)	External (mm)
HSS	l=53.19 h=37.20	l=61.29 h=35.46	l=55.05 h=36.46	l=48.94 h=37.44	l=49.23 h=37.52	l=55.53 h=35.74	l=58.75 h=36.10	l=53.26 h=36.60
Pin S235	l=42.02 h=35.54		l=35.64 h=31.37		l=34.18 h=30.84		l=40.36 h=35.63	

Note: Internal means ovalization of the side facing the center of the box while external is the opposite.



Fig. 6.2: (a) pin elongation (b) box ovalization.

Thus, the boxes chosen are those written in red in Table 3.1. By chance, or not, the 4 cases with smaller ovalizations are one from each category, i.e., material (S355 and HSS) and distance between inner plates (D1 and D2). It should be noted that the failure of the pins, in the 1st test, in the HSS cases was by bending while in the S355 cases it was by shear.

For these tests it was necessary to fabricate 4 pins. These pins were made at LERM with steel type like S235. These pins were the ones used in the 1st phase of this project and here is designated as S235*, as explained in chapter 3.

6.1 Test 19: R_S235_HSS_D2_E vs Test 20R: R_S235*_HSS_D2_E

As the pins used in this part of laboratory testing are all S235 type pins, the most reliable comparison is to compare with cases that have previously been tested with pins of this same category. Therefore, the comparison with the other tests is not very conclusive because in the first use they were tested with a StS type steel pin, which has different characteristics than the S235 (table 3.5).

The following figures show the comparison between Test 19 and Test 20R.

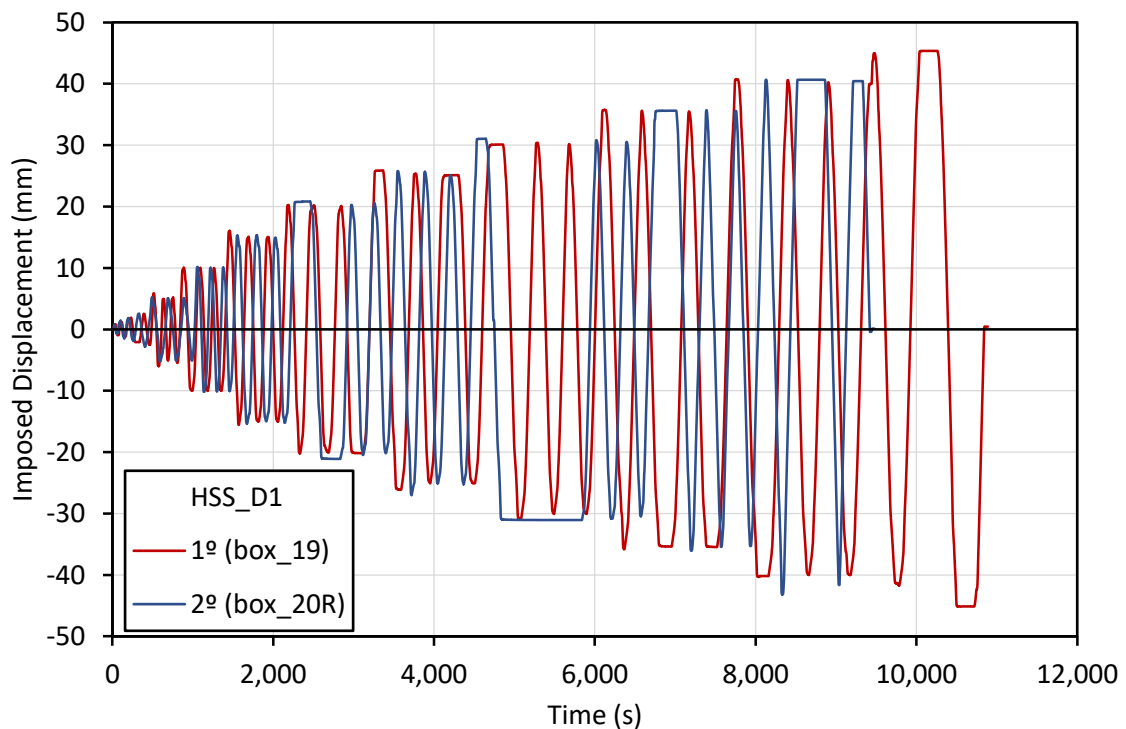


Fig. 6.3: Load history for test number 19 and 20R.

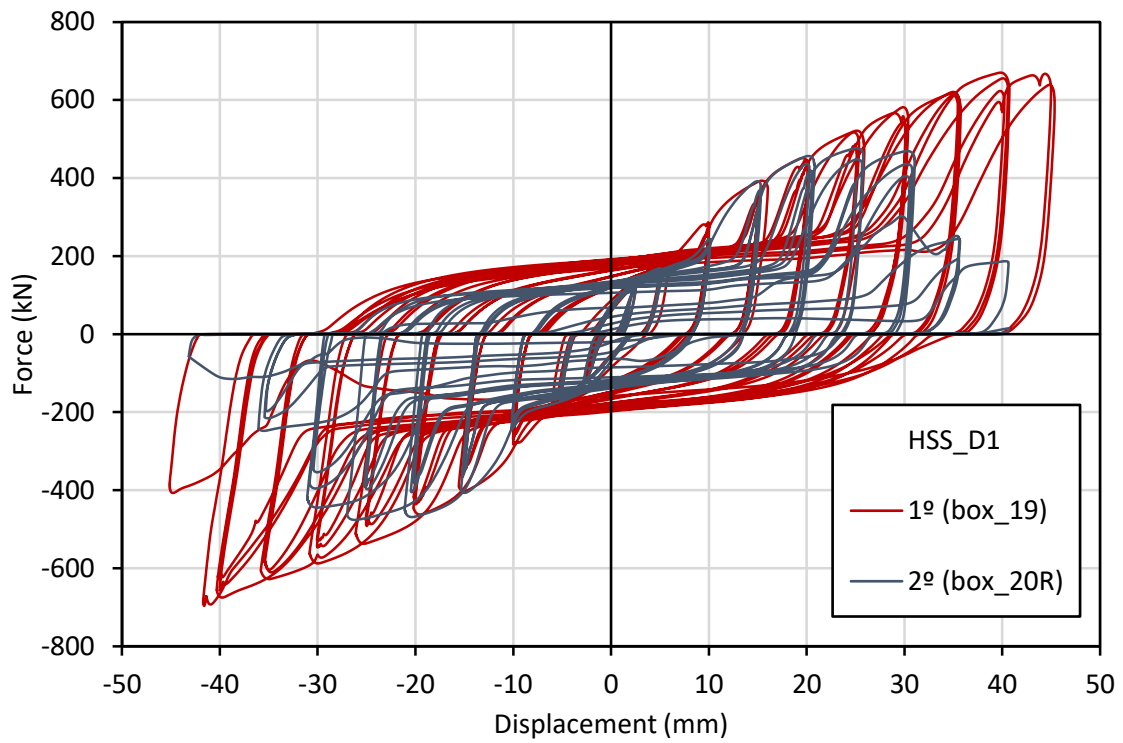


Fig. 6.4: Force-Displacement curve of test number 19 and 20R.

The next figures show how the failure occurred in the pin.

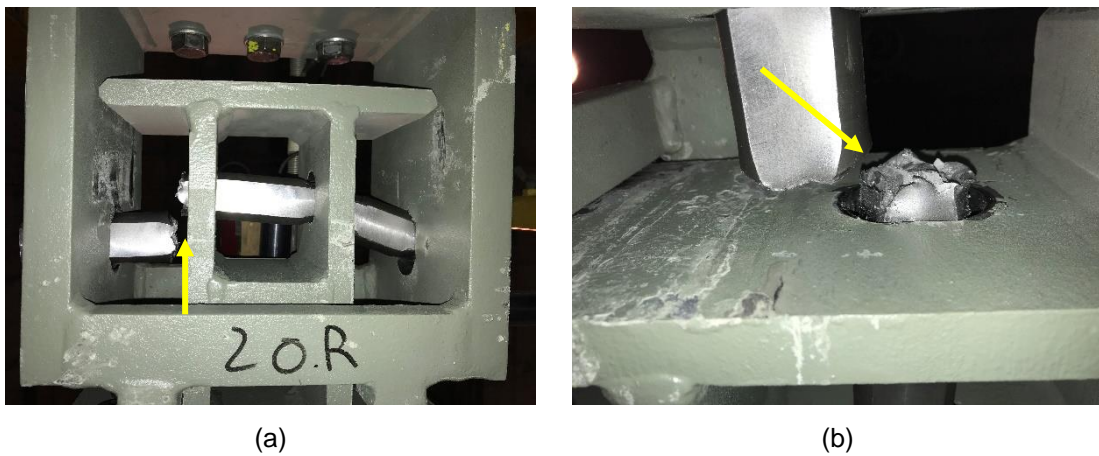


Fig. 6.5: Experimental test number 20R: (a) failure mode; (b) pin failure.

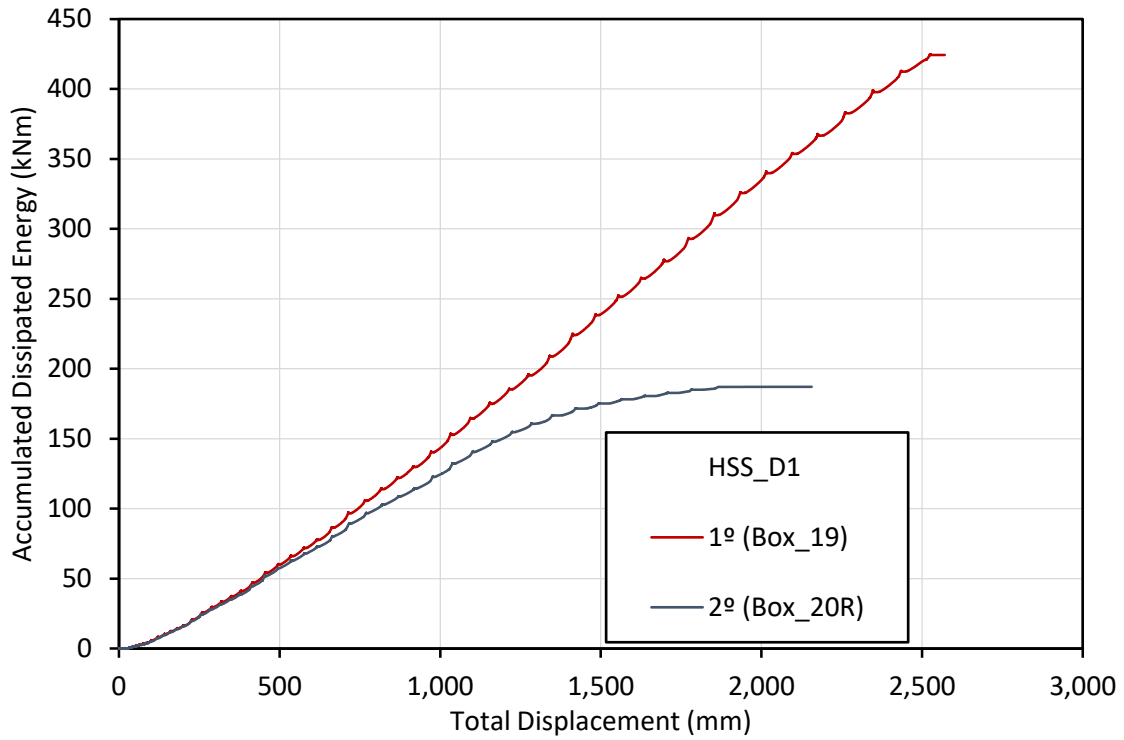


Fig. 6.6: Accumulated Dissipated Energy curve of test number 19 and 20R.

By this analysis the conclusions are as expected, i.e., reused box having a smaller number of cycles, less hardening and less accumulated dissipated energy. The strength reached similar values to the box of the 1st test up to the initial imposed displacement group.

As the reused boxes were already somewhat ovalized, this causes the forces reached to be recorded more by peaks, and always constant at the quantitative force level when increasing the imposed displacements, and not by a constant increasing "straight line" as in the tests of the new boxes, as shown in the next figure with the separate force-displacement curves. This shows that there is less resistance on the part of the box because the pins at mainly the initial imposed displacements meet the plates in a lighter way and also explains the lower hardening.

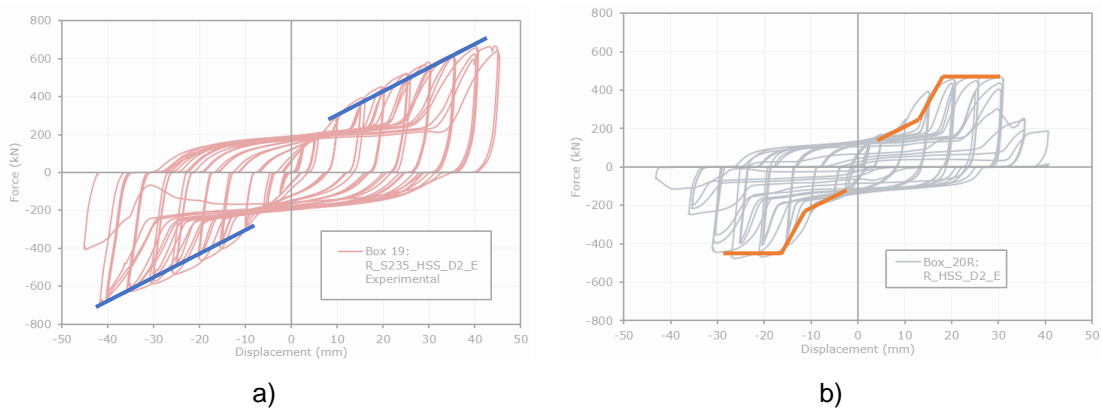


Fig. 6.7: Force-Displacement curve of test number 19 (a) and 20R (b), with the progress of the force.

In the next subchapters it should be noted that the graphs that follow have no units due to the single fact of visualization. Therefore, the Force-Displacement graphs (left) on the abscissae are the displacements in mm and on the ordinates are the forces in kN, while the Accumulated Dissipated Energy graphs (right) on the abscissae are the total displacement, i.e., the sum of the imposed amplitudes, and the ordinates are then the energy.

6.2 D1vsD2 with reused boxes

This subchapter will compare devices 11R with 25R (S355) (fig. 6.9 a)) and 13R with 20R (HSS) (fig. 6.9 b)). The overlapping graphs are shown in the following figure.

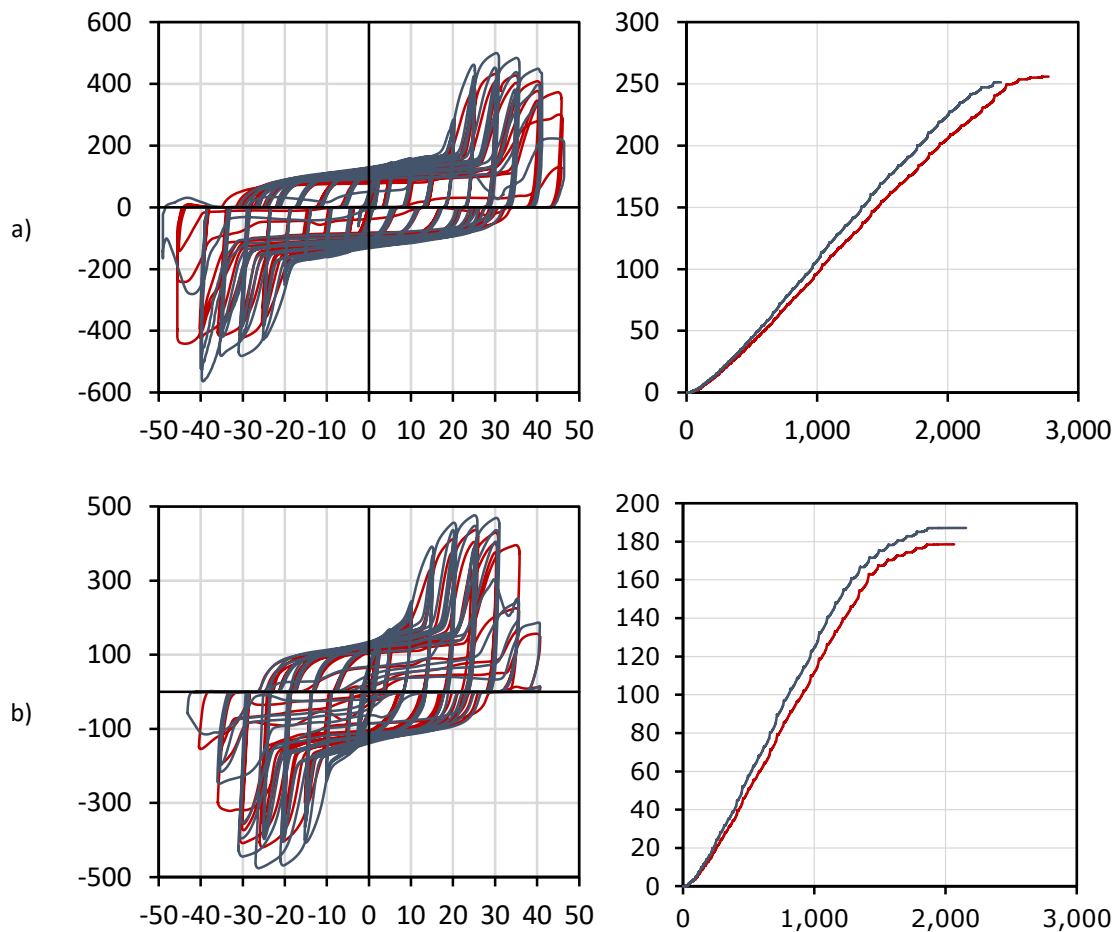


Fig. 6.8: Comparisons between S235*_D1 (red) with S235*_D2 (dark blue). Very similar graphs, with higher resistances with D1 remoteness.

6.3 S355vsHSS with reused boxes

This subchapter will compare devices 11R with 13R (D1) (fig. 6.10 a)) and 20R with 25R (D2) (fig. 6.10 b)). The overlapping graphs are shown in the following figure.

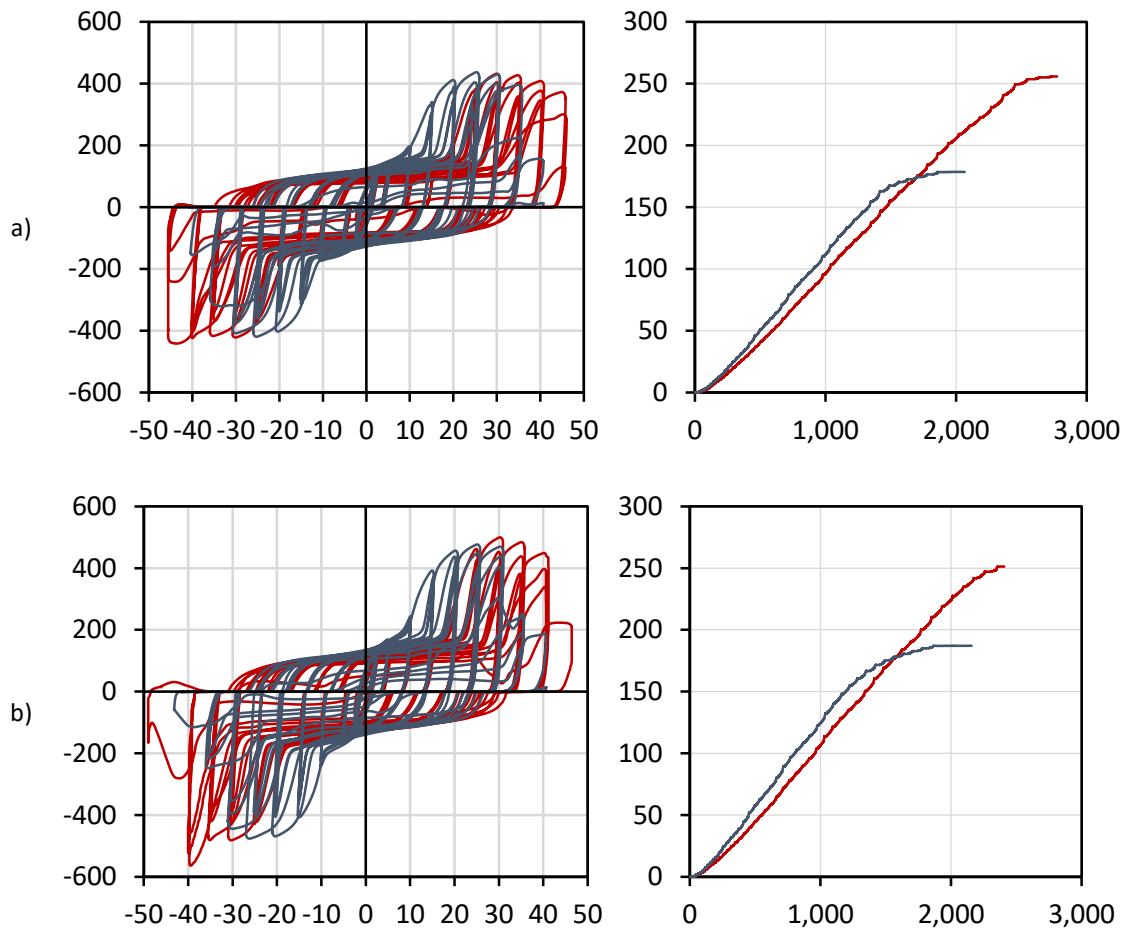


Fig. 6.9: Comparisons between S235*_S355 (red) with S235*_HSS (dark blue).

Where it was proven that as the S355 has less resistant steel and thus larger ovalization. This is explicit in the F-D graphs, where it only offers strength from the 25mm range onwards, while HSS is from 15mm onwards. It thus demonstrates greater ductility, which was to be expected.

7. Conclusions and future developments

7.1 Conclusions

This dissertation does not conclude which is the perfect combination to dissipate energy from seismic actions. Moreover, a real earthquake was not simulated since this is characterized by strong and sudden movements, and in the laboratory the movements were the opposite, i.e., smooth and low speed/acceleration to understand in detail the hysteretic behaviour of the various DRBrC configurations tested. However, all tests were successfully performed without any measurement problems because the mechanical jack (actuator) was correctly mounted.

From the results presented, in fact, the HSS boxes were those which presented both higher and lower values of force, number of cycles and accumulated dissipated energy, as mentioned in sub-chapter 3.6. By coincidence (fig. 7.1) the devices that had these effects were the ECCS of the S235_HSS devices and their imposed constant amplitudes C1 (20mm). As it was also the case of the StS_HSS devices with constant imposed amplitudes C1 (30mm). The results for boxes 6 and 27 are presented in Figure 7.1.

Full list of experimental test specimens

No of test configuration	Configuration code (*)	Pin shape	Pin Ø	Pin steel	External plate thickness	External plate dimensions	Internal Plate spacing	Internal plate thickness	External plate dimensions	Plates steel	Load protocol
1	R_S235_S355_D1_E	R	50	S235	30	220x300	D1	20	140x300	S355	E
2	R_S235_S355_D1_C1	R	50	S235	30	220x300	D1	20	140x300	S355	C1
3	R_S235_S355_D1_C2	R	50	S235	30	220x300	D1	20	140x300	S355	C2
4	R_S235_S355_D1_C3	R	50	S235	30	220x300	D1	20	140x300	S355	C3
5	R_S235_HSS_D1_E	R	45	S235	30	220x300	D1	20	140x300	HSS	E
6	R_S235_HSS_D1_C1	R	45	S235	30	220x300	D1	20	140x300	HSS	C1
7	R_S235_HSS_D1_C2	R	45	S235	30	220x300	D1	20	140x300	HSS	C2
8	R_S235_HSS_D1_C3	R	45	S235	30	220x300	D1	20	140x300	HSS	C3
9	R_S45_S355_D1_E	R	45	S45	30	220x300	D1	20	140x300	S355	E
10	R_S45_S355_D1_C1	R	45	S45	30	220x300	D1	20	140x300	S355	C1
11	R_S45_S355_D1_C2	R	45	S45	30	220x300	D1	20	140x300	S355	C2
12	R_S45_HSS_D1_E	R	45	S45	30	220x300	D1	20	140x300	HSS	E
13	R_S45_HSS_D1_C1	R	45	S45	30	220x300	D1	20	140x300	HSS	C1
14	R_S45_HSS_D1_C2	R	45	S45	30	220x300	D1	20	140x300	HSS	C2
15	R_S235_S355_D2_E	R	50	S235	30	220x300	D2	20	140x300	S355	E
16	R_S235_S355_D2_C1	R	50	S235	30	220x300	D2	20	140x300	S355	C1
17	R_S235_S355_D2_C2	R	50	S235	30	220x300	D2	20	140x300	S355	C2
18	R_S235_S355_D2_C3	R	50	S235	30	220x300	D2	20	140x300	S355	C3
19	R_S235_HSS_D2_E	R	45	S235	30	220x300	D2	20	140x300	HSS	E
20	R_S235_HSS_D2_C1	R	45	S235	30	220x300	D2	20	140x300	HSS	C1
21	R_S235_HSS_D2_C2	R	45	S235	30	220x300	D2	20	140x300	HSS	C2
22	R_S235_HSS_D2_C3	R	45	S235	30	220x300	D2	20	140x300	HSS	C3
23	R_S45_S355_D2_E	R	45	S45	30	220x300	D2	20	140x300	S355	E
24	R_S45_S355_D2_C1	R	45	S45	30	220x300	D2	20	140x300	S355	C1
25	R_S45_S355_D2_C2	R	45	S45	30	220x300	D2	20	140x300	S355	C2
26	R_S45_HSS_D2_E	R	45	S45	30	220x300	D2	20	140x300	HSS	E
27	R_S45_HSS_D2_C1	R	45	S45	30	220x300	D2	20	140x300	HSS	C1
28	R_S45_HSS_D2_C2	R	45	S45	30	220x300	D2	20	140x300	HSS	C2
	R										

Dimensions in mm and steel grades in MPa
 (*) Configuration code according to: #PinShape_#PinGzelGrade_#PlatesSteelGrade_#InternalPlateSpacing_#LoadProtocol

Color codes			
Protocol	Pin section	Steel grade	Internal plate spacing
E = ECCS	R = Chamfered	S235	D1 = 80/0/00
C1 = Constant 1	C = Circular	S45	D2 = 70/90/70
C2 = Constant 2		S355	
C3 = Constant 3		HSS	

Fig 7.1: Devices with higher and lower values.

At parametric level having 20 devices in which half have D1 and half D2, there was no distance that stood out the other. Such is the case when comparing the pins steel type, where there are 12 StS and the rest S235, none of them was "better" than the other. Geographically, the countries and areas more prone to earthquakes are coastal areas, such as Portugal, Japan, Italy, USA, Mexico, Greece, among others and therefore possibly the StS pin is the most recommended,

which also has tensile strength to be higher than the S235 pin. Regarding the boxes those show different values, being 14 HSS boxes and 6 S355 that on the parametric analysis, reflects more points in favor of the less resistant box that ovalizes more but makes the pin, the essential element to capture the energy released from the earthquake, more ductile.

Another important result to stress out is the fact that 1/3 of the tests had failure mode via shear and not by bending as would have been expected. This failure is not favourable for pin replacement, which is one of the major projects aims on the economic level. That means, to find a device that resists well to a seismic event and is not damaged too much to reuse in a future earthquake, but to be replaced with a new pin. This failure mode did not happen in a specific type of pin, type of box or distance between interior plates in which one could conclude that this event is due to a combination of several characteristics. However, with the same number of devices, more such failures occurred in D2 than in D1.

ABAQUS is not stochastic but deterministic, and so the pin results were always presented with shear failure due to the imposed settings. While in the lab the ruptures happened somewhat randomly, ABAQUS does not provide such results, but these are nonetheless coherent. Otherwise, the simulations showed similar values with the real ones. Pinching phenomena were not fully captured by the numerical models. Convergence of the finite element solution was not the focus, so the models presented still have room for improvement regarding their efficiency; mesh discretization (refinement) and material properties can be further improved considering that the isotropic hardening component was not applied. A combined hardening characterization could not be performed accurately because cyclic tensile tests to characterize the cyclic behavior of the steel materials were not possible. However, the numerical models developed allowed further evaluation.

Finally, 4 new tests were performed, in the laboratory, on reused boxes with pins manufactured in LERM's workshops with characteristics like an S235. A priori it would be expected that the reused boxes would be HSS because they resist more and therefore deform less. Eventually there were 2 HSS boxes and 2 S355 boxes, which leads to the conclusion that the S355 boxes do not deform much more than the HSS ones, and therefore are also a great final solution. The results of these tests show that the boxes are much less effective the second time they are used.

7.2 Future developments

As mentioned before, the modeling of the devices using ABAQUS can be much improved namely in the material properties, because in these simulations they were approximate and generalist values, as also the meshing, especially at the pin, and in the material damage characterization.

In practice tests are taking place on a seismic table at the National Technical University of Athens (NTUA), tests that more closely simulate a seismic action for later this type of dissipative solution to be integrated in EC8, being necessary to develop design rules and behaviour coefficients (q).

References:

- ABAQUS (2012) Analysis User's Manual, Version 6.12. Providence, RI: Dassault Systèmes.
- Adams, G. G. & Nosonovsky, M. 2000. Contact modeling - forces. *Tribology International*, Vol. 33, pp 431- 442.
- Al-Khazraji A. N., Amin S. A. & Al-Warmizyari H. A.,
Creep Damage Modeling for Stainless Steel Tube Type 321H Using Finite Element Analysis,
Mechanical Engineering Department, University of Technology, Baghdad, Iraq, 2017.
- Bandstra, J. P., Koss, D. A., Geltmacher, A., Matic, P. & Everett, R. K. 2004. Modeling void coalescence during ductile fracture of a steel. *Materials Science and Engineering*, Vol. 366, pp 269-281.
- Barber, J. R. & Ciavarella, M. 2000. Contact mechanics. *International Journal of Solids and Structures*, Vol. 37, pp 29-43.
- Cabrita, D., 2020. Experimental and numerical research on a novel hysteretic dissipative and easily repairable device for composite steel-concrete frame structures. MSc Dissertation in Civil Engineering, Instituto Superior Técnico.
- Calado L., Ferreira J., S. F. (2004) Characterization of Dissipative Connections for Concentric Bracing Systems in Steel Frames in Seismic Areas: Report 2 - Detailed Report INERD.
- Chopra A.K., 2001. *Dynamics of Structures, Theory and Applications to Earthquake Engineering*. Second Edition, New Jersey: Prentice-Hall.
- Construir, *Estará a nossa construção preparada em caso de sismo?*, 2018
<https://www.construir.pt/2018/01/15/estara-nossa-construcao-preparada-caso-sismo>
- DASSAULT 2014. ABAQUS Analysis User's Guide. Version 6.14. France: Dassault Systèmes Simulia Corporation.
- DISSIPABLE (2018) Work package 1 - Deliverable 1.1 Report on evolution of INERD and FUSEIS devices into the new DRBs, *Journal of Chemical Information and Modeling*. POLIMI, Italy.
- DISSIPABLE (2020a) 'Work package 2 - Deliverable 2.1 Report on calibration of numerical models for DRBs'.
- DISSIPABLE (2020b) Work package 2 - Deliverable 2.2 Report on parametric studies of DRB systems.
- DISSIPABLE (2021) '2 nd Phase Experimental Full-Scale Tests Behaviour of DRBrC Devices Results'.

- ECCS, 1986. Recommended Testing Procedure For Assessing the Behaviour of Structural Steel Elements under Cyclic Loads. Technical Committee 1 - Structural Safety and Loadings Technical Working Group 1.3 - Seismic Design N° 45, 0–11.
- EN1993-1-5 (2006) Eurocode 3 - Design of steel structures - Part 1-5: Plated structural elements. Brussels: (CEN), European Committee for Standardisation.
- EN1998-1: 2004. Eurocode 8: Design of structures for earthquake resistance. -Part 1: General rules, seismic actions and rules for buildings, CEN, Bruxelles, Belgium.
- Estekanchi H., Soltani A., Vafai A., SEISMIC BEHAVIOUR OF STEEL FRAMES WITH OFF-CENTER BRACING SYSTEM, 13th World Conference on Earthquake Engineering Vancouver, B.C., Canada August 1-6, 2004, Paper No. 1787.
- Faridmehr, I., Osman, M. H., Adnan, A. B., Najed, A. F., Hodjati, R., Azimi, M. A. 2014. Correlation between Engineering Stress-Strain and True Stress-Strain Curve. American Journal of Civil Engineering and Architecture, Vol. 2, pp 53-59.
- Farinha T., 2020. Assessment of hysteretic dissipative devices to improve the seismic behaviour of steel-concrete composite structures, MSc Dissertation in Civil Engineering, Instituto Superior Técnico.
- FEMA 273: NEHRP, 1997. guidelines for the seismic rehabilitation of buildings, Federal Emergency Management Agency.
- Ferreira J., *Actividade Sísmica/Vulcânica*, 2021 <https://oamarense.pt/actividade-sismica-vulcanica/>
- Georges S. Papavasileiou, Dimus C. Champsis, Nikos D. Lagaros, *Optimized seismic retrofit of steel-concrete composite buildings*, Journal Engineering Structures, Volume 253, 15 June 2020, 110573.
- Guedes, A., 2011. DIMENSIONAMENTO E COMPORTAMENTO SÍSMICO DE SISTEMAS METÁLICOS DUAIS, MSc Dissertation in Civil Engineering, Faculdade de Engenharia Universidade do Porto.
- Hillerborg, A. (1978) A model for fracture analysis.
- Kelly, P. (2013) Solid Mechanics Part II: Engineering Solid Mechanics.
- LESSLOSS 2007/03 – Innovative Anti-Seismic Systems Users Manual. Available online at <http://elsa.jrc.ec.europa.eu/events.php?id=4#reports>.
- Levanger, H. (2012) Simulating Ductile Fracture in Steel using the Finite Element Method: Comparison of Two Models For Describing Local Instability due to Ductile Fracture. University of Oslo.

- Lynch P., *8 coisas que você deveria saber sobre Fazlur Khan, o gênio dos arranha-céus*, 2016
<https://www.archdaily.com.br/br/794238/8-coisas-que-voce-deveria-saber-sobre-fazlur-khan-o-genio-dos-arranha-ceus>
- Medeot, R., 2004 – Re-centring capability of seismic isolation systems based on energy concepts. Proceedings of the 13th World Conference on Earthquake Engineering, Vancouver.
- Myers, A. T., Deierlein, G. G. and Karvinde, A. (2009) Testing and probabilistic simulation of ductile fracture initiation in structural steel components and weldments. Stanford University.
- Naeim F., 2002. The Seismic Design Handbook. Second Edition, New Jersey: Prentice-Hall.
- Nascimento, S. M. D. 2020. Detailed Experimental Programme Fully Dissipative and Easily Repairable devices for resilient buildings with composite steel-concrete structures – Pin device. MSc Dissertation in Civil Engineering, Instituto Superior Técnico.
- Newmark N. M., Rosenblueth E., 1971. Fundamentals of Earthquake Engineering, Prentice-Hall, Englewood Cliffs.
- Plumier, A., Doneux, C., Castiglioni, C., Brescianini, J., Crespi, A., Dell’anna, S., Lazzarotto, L., Calado, L., Ferreira, J., Feligioni, S., Bursi, O., Ferrario, F., Somnavilla, M., Vayas, I., Thanopoulos, P., Demarco, T. 2004. Two innovations for earthquake resistant design: The INERD Project, Final Report. Research Programme of the Research Fund for Coal and Steel, Grant Agreement No7210-PR-316.
- ProCiv, *O que é um sismo?*, 2017 <http://www.prociv.pt/pt-pt/RISCOSPREV/RISCOSNAT/SISMOS/Paginas/default.aspx>
- RFCS-02-2017 (2017) ‘DISSIPABLE – Fully Dissipative and Easily Repairable Devices for Resilient Buildings with Composite Steel-Concrete Structures’, in. European Commission, Research Fund for Coal and Steel. POLIMI (coordinator), IST, NTUA, SOFMAN, UNITN, RWTH, CSM, UNIPI.
- Sheikh H., Massumi A. Effects of bracing configuration on seismic behaviour of tall steel structures subjected to earthquake ground motions. Proceedings of the 10th National Conference in Earthquake Engineering, Earthquake Engineering Research Institute, Anchorage, AK, 2014.
- Soboyejo, W. (2002) Mechanical properties of engineered materials. Marcel Dekker.
- Stafford Smith B, Coull A., 1991. Tall building structures: analysis and design. Wiley: Canada.
- Stahleisen V., Hoff H., 1958. *Beobachtungen über den Bauschinger-Effekt an weichen und mittelharten Stählen*. Düsseldorf.
- Taranath BS., 1988. Structural analysis and design of tall buildings. McGraw-Hill: New York.
- Taucer, F. et al. (2014) DUAREM Full-scale experimental validation of dual eccentrically braced frame 83 with removable links. European Commission. doi: 10.2788/539418.

Vayas, I. et al. (2017) Innovative Anti-Seismic Devices and Systems (INNOSEIS). 1st edn. ECCS - European Convention for Constructional Steelwork.

Annexes

A.1 Test 06: R_S235_HSS_D1_C1

Among the tests with constant applied amplitudes, this was the one with the least accumulated dissipated energy.

The test specimen tested, 06-R_S235_HSS_D1_C1, is composed by a steel grade S235 chamfered pin and high strength steel (HSS) plates with 80/70/80 mm (D1) spacing (Fig. 3.27).

The loading history applied consists of a constant amplitude cycle of 20 mm (Fig. A.1). The test lasted 3h00m.

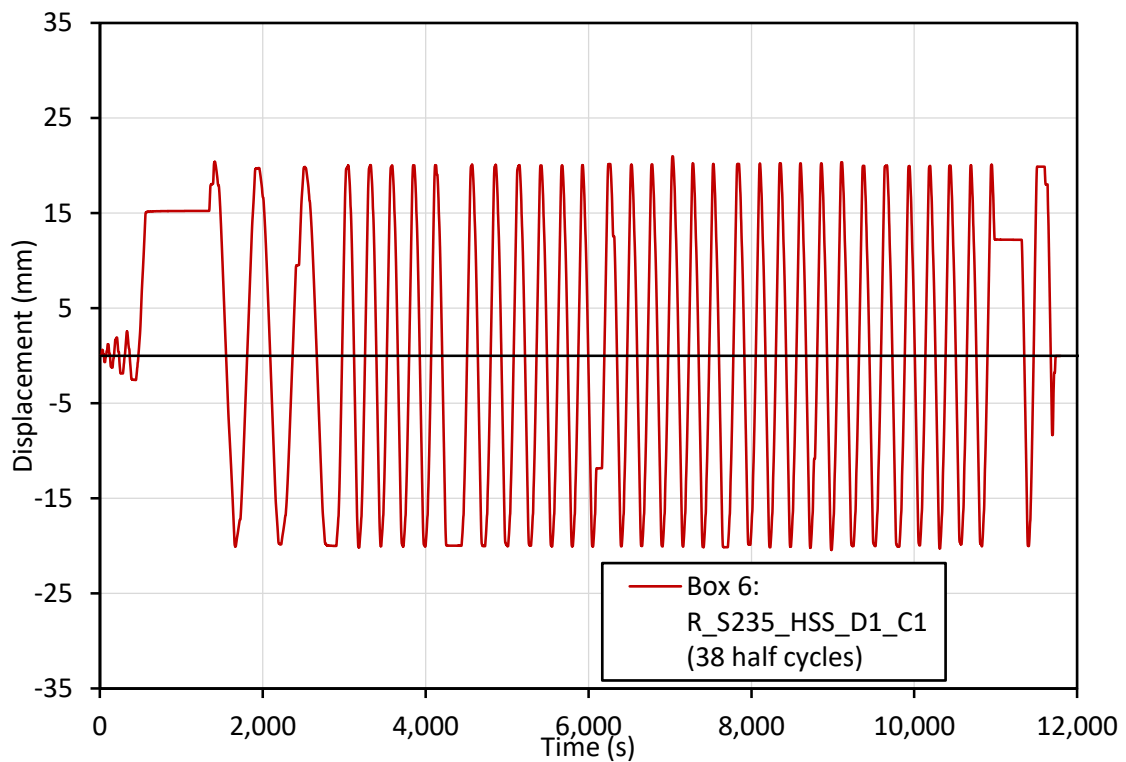


Fig. A.1: Load history for test number 6.

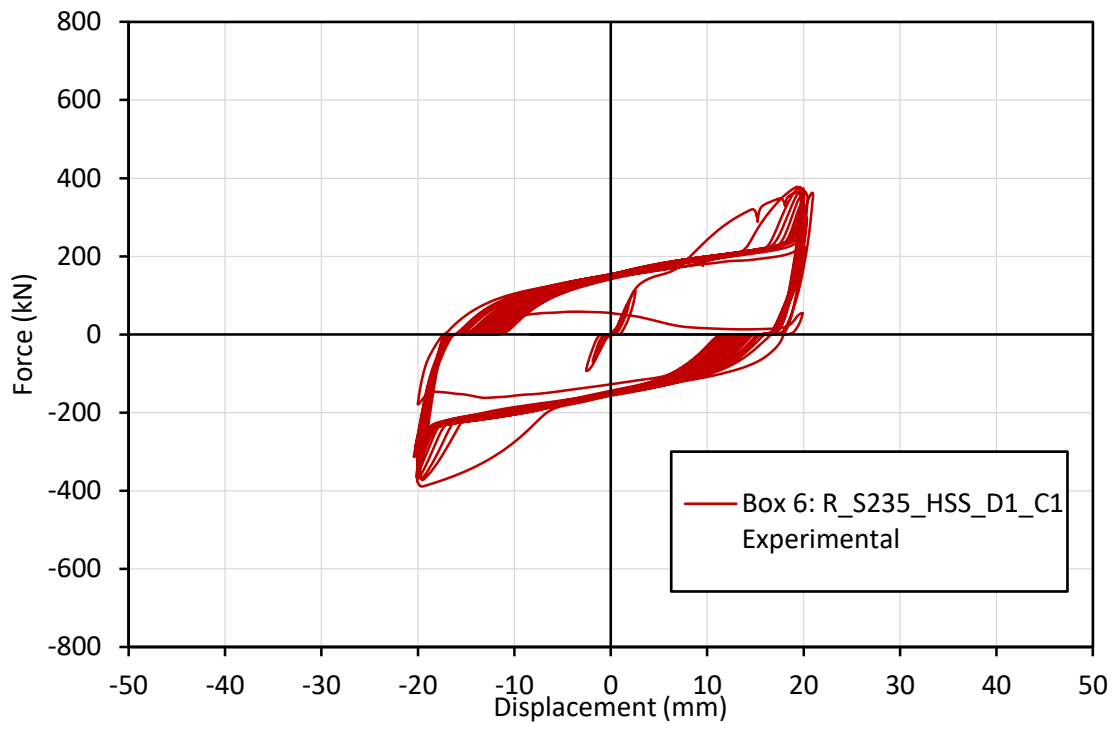
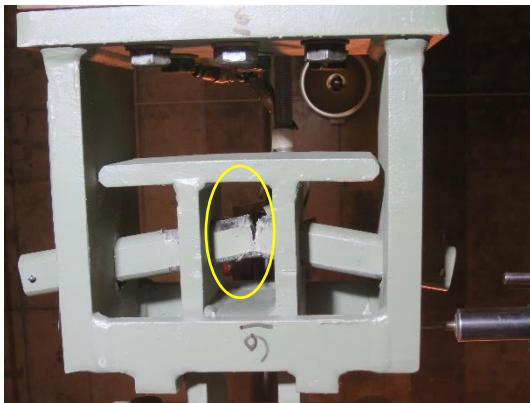
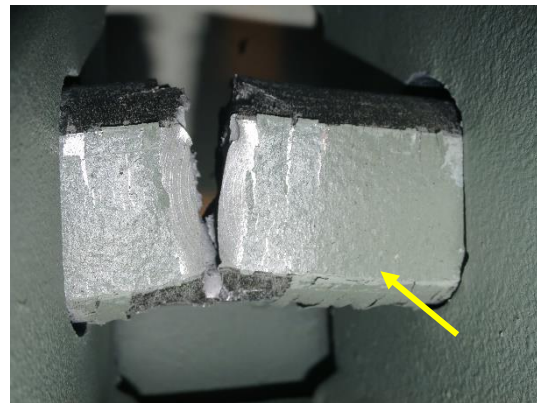


Fig. A.2: Force-Displacement curve of test number 6.



(a)



(b)

Fig. A.3: Experimental test number 6: (a) failure mode; (b) pin failure.

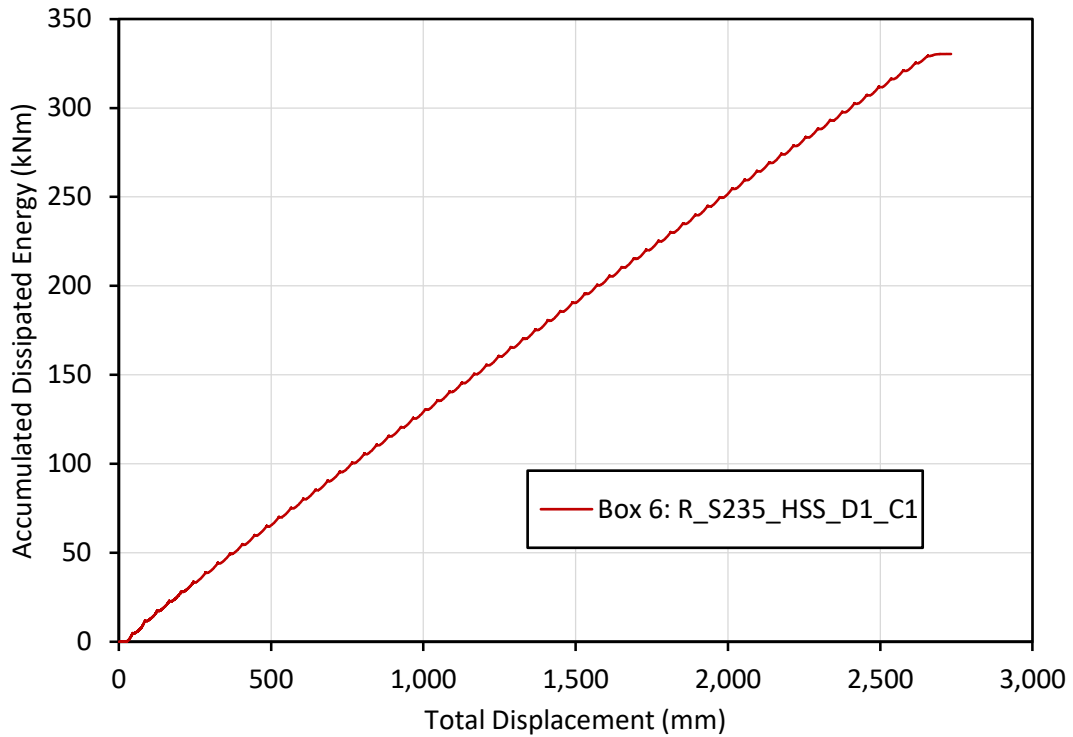


Fig. A.4: Accumulated Dissipated Energy curve of test number 6.

Tab. A.1: Results for experimental test 6.

	Positive	Negative
F_{max} (kN)	377.52	-389.16
δ_{max} (mm)	20.98	-20.42
Dissipated Energy (kNm)	330.33	
Nr. Of cycles	38	

Note: Reached pin failure.

A.2 Test 27: R_StS_HSS_D2_C1

Finally, the last test presented was the one that had higher forces than the imposed constant amplitude range tests.

The test specimen tested, 27-R_StS_HSS_D2_C1, is composed by a stainless steel (StS) chamfered pin and high strength steel (HSS) plates with 70/90/70 mm (D2) spacing (Fig. A.5).

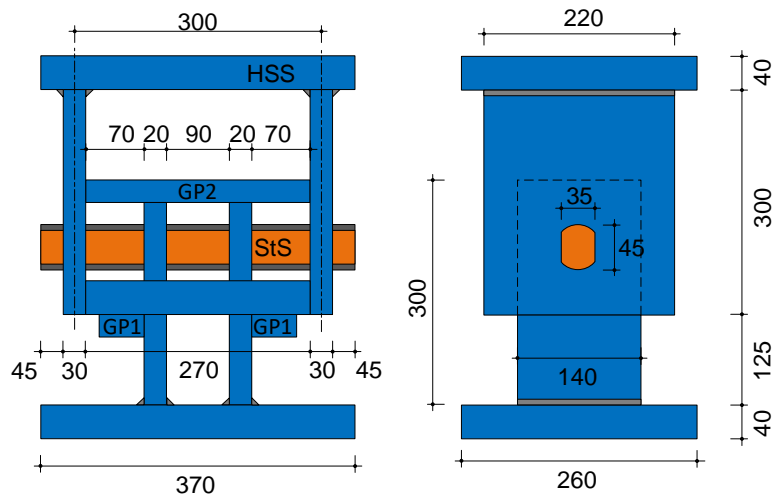


Fig. A.5: Specimen model of test number 27.

The loading history applied consists of a constant amplitude cycle of 30 mm (Fig. A.6). The test lasted approximately 2h15m.

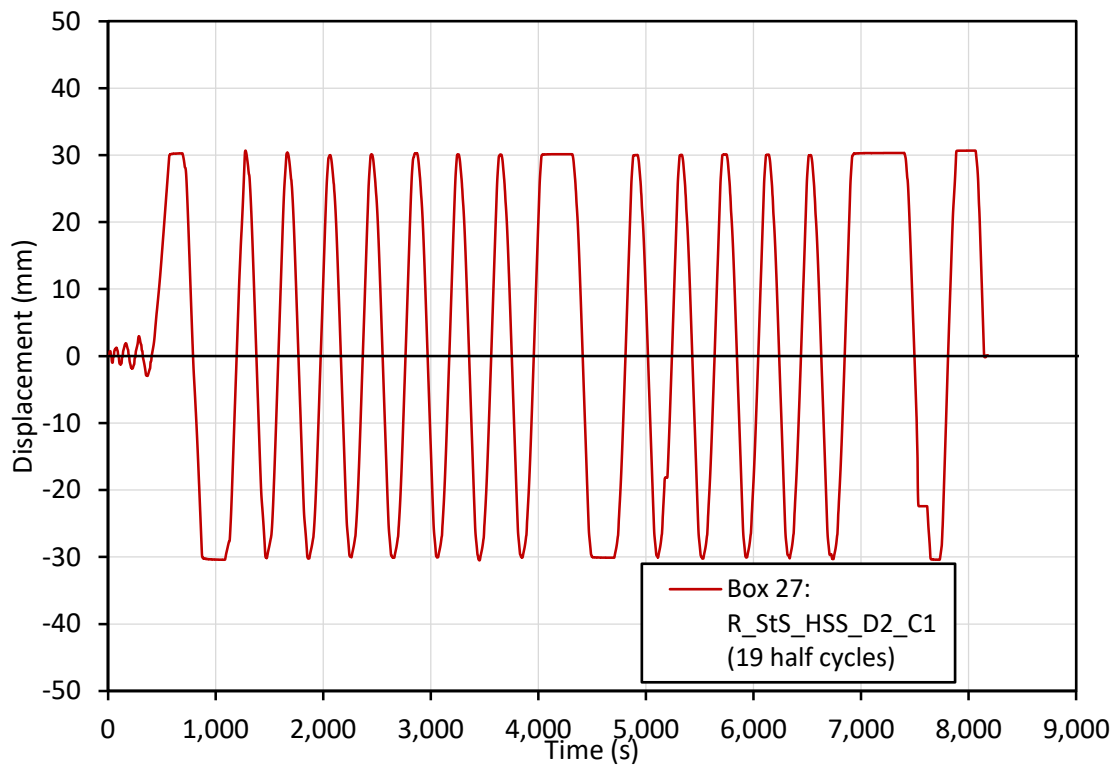


Fig. A.6: Load history for test number 27.

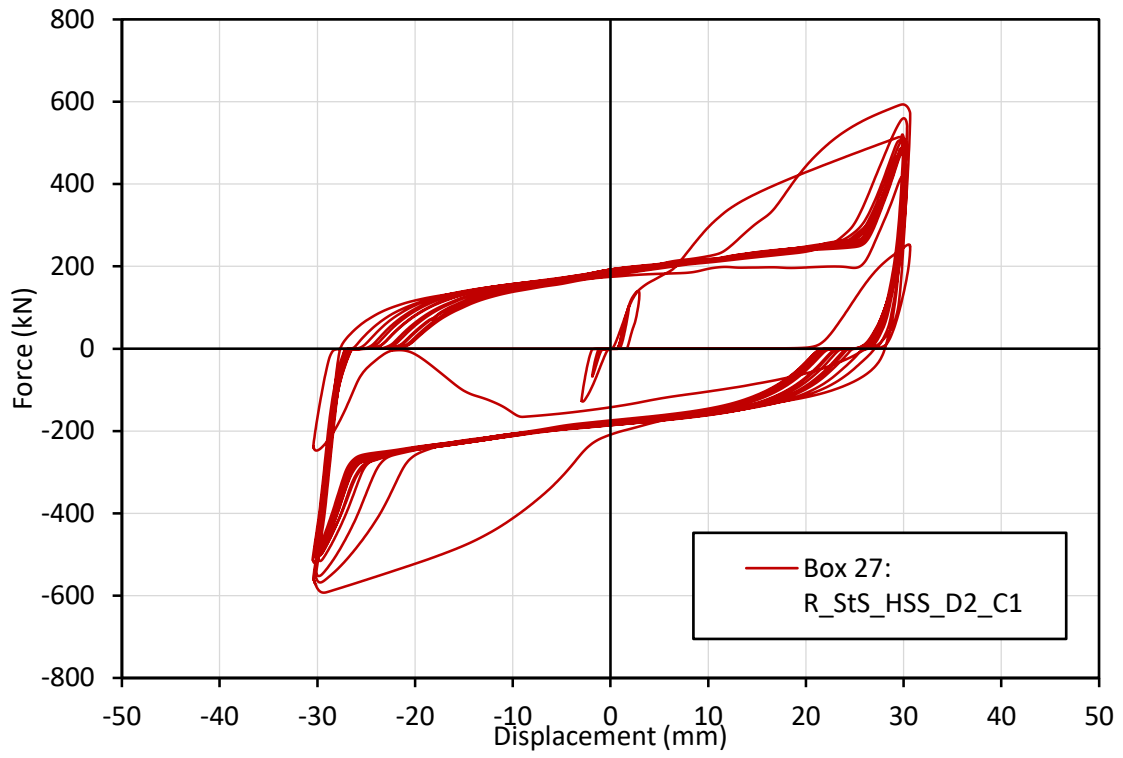
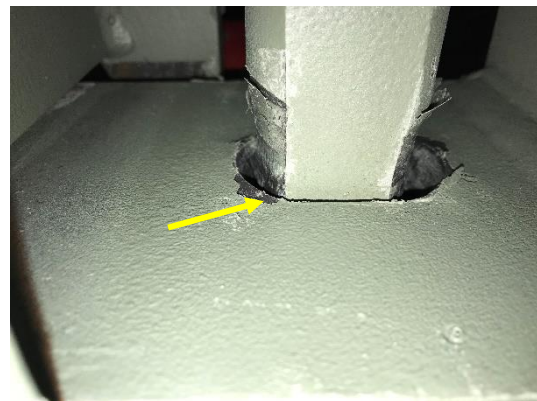


Fig. A.7: Force-Displacement curve of test number 27.



(a)



(b)

Fig. A.8: Experimental test number 27: (a) failure mode; (b) pin elongation.

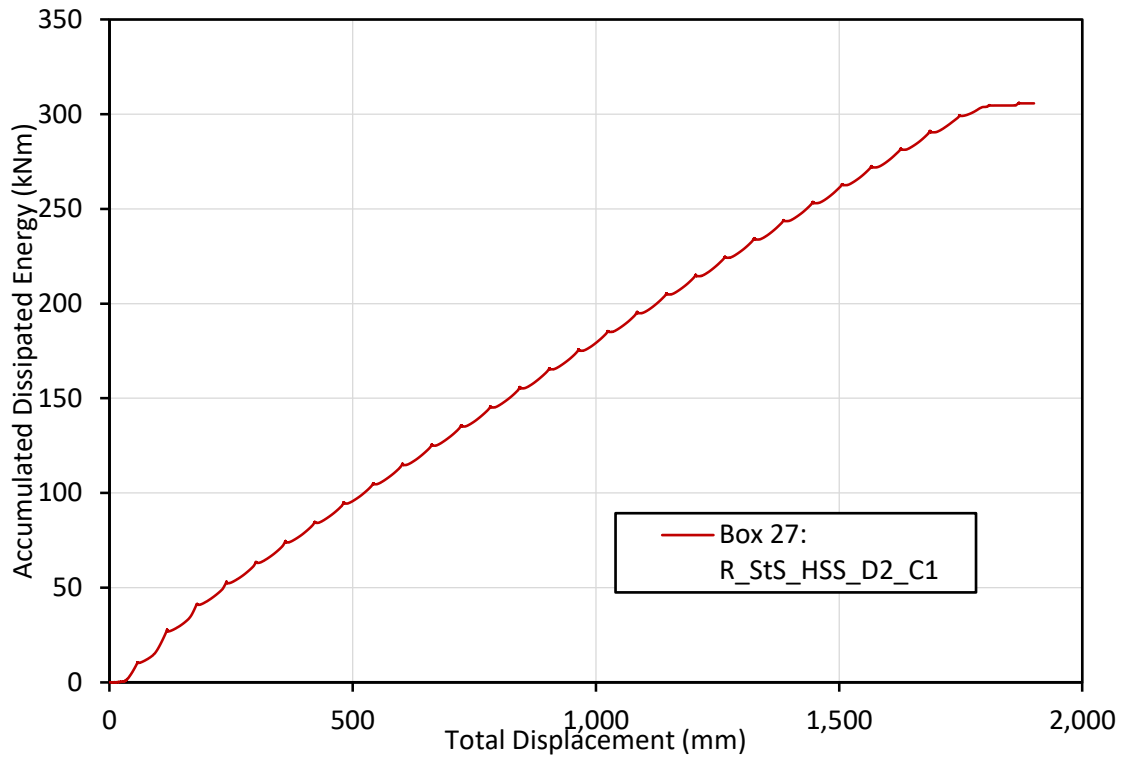


Fig. A.9: Accumulated Dissipated Energy curve of test number 27.

Tab. A.2: Results for experimental test 27.

	Positive	Negative
F_{max} (kN)	593.40	-592.68
δ_{max} (mm)	30.67	-30.48
Dissipated Energy (kNm)	305.72	
Nr. of cycles	20	

Note: Reached pin failure.

A.3 S235_HSS_D1

All tests of box S235_HSS_D1 together.

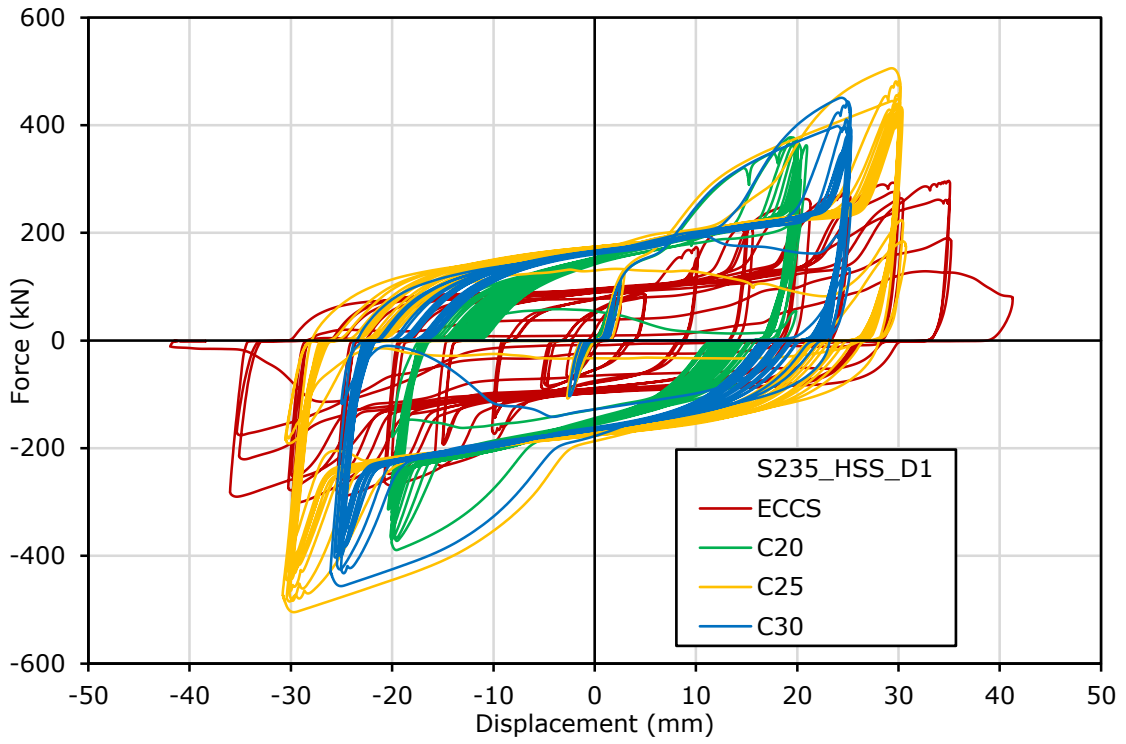


Fig. A.10: Curve Force-Displacement of all tests.

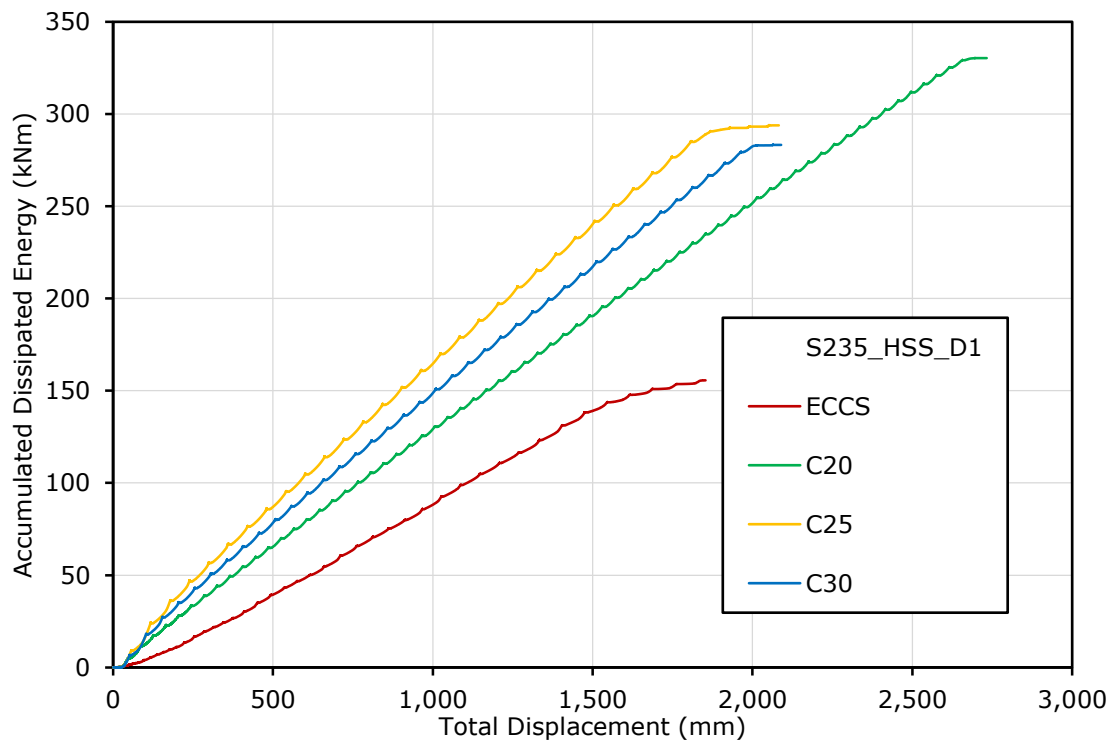


Fig. A.11: Accumulated Dissipated Energy of all tests.

A.4 StS_S355_D1

All tests of box StS_S355_D1 together.

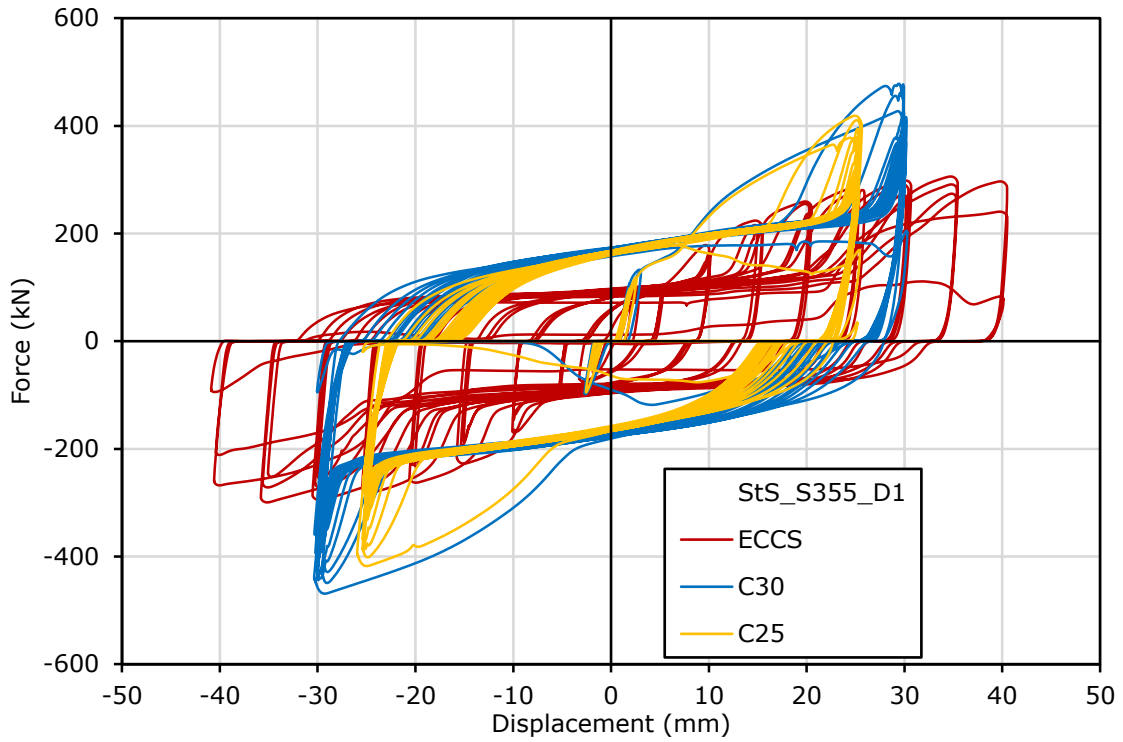


Fig. A.12: Force-Displacement curve of all tests.

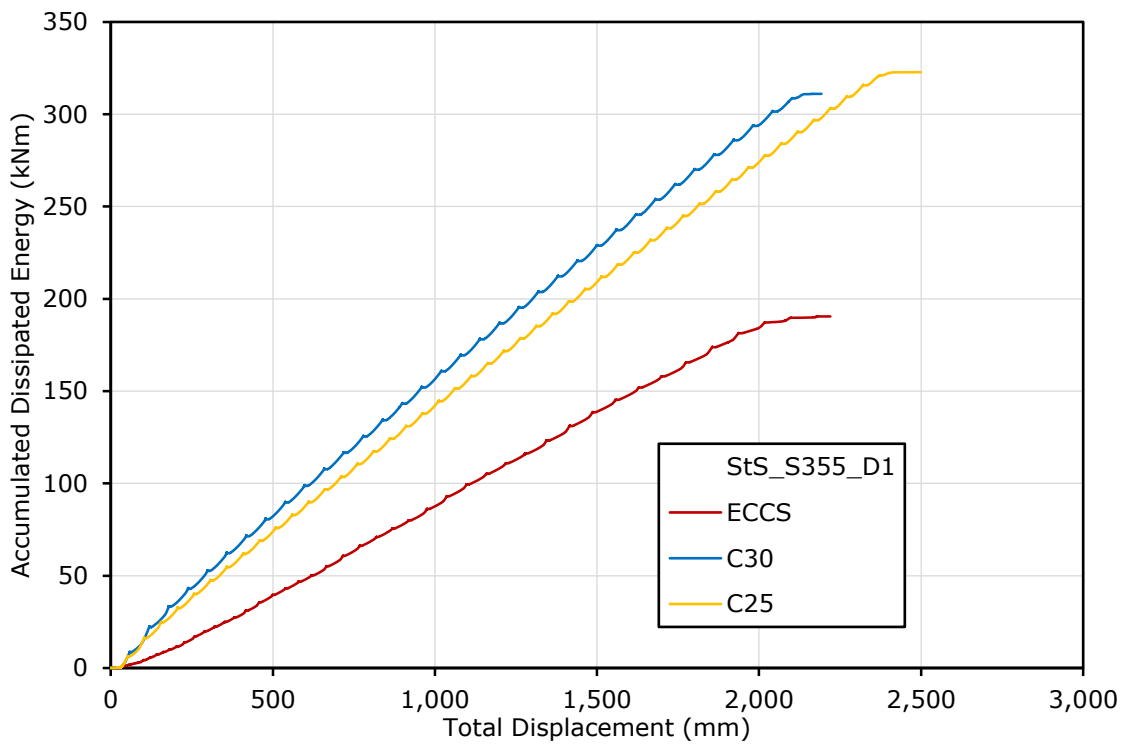


Fig. A.13: Accumulated Dissipated Energy of all tests.

A.5 StS_HSS_D1

All tests of box StS_HSS_D1 together.

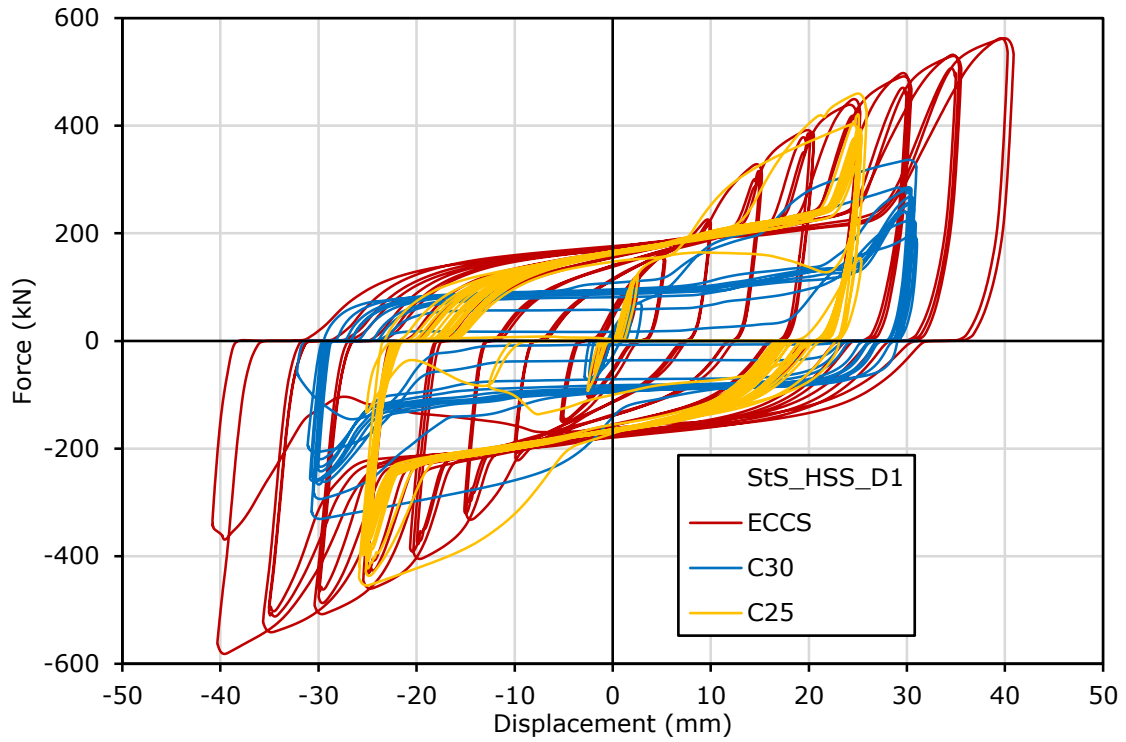


Fig. A.14: Force-Displacement curve of all tests.

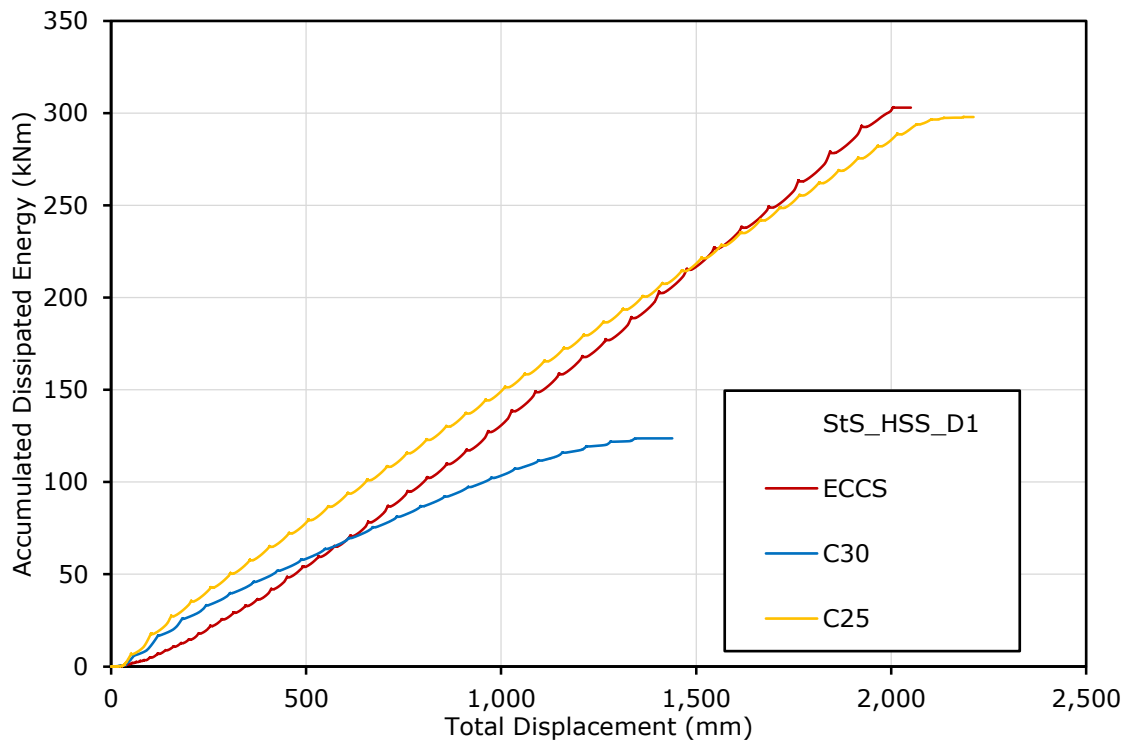


Fig. A.15: Accumulated Dissipated Energy of all tests.

A.6 S235_HSS_D2

All tests of box S235_HSS_D2 together.

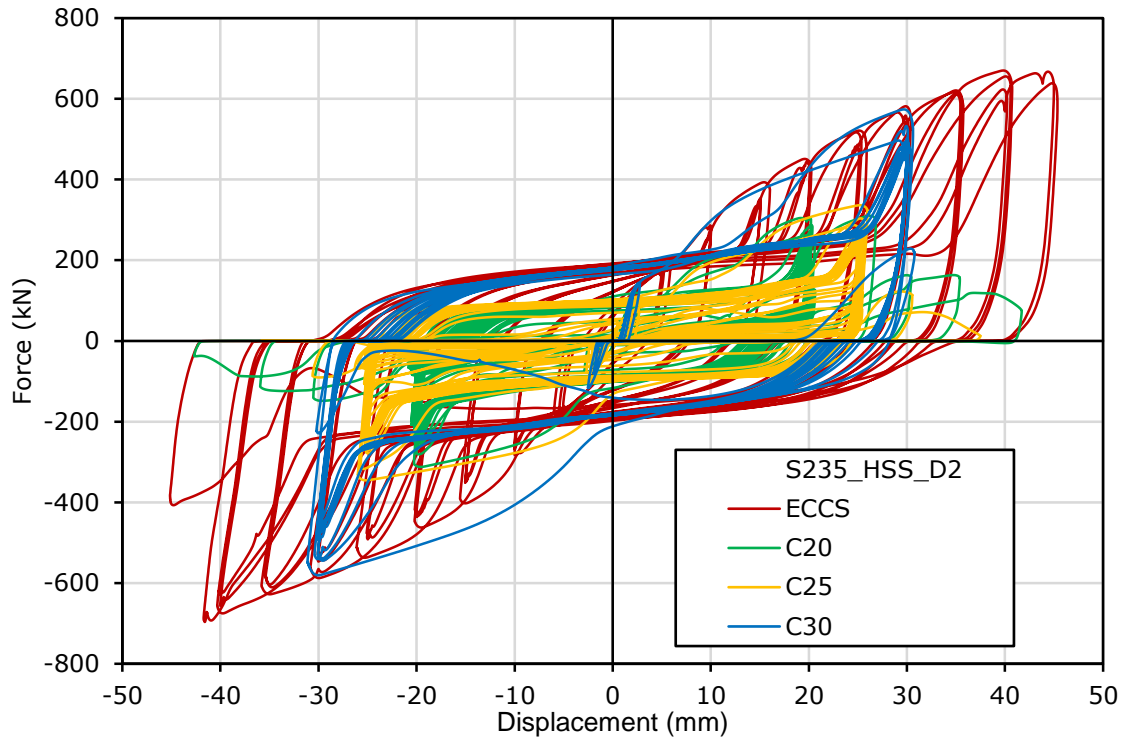


Fig. A.16: Curve Force-Displacement of all tests.

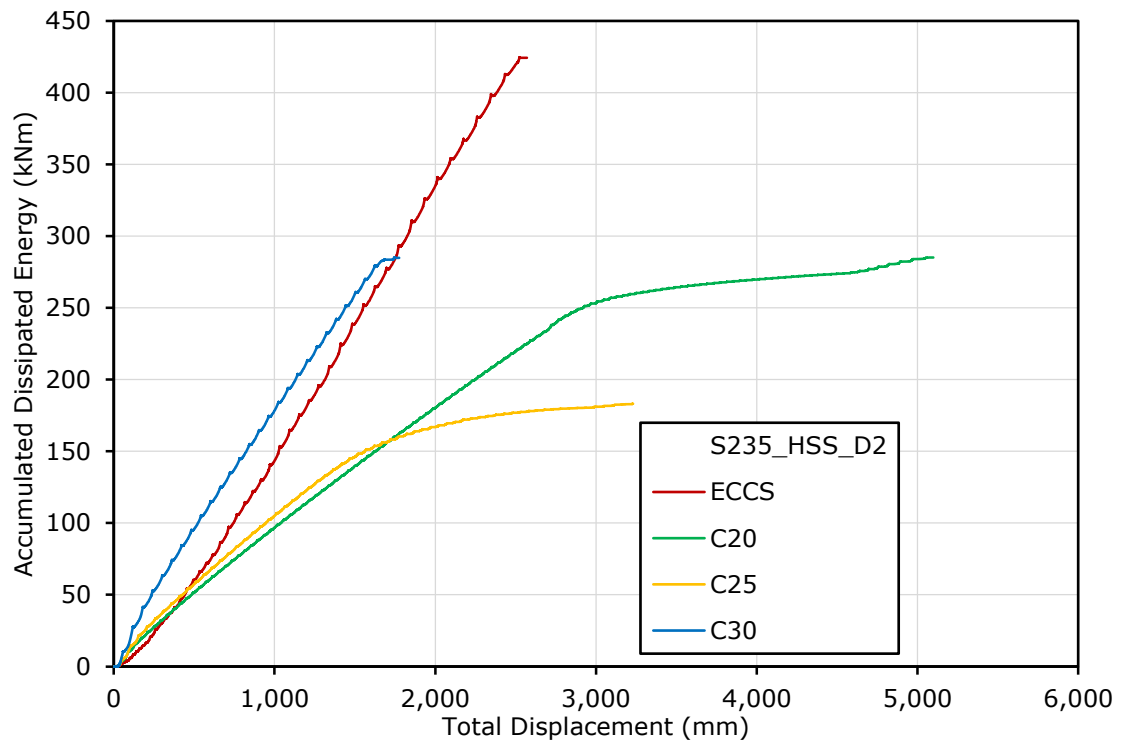


Fig. A.17: Accumulated Dissipated Energy of all tests.

A.7 StS_S355_D2

All tests of box StS_S355_D2 together.

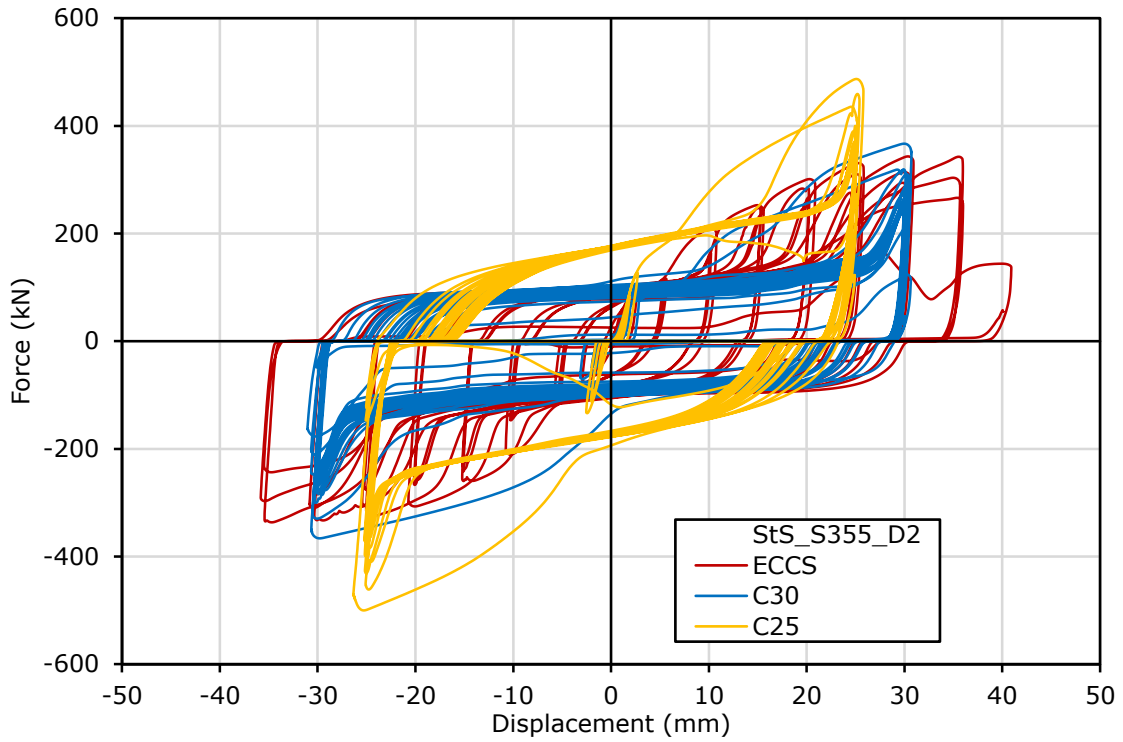


Fig. A.18: Force-Displacement curve of all tests.

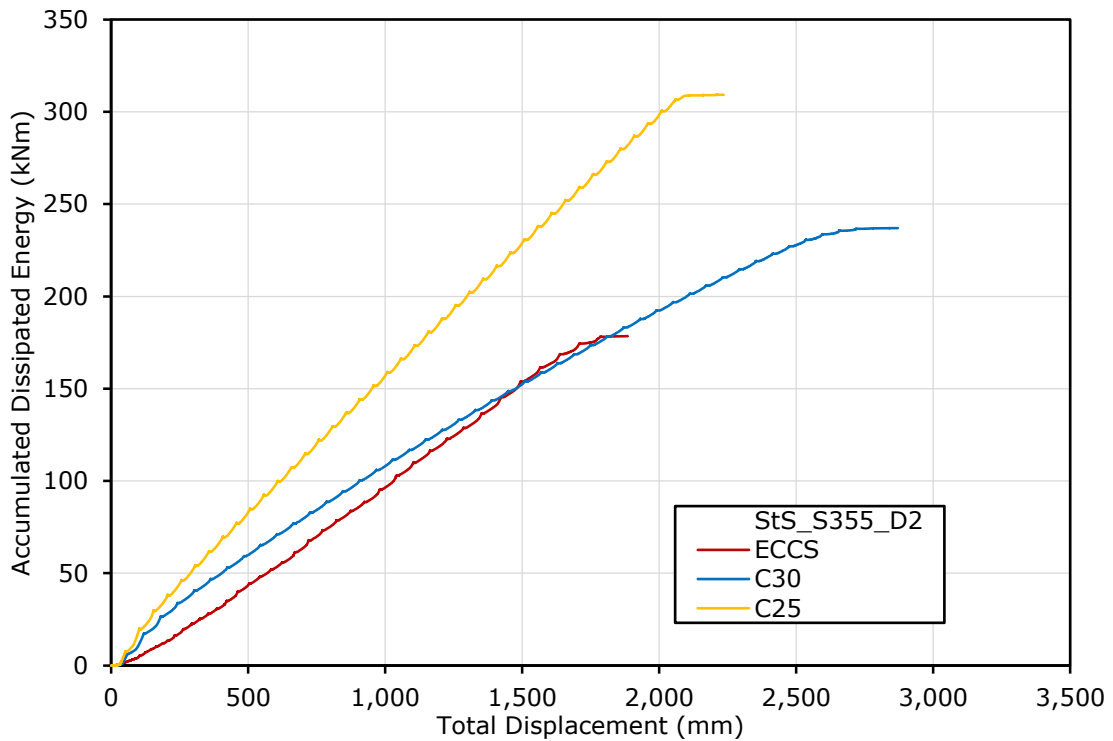


Fig. A.19: Accumulated Dissipated Energy of all tests.

A.8 StS_HSS_D2

All tests of box StS_HSS_D2 together.

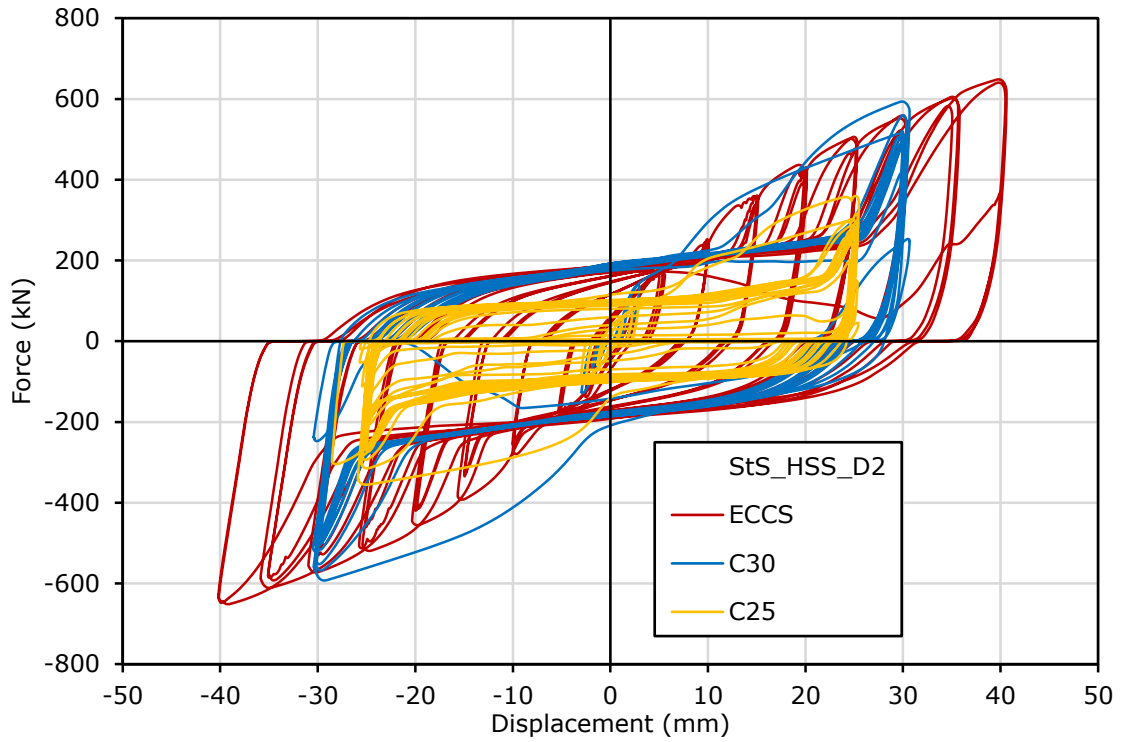


Fig. A.20: Force-Displacement curve of all tests.

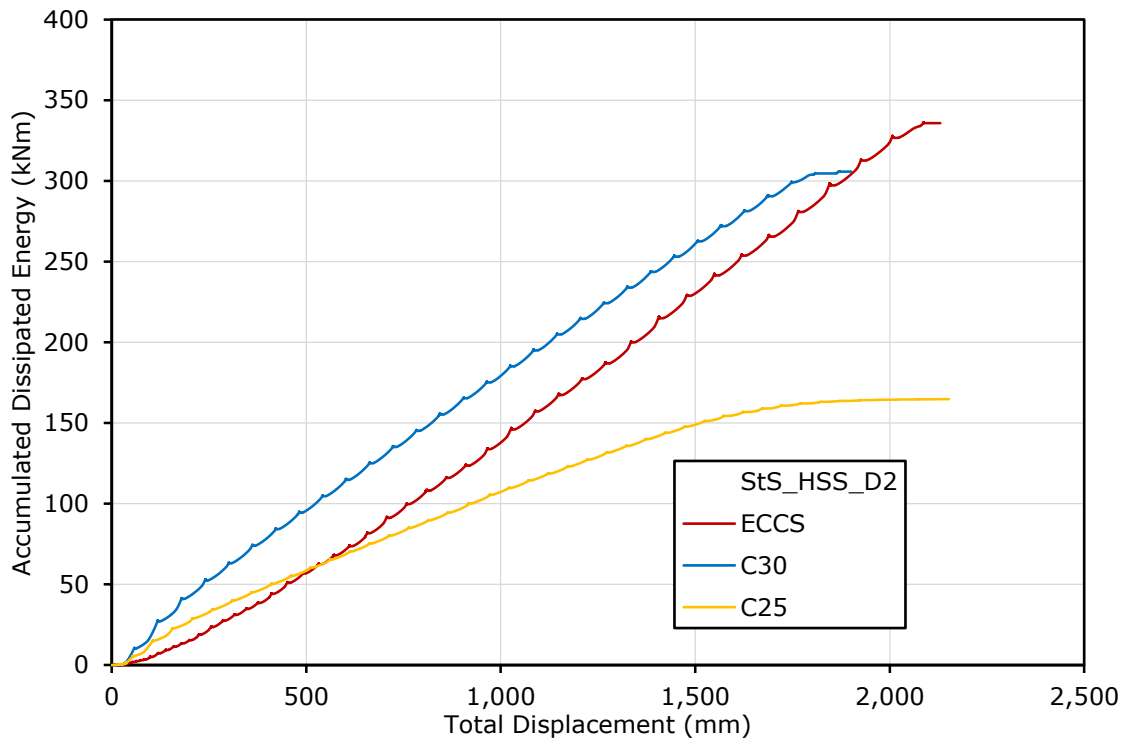


Fig. A.21: Accumulated Dissipated Energy of all tests.